


2017

I. THE HIGH STRAIN RATE RESPONSE OF HOLLOW SPHERE STEEL FOAM; II. THE DYNAMIC RESPONSE OF AN AMERICAN ELM TREE

Ignacio Cetrangolo
icetrang@umass.edu

Follow this and additional works at: http://scholarworks.umass.edu/masters_theses_2

 Part of the [Civil Engineering Commons](#), [Other Life Sciences Commons](#), and the [Structural Engineering Commons](#)

Recommended Citation

Cetrangolo, Ignacio, "I. THE HIGH STRAIN RATE RESPONSE OF HOLLOW SPHERE STEEL FOAM; II. THE DYNAMIC RESPONSE OF AN AMERICAN ELM TREE" (2017). *Masters Theses May 2014 - current*. 460.
http://scholarworks.umass.edu/masters_theses_2/460

This Open Access Thesis is brought to you for free and open access by the Dissertations and Theses at ScholarWorks@UMass Amherst. It has been accepted for inclusion in Masters Theses May 2014 - current by an authorized administrator of ScholarWorks@UMass Amherst. For more information, please contact scholarworks@library.umass.edu.

**I. THE HIGH STRAIN RATE RESPONSE OF HOLLOW SPHERE
STEEL FOAM**

II. THE DYNAMIC RESPONSE OF AN AMERICAN ELM TREE

A Thesis Presented

by

IGNACIO CETRANGOLO

Submitted to the Graduate School of the
University of Massachusetts Amherst in partial fulfillment
of the requirements for the degree of

MASTER OF SCIENCE IN CIVIL ENGINEERING

February 2017

Civil and Environmental Engineering
Structural Engineering and Mechanics Program

© Copyright by Ignacio Cetrangolo 2017

All Rights Reserved

- I. THE HIGH STRAIN RATE RESPONSE OF HOLLOW SPHERE
STEEL FOAM
- II. THE DYNAMIC RESPONSE OF AN AMERICAN ELM TREE

A Thesis Presented

by

IGNACIO CETRANGOLO

Approved as to style and content by:



Sanjay R. Arwade, Chair



Simos Gerasimidis, Member



Brian Kane, Member



Richard N. Palmer, Department Head
Civil and Environmental Engineering

ACKNOWLEDGMENTS

First and foremost, I would like to thank Dr. Sanjay Arwade. I am very glad that I spontaneously came up to talk to him about structural engineering at that open house many years ago. Soon after, we worked on the Eladio Dieste project and today, I am proudly presenting my thesis and I am very grateful to him for giving me this opportunity. Additionally, his guidance and support have been essential in all that I have accomplished and learned these past few years. I would also like to thank the members of my committee for their continued input: Dr. Simos Gerasimidis and Dr. Brian Kane, for their help along the way and their professional advice.

Beyond this project, my colleagues and classmates have been very helpful throughout the past year and a half, to which I extend my gratitude to and wish them all the best in their future endeavors. In particular, many thanks to Andrew Rock, an excellent student and better person, for all the work and learning we did together related to this project.

Lastly, my most profound gratitude goes out to my closest friends and family, especially to my grandparents. This accomplishment would not have been possible if it were not for them. Special thanks to my siblings, Gastón and Melina, and above all, to my parents, Andrea and Luis. *Gracias a ustedes por enseñarme todos los días la importancia de la educación, ser humilde, y luchar por mis sueños.*

ABSTRACT

PART I. THE HIGH STRAIN RATE RESPONSE OF HOLLOW SPHERE STEEL
FOAM

PART II. THE DYNAMIC RESPONSE OF AN AMERICAN ULMUS TREE

FEBRUARY 2017

IGNACIO CETRANGOLO

B.S., UNIVERSITY OF MASSACHUSETTS AMHERST

M.S.C.E., UNIVERSITY OF MASSACHUSETTS AMHERST

Directed by: Professor Sanjay R. Arwade

PART I

Hollow-sphere (HS) steel foam is a relatively new material whose cellular morphology and material properties qualify it as a metallic foam. This is an innovative foam-like material that exhibits high stiffness paired with low relative densities. Technological advancements in the past few decades have enabled the manufacturing of this material by a sintering process and, as a result, research has begun to accelerate as a multi-school collaboration effort for this particular work. Even though commercialization has been a challenge for metallic foams, it is imperative that researchers continue to prove and promote the advantages of metallic foams despite the current challenges posed by commercialization.

One of the most promising characteristics of metallic foams is their energy absorption capacity. This work explores hollow-sphere steel foam's ability to absorb energy at high strain rates under a dynamic impact load and builds upon an earlier work of quasi-static compression loading. Since most research in this field has been attributed to aluminum open-cell foams, the objective of this work seeks to build upon and apply existing methods to cultivate new research material for hollow-sphere steel foam. The premise of this work began with experimental research analyzing stress-strain relationships of a mass impacting samples of HS steel foam with different kinetic energies. As a result, material properties were extracted and quantified such as elastic modulus, yield stress, and energy absorption, among others. These properties set the foundation for the next set of research; finite element analysis whose objective is to develop a functional material model that could be used for a later application in structural engineering, such as a blast or crash impact.

PART II

The second part of this thesis applies structural engineering mechanics to a complex arboricultural project. A particular American elm (*Ulmus americana* L.) tree is the focus of analysis due to its usage for tree climbing competitions. Structurally, this work is relevant to structural engineering by involving finite element analysis of a branch of this American elm tree. This particular work has the objective of understanding how a particular American elm branch behaves structurally under a variety of dynamic loads with different input parameters.

Before any of the analyses can be implemented, the definite geometry of the tree has to be measured and material properties have to be calculated. Field experimental data are imperative for this project so that the idealized model can represent the real system as best as possible. Following the data acquisition and modeling of the tree, loads that were either measured or calculated are applied. These loads can be idealized as an impulse load and a cyclic load, with variability imposed within each of them. It is within this variability of the parameters within the loads that the purpose of this work arises. By applying extreme loads upon this tree branch, critical points along the branch can be identified by calculating maximum bending and axial stresses. These stresses indicate not only the critical points along the primary branch but in addition, they indicate the magnitude and severity of these potential stresses, which can be compared directly with the mechanical properties of the wood in the branch. The final intent of this work is to contribute to the knowledge of how a particular branch behaves dynamically in order to better equip tree climbers, academics, and professionals by integrating structural mechanics and arboriculture.

TABLE OF CONTENTS

	Page
ACKNOWLEDGMENTS	iv
ABSTRACT.....	v
TABLE OF CONTENTS.....	vii
LIST OF TABLES	ix
LIST OF FIGURES	xi
CHAPTER	
1. THE HIGH STRAIN RATE RESPONSE OF HOLLOW SPHERE STEEL	
FOAM.....	1
1.1 Introduction.....	1
1.2 Literature Review.....	2
1.2.1 Characterization and Manufacturing.....	2
1.2.2 Types of Steel Foam	3
1.2.2.1 Gasar (Lotus Type)	3
1.2.2.2 Powder Metallurgy.....	5
1.2.2.3 Hollow Sphere	7
1.2.3 Applications	10
1.2.4 Behavior under Compression.....	16
1.2.4.1 Quasi-static Loading	16
1.2.4.2 Dynamic/High Strain Rate	19
1.2.5 Finite Element Modeling	23
1.3 Experimental Testing.....	26
1.3.1 Introduction.....	26
1.3.2 Materials and Methods.....	28
1.3.3 Results and Analysis	33
1.3.3.1 Measurements and Geometry	33
1.3.3.2 Stress vs. Time	36
1.3.3.3 Stress vs. Strain.....	40
1.3.3.4 Comparison to Quasi-static Behavior	44
1.3.3.5 Strain Rate.....	48
1.3.3.6 Yield Stress and Elastic Modulus	50
1.3.3.7 Energy Absorption Capacity.....	52
1.3.3.8 Compression Waves.....	55
1.3.4 Conclusions.....	58
1.3.5 Future Work	59
1.4 Finite Element Analysis	60
1.4.1 Introduction.....	60
1.4.2 Modeling.....	61
1.4.3 Dynamic Analysis.....	65
1.4.4 Conclusions.....	67
1.4.5 Future Work	67

CHAPTER		
2.	THE DYNAMIC RESPONSE OF AN AMERICAN ELM TREE	69
2.1	Introduction.....	69
2.2	Geometry.....	70
2.2.1	Experimental Data	70
2.2.2	SketchUp Modeling	72
2.3	Finite Element Analysis	74
2.3.1	Modeling	74
2.3.2	Modeling Assumptions	79
2.3.3	Modal Analysis	81
2.3.4	Calibrating Young's Modulus.....	82
2.3.5	Static Analysis	83
2.3.6	Dynamic Analyses	86
2.3.6.1	Impulse Load	86
2.3.6.1.1	Introduction and Definitions	86
2.3.6.1.2	Results and Analysis	88
2.3.6.2	Climbing Load	96
2.3.6.2.1	Introduction and Definitions	96
2.3.6.2.2	Results and Analyses.....	98
2.4	Conclusions.....	100
2.5	Future Work	102
APPENDICES	103
A.	GENERAL AND FEM GEOMETRY OF TREE BRANCH.....	104
B.	MATLAB SCRIPT FOR IMPULSE LOAD SCENARIOS.....	106
C.	MAXIMUM CALCULATED STRESSES FOR ALL SCENARIO TYPES	108
BIBLIOGRAPHY	112

LIST OF TABLES

Table	Page
Table 1.1: Prototype and production structural applications for metal foams from selected literature (Brooks H Smith, 2012).....	11
Table 1.2: Geometry of the samples for drop height of 928 mm prior to impact.....	33
Table 1.3: Geometry of the samples for drop height of 928 mm post-impact.....	33
Table 1.4: Measured strain of set of samples for drop height of 928 mm	33
Table 1.5: Geometry of the samples for drop height of 747 mm prior to impact.....	34
Table 1.6: Geometry of the samples for drop height of 747 mm post-impact.....	34
Table 1.7: Measured strain of set of samples for drop height of 747 mm	34
Table 1.8: Geometry of the samples for drop height of 530 mm prior to impact.....	34
Table 1.9: Geometry of the samples for drop height of 530 mm post-impact.....	35
Table 1.10: Measured strain of set of samples for drop height of 530 mm	35
Table 1.12” Comparison of methodological (FBF) strain and measured strain for drop height of 928mm.....	48
Table 1.12: Comparison of methodological (FBF) strain and measured strain for drop height of 747mm.....	48
Table 1.13: Comparison of methodological (FBF) strain and measured strain for drop height of 530mm.....	48
Table 1.14: Elastic modulus for every sample for all drop heights	51
Table 1.15: Energy absorbed per m ³ for all drop heights	52
Table 1.16: Total energy absorbed for all drop heights	53
Table 1.17: Time function displacements for Sample 928_01	64
Table 2.1: Iterative process for calibrating Young's modulus	83
Table 2.2: Sum of stresses for the self-weight static analysis.....	86
Table 2.3: Input parameters	88

Table 2.4: Combined of bending and axial stresses and percentage within limit stress for impulse load “Scenario #1” in each element of the primary branch.....	91
Table 2.5: Sum of stresses for DdRT load: Jason 1	98
Table 2.6: Strength properties of the American elm.....	101

LIST OF FIGURES

Figure	Page
Figure 1.1: Gasar foam, showing largely elongated pores (Shapovalov, 1998)	4
Figure 1.2: Stress-strain response of steel foam and Al foam (Park & Nutt, 2000)	6
Figure 1.3: A sample of hollow sphere foam showing the spheres tightly packed	7
Figure 1.4: Structural parameters (a) of the HSS (D, d, and t) and (b) different types of porosities. The explanation of the parameters can be found in the text (Ashby et al., 2000).....	9
Figure 1.5: Engineering stress-strain curve from densification tests (Brooks H Smith, 2012).....	16
Figure 1.6: A sequence of images of the steel foam during the test at various strains (from left to right then top to bottom: 0.0, 0.10, 0.35, 0.50, 0.65, 0.85). Note that photos use a wide-angle lens; the plates did not rotate during compression (Brooks H Smith, 2012)	18
Figure 1.7: Schematic of the experimental set up used to perform impact tests by (Gaitanaros & Kyriakides, 2014a)	20
Figure 1.8: Hollow spheres geometry: sample geometry as generated (left); photograph of the experimentally-tested sintered hollow spheres steel foam (right) from (Brooks H Smith, 2012).....	24
Figure 1.9: Pre-cut samples of aluminum foam.....	28
Figure 1.10: Instron dynatup 8250 impact testing machine and set-up	28
Figure 1.11: Impactor with mass	29
Figure 1.12: Samples of HS steel foam pre-impact testing	29
Figure 1.13: 4,500 fps high-speed camera and lighting.....	30
Figure 1.14: Samples of HS steel foam post-impact testing.....	30
Figure 1.15: Stress vs. time for drop height of 928 mm	36
Figure 1.16: Stress vs. time for drop height of 747 mm	36
Figure 1.17: Stress vs. time for drop height of 530 mm	37

Figure 1.18: Average stress vs. time from all drop heights	37
Figure 1.19: Entire duration of data capture of stress vs. time for drop height of 928 mm	39
Figure 1.20: Stress vs. strain for drop height of 928 mm	40
Figure 1.21: Stress vs. strain for drop height of 747 mm	40
Figure 1.22: Stress vs. strain for drop height of 530 mm	41
Figure 1.23: Stress vs. strain for all drop heights	41
Figure 1.24: Comparison of impact to quasi-static behavior for drop height of 928 mm	44
Figure 1.25: Comparison of impact to quasi-static behavior for drop height of 747 mm	44
Figure 1.26: Comparison of impact to quasi-static behavior for drop height of 530 mm	45
Figure 1.27: Stress vs. strain curve for 20 ppi specimens with quasi-static data superimposed by (Rock, 2016)	47
Figure 1.28: Linear, elastic region for drop height of 928 mm showing the yield point	50
Figure 1.29: Linear, elastic region for drop height of 747 mm showing the yield point	50
Figure 1.30: Linear, elastic region for drop height of 530 mm showing the yield point	51
Figure 1.31: Wave speeds within the samples for drop height of 928 mm	55
Figure 1.32: Wave speeds within the samples for drop height of 747 mm	55
Figure 1.33: Wave speeds within the samples for drop height of 530 mm	56
Figure 1.34: Boundary conditions for preliminary model	61
Figure 1.35: Scaled displacement-time function for Sample 928_01	65
Figure 1.36: Development of stress-strain curve for 928_01	66
Figure 2.1: American elm tree branch of interest located in Central Residential Area, UMass Amherst.....	69

Figure 2.2: SketchUp model of the tree branch showing the scaled geometry for every section	74
Figure 2.3: Stress resultant output option for the moment-curvature models.....	77
Figure 2.4: FE model of the tree branch with numbered elements	77
Figure 2.5: First and second modes of the tree branch	81
Figure 2.6: Static analysis with labeled points.....	85
Figure 2.7: Impulse force function for the characteristics as described	89
Figure 2.8: Displacement-time response for impulse load: Scenario #1	93
Figure 2.9: Stress vs. mass of all scenarios.....	94
Figure 2.10: Stress vs. rope length of all scenarios.....	95
Figure 2.11: Stress vs. fall distance of all scenarios	95
Figure 2.12: Stress vs. percent strain at 10% MBS of all scenarios	96
Figure 2.13: DdRT ascending loads.....	97
Figure 2.14: SRT ascending loads	97
Figure 2.15: Displacement-time response for DdRT: Jason 1	99

CHAPTER

1. THE HIGH STRAIN RATE RESPONSE OF HOLLOW SPHERE STEEL

FOAM

1.1 Introduction

Steel is widely regarded as one of the primary materials for design and construction in the engineering industry in recent history. Its desirable material properties and relatively fast manufacturing techniques have proven for it to be a material of choice for design. Throughout history, the usage of steel for construction has overtaken that of iron in the same way that iron overtook stone and this is a direct result of society and the evolution of technology. As the needs of the public change over time and technology evolves as a result, new materials, products, and innovations come of age.

Over the last two decades, a new type material has arisen that introduces foam-like characteristics to a variety of metals such as aluminum, copper, titanium, and what is going to be the focus of this paper, steel. These metallic foams are cellular structures that are highly porous and offer potential applications to lightweight structures, energy dissipation, and various others mechanical properties. Within each type of metal alloy there exists different manufacturing processes that result in subtypes of metallic foams which will be discussed later on; the one that will be of interest is the hollow sphere (HS) steel foam. Currently, the research on HS steel foam has not been investigated as much as other types of metallic foams but the scientific community has certainly made great strides since a few decades ago.

1.2 Literature Review

1.2.1 Characterization and Manufacturing

In order to understand the advantages and applications of HS steel foam, it is imperative that the different manufacturing processes be understood for different metal foams, to make way as to how HS steel foam came to be. The structural characterization of metallic foams is established by its cell topology (whether it is open or closed cell), relative density, cell size, shape, and anisotropy (Ashby et al., 2000). The foam characteristics that are implemented into the solid metals result in a material that exhibits particular physical and mechanical properties. In general, the method of manufacturing consists of dispersing air into the solid metal matrix and thus reduces the relative density of the metal and introduces other advantages. Some of these advantages include its light weight and low density, its high strength to weight ratio, and its exceptional capabilities of energy dissipation.

In general, metallic foams are characterized as open-celled or closed-cell foams. Open-celled foams are those that contain a continuous network of metallic struts and ligaments and the enclosed pores in each strut frame are connected, are weaker, and are mainly used in functional applications where the continuous nature of the porosity is exploited (Kennedy, 2012). Open-celled foams permit the fluid flow, ingrowth, and thus in addition to impact applications there is a potential for orthopedic solutions (Ryan, Pandit, & Apatsidis, 2006). Closed-cell foams are different from open-celled in the sense that the cells are individually separated from each other by cell walls and they can be filled with gas. Both types of foams are closely related in their mechanical behavior and response, therefore they are useful in similar types of applications. These applications are a result of

the multifunctional performance of both types of foams and they include thermal insulation, heat sinks, acoustic insulation, energy absorption devices (crash protection), lightweight structural sandwich panels (as the core material) and vibration devices (Sanders, 2002). Further structural characterization of metal foams is included in (Ashby et al., 2000), where there is extensive literature on how these characteristics are identified using methods such as optical microscopy, scanning electron microscopy, and x-ray computed tomography.

There has been a substantial amount of research published on foams made of other types of metals such as aluminum, titanium, and copper, with aluminum being the most prevalent today in applications and research. Some of the published research on it for dynamic loading will be much of what this thesis will be referencing back to. Steel has not been the subject of as much research as the rest and this is because of the manufacturing difficulties that it poses due to steel's high melting point that requires new technologies (B. H. Smith et al., 2012). Despite these difficulties, research on different types of steel foams is in the early development stages. Today, there exists research topics within steel foams that encompass cell morphology, material characterization, finite element analysis, mechanical properties, quasi-static loading behavior, and current and future applications.

1.2.2 Types of Steel Foam

1.2.2.1 Gasar (Lotus Type)

The central theme of this thesis is HS steel foam and it is one of the most popular types of steel foams on the market today. Despite this, it is important that other popular types of steel foams are researched and understood. The gasar (lotus type) method for

fabricating steel foam is a very controllable method for steel foams in which long, cylindrical pores are aligned uniaxially along the length of solidification direction. This highly anisotropic, closed-cell material produces high-density foams ranging from about 35% to 100% relative density (Brooks H Smith, 2012). There are two types of fabrication methods in place today, the casting technique and the continuous zone melting technique. The casting technique utilizes a metal inside a crucible that is melted by an induction heating coil in a high-pressure gas atmosphere. The gas is dissolved up the equilibrium gas concentration into the molten metal, according to the Sieverts' law. The melt saturated with gas is poured into the mold. When some part of the mold is cooled down by a chiller or circulated water, the melt can be solidified unidirectionally. The elongated pores can evolve and grow by the influence of the unidirectional solidification (Nakajima et al., 2006). Once the solidification is completed, the result is the foam with cylindrical voids along the length of the metal, and these elongated pores can be seen in Figure 1.1. As a result, multiple parameters can be controlled during the fabrication more so than other

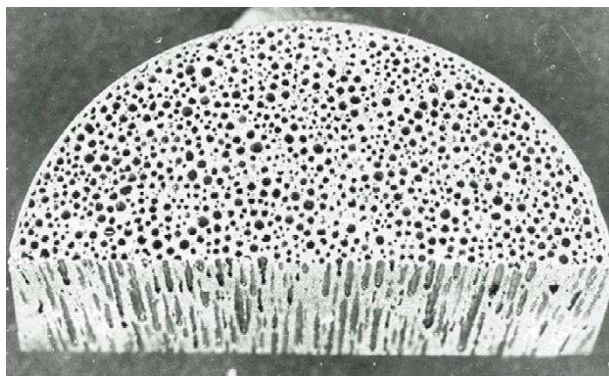


Figure 1.1: Gasar foam, showing largely elongated pores (Shapovalov, 1998)

fabrication types of steel foams. These parameters include melt temperature, solidification velocity, the dissolving gas pressure during melting and solidification, the inert gas pressure during melting and solidification (Nakajima et al., 2006). In continuous zone

melting, one segment of a rod of the base metal is melted in the presence of the diffusive gas and then allowed to re-solidify shortly thereafter. The lotus type steel foam allows for high tensile strength and ductility – up to 190 MPa at over 30% strain for a foam of 50% relative density – due to its direct load paths and largely non-porous matrix (Brooks H Smith, 2012). Whereas in comparison, HS steel foams reach ultimate strength at about 8 MPa at 2% strain and 8% relative density (Friedl et al., 2008).

1.2.2.2 Powder Metallurgy

Another popular type of steel foam that has a different manufacturing process is that of powder metallurgy (PM) techniques. PM steel foam is a closed-cell material that undergoes a random process of fabrication and results in a metal foam that exhibits relative densities between 0.38 to 0.64 according to Park and Nutt. To synthesize the foam, commercially available steel powder (an Fe 2.5C blend) is mixed with a foaming agent, usually strontium carbonate (SrCO_3) and magnesium carbonate (MgCO_3). After mixing, the blend is compacted by uniaxial cold-pressing to yield a virtually non-porous, semi-finished steel sample. Subsequently, the steel is melted to effect foam expansion, volumetrically. At this point, the metal softens and the released gasses infiltrate the pores to a size 2.5x the initial volume. Finally, the foaming agent gets exhausted and therefore the pressure in the pores decreases to result in the foam collapsing to its steady state volume. (Park & Nutt, 2000). In addition to the process of synthesizing steel foams via powder metallurgy methods, Park and Nutt conducted a study of their manufactured PM foam in order to obtain mechanical properties. They tested the foams by loading them in compression and compared them with a typical response of an aluminum alloy foam (Al-4Cu). The relative densities are 0.45 and 0.2 for the steel and aluminum foams, while the

absolute densities are 3.5 and 0.54 g/cm³. Figure 1.2 shows the stress-strain response of steel foam and aluminum foam in compression. It should be noted that the scale on the aluminum foam response curve had to be enlarged by a factor of 3 for comparison purposes.

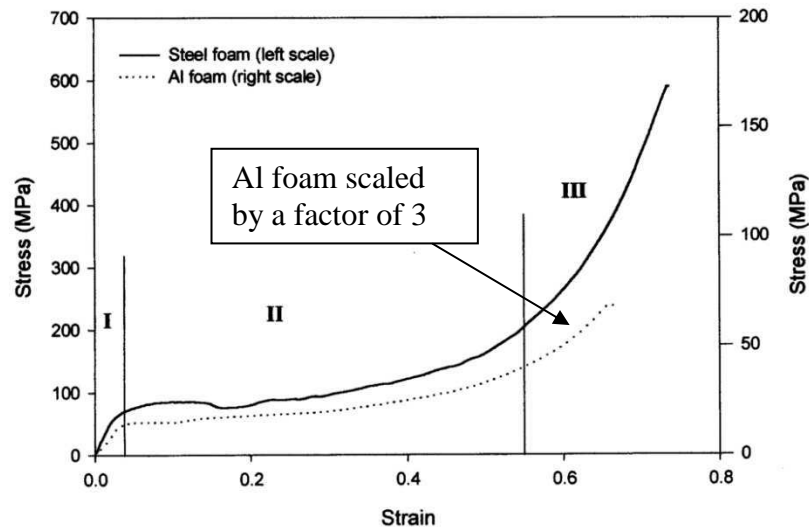


Figure 1.2: Stress-strain response of steel foam and Al foam (Park & Nutt, 2000)

This comparison is a very important distinction because it shows how similarly steel and aluminum foams behave, despite their difference in pore structure. Their response is almost identical and this is a key theme in later in my thesis. This stress-strain response graph shows three regions, labeled I-III. Region I is that of linear elastic behavior, and its yield stress marks the end of this region and the beginning of the foam collapsing due to compression. Next, region II is the strain hardening region where densification takes place. Densification in the steel foam is the event when the individual cells deform individually and on the global scale, interact together to collapse simultaneously, thus absorbing tremendous amounts of energy along a large amount of strain hardening. This region of nearly constant stress is what researchers strive for and gives substance to the integral under the curve, which is energy absorbed. After all of the cells buckle and collapse, there is a

sharp increase in strength over a short amount of strain. This is region III, where the foam is no longer a foam, and thus begins to take the characteristics of its solid counterpart.

1.2.2.3 Hollow Sphere

Hollow sphere is the last manufacturing process covered here and it is the most relevant one to this thesis. HS steel foam consists of metallic hollow spherical shells that are randomly packed together to form a structure that can be open-celled or closed cell (Friedl et al., 2008), as seen in Figure 1.3. To begin the process of fabrication, a plethora

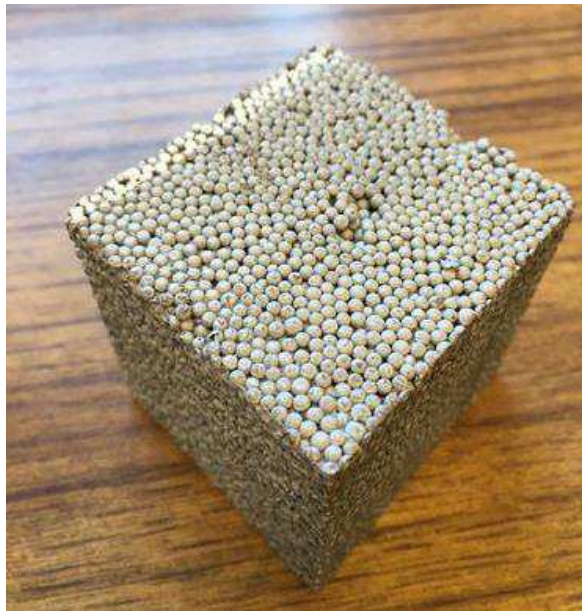


Figure 1.3: A sample of hollow sphere foam showing the spheres tightly packed

of thin-walled spheres need to be acquired and combined with a liquid suspension of metal powder and a binding agent, to then drain the liquid and create “green spheres”. These “green spheres” may be sintered individually and consolidated using an adhesive matrix, casting in a metal matrix, compacting through powder metallurgy techniques, or sintering the spheres. One special variation involves manufacturing the spheres with a blowing agent

within and then allowing the spheres to expand and sinter into the resultant shapes (B. H. Smith et al., 2012).

To bond the spheres there are multiple techniques to do so. One such way is to infiltrate the hollow spheres with a bonding material such as epoxy or a low melting metal (referred to as syntactic foams). The use of this material to fill the voids detracts from certain benefits of metal foams such as high specific strength or high-temperature properties (Sanders, 2002). Another method of bonding the spheres consists of applying large amounts of heat and pressure to an assembly of metal or ceramic precursor hollow spheres. This has an effects of the flattening of the contact between the hollow spheres, and are bonded by diffusion. This manufacturing technique has yet to produce good quality foams with uniform cell size and wall thickness due to the irregularities in the contact between cell walls, that are not perfectly flat, therefore they become difficult to model (Sanders, 2002). The last method of bonding that described next is the one of most interest and relevance to this thesis. It uses a liquid phase in the sintering process that forms a bonded neck region between spheres. There are two sub-techniques to achieve this neck. One such sub-technique consists of coating the hollow spheres with a metal powder slurry and assembling into a structure while the slurry is still in liquid form. The liquid forms the neck regions at contact points and is then dried to proceed to be sintered. The second sub-technique, the hollow spheres are coated with a material that melts at a lower temperature than the sphere material, such as solder or braze. They are then assembled and heated to the melting point beyond than that of the coating's and it liquefies and forms necks. In conclusion, this final liquefying phase bonding technique is a promising one because of the simplicity for modeling of the microstructure of the hollow sphere foams, as it presents the

simplest geometry and size (Sanders, 2002). As mentioned, there are different methods for bonding the spheres together to one another, producing sintering necks between the spheres. Due to these, three types of porosities are defined on a different scale: macroporosity, which is the volume inside the hollow spheres, mesoporosity, which is the cavity between the single spheres, and the microporosity, which is the porosity of the cell wall itself (Friedl et al., 2008). These porosities and necking are better illustrated in Figure 1.4. It is important to note these porosities because it goes back to the notion of HS steel foams having the capacity of being either open-celled or closed-cell. The morphology of the cell is important in determining the properties of the foam, just as is the types of porosities, due to the fact that porosity is what dictates the overall relative density of the material. The relative density can ultimately be tailored by varying the starting relative density of the hollow spheres and the extent of densification during consolidation (Ashby et al., 2000). Because porosity can be controlled and adjusted, density becomes a new design variable and, as a result directly affects the mechanical properties of the material such as elastic modulus and yield stress (Szyniszewski et al., 2014). HS steel foam offers

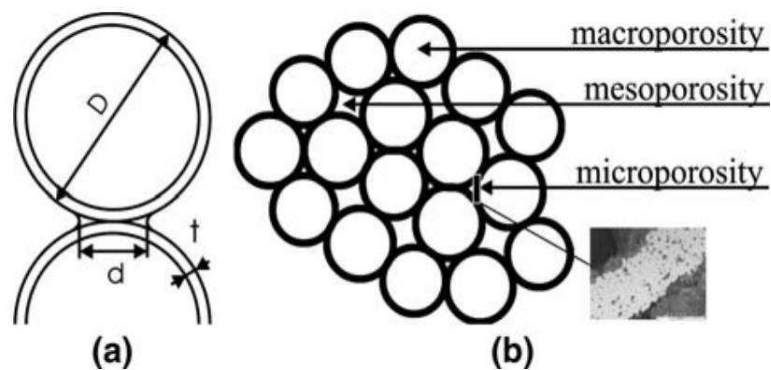


Figure 1.4: Structural parameters (a) of the HSS (D , d , and t) and (b) different types of porosities. The explanation of the parameters can be found in the text (Ashby et al., 2000)







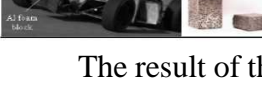
a variety of advantages over other conventional metal foams. Sanders conducted an analysis of the random packing of the hollow spheres and its effect on body-centered cubic and face-centered cubic sphere packings and showed that the face-centered cubic packing gave the highest values of moduli and strengths. In addition to that finding, the analysis showed that at relative densities of 10%, these moduli and strengths are three times larger than those of existing metallic foams and it increases to a factor of ten at relative densities below 5% (Sanders, 2002). Sanders stated that metal foams, in general, have a number of defects such as cell wall curvature, cell wall corrugation, and density variations that account for a large fraction of the degradation in properties. HS foams offer solutions to these defects in closed cell foams because ideal spheres can be bonded into a relatively defect-free structure (Sanders, 2002).

1.2.3 Applications

The introduction of a new material such as steel foam brings upon the research and development of said material in order to make it commercially available for appropriate applications in structural engineering. By introducing density as a design variable, steel foam has the potential to be more suited for some applications than solid steel in structural and non-structural ways. The structural advantages include minimizing weight while maximizing stiffness, increased energy dissipation, increased mechanical damping, and tuned vibration absorption frequencies; while non-structural advantages include decreased thermal conductivity, improved acoustical performance, provision of air/fluid transport within the material, electromagnetic and radiation shielding, and joining thermally dissimilar materials (B. H. Smith et al., 2012). It is clear that the most important characteristic of this material is that of energy absorption because of its weak behavior

under tensile forces and its favorable behavior under compressive loads. Due to this, the target market for applications exists in the mechanical, aerospace, and automotive domains. There is a very well compiled and comprehensible table by Smith which lists current structural applications for metal foams, below on Table 1.1. The foam sandwich panels consist of thin two thin-walled metal members that enclose the metal foam inside of it. Using foam core sandwich panels really exhibit their true potential when the stiffness and density are compared to a sheet of the same material with the same mass.

Table 1.1: Prototype and production structural applications for metal foams from selected literature (Brooks H Smith, 2012)

Prototype/In-Production Applications:	Weight	Stiffness	Energy	Damping	Vibration	Importance to civil engineering	Reference
 Steel foam bars, rods, sandwich plates	X	X	X			Proof-of-concept, demonstrates steel foam bars, rods, sandwich plates, foam filled tubes can all be produced; demonstrates essentially all aluminum foam applications could be extended to steel foam.	(Kremer, Liskiewicz and Adkins 2004)
 Wall/floor foam sandwich panels	X	X				Mass production of metal foam panels is possible. Great variety of bending stiffness-to-weight regimes opened up by this possibility.	(Banhart and Seeliger 2008)
 Balcony platform, parking floor slab	X	X				Metal foam panels may take significant, even localized, loads, thus a appropriate for floor slab, even heavily loaded parking garage (as load redistributes adequately).	(Hipke 2011)
 Crane lifting arm and support; analogous to structural beams	X	X				Metal foam beams can be produced that support high/typical structural loads and fatigue is not a unique problem as crane arms were fatigue tested.	(Banhart and Seeliger 2008)
 Fabrication equipment		X		X	X	Metal foam panels can be tuned for desired vibration characteristics, could, e.g., be very important for high-speed rail applications.	(Neugebauer, et al. 2004)
 Ariane 5 rocket cone prototype	X	X			X	Shell structures possible with metal foams, tight dynamic performance constraints can be met. Metal foam explicitly cheaper than traditional sandwich panel in this case.	(Banhart and Seeliger 2008)
 Race car crash absorber				X		Load transfer to the support limited by the foam yield. Slower deceleration reduces dynamic effects and enhances driver's safety.	(LeFebvre 2008), (Cardoso and Oliveira 2010)

The result of these experiments (Ashby et al., 2000) is that the foam is much stiffer than the dense sheet because by expanding its height will not change its mass but Young's modulus, E , will go down. Therefore, the stiffness-to-mass ratio of a foam is higher than that of the corresponding dense material which is a reason why foams are good materials for lightweight construction. In addition, it should be noted that the properties of the panels based on dense sheets can be designed for optimization based on compressional, tensional,

torsional, or flexural properties (Banhart & Seeliger, 1996). Foam sandwich panels have enabled a multitude of applications. One of them is a telescope lifting system whose goal is to increase the working height and horizontal outreach while keeping the total vehicle weight below 3,500kg. The vehicle was tested under multi-axial cyclic load, passed the requirement, and kept the weight as required for the 'Euro B' driving license which was an advantage for the operating company. Another significant application with these panels is that of the bicycle crank arm for racing bicycles. The manufactured foam part weighs 222g (78g less than the conventional part which weighs 300g). This is a significant reduction in weight, 30%, and it is a notable achievement granted that the lightest products on the market differ by some tens of grams only (Banhart & Seeliger, 1996). The biggest challenge in the application of metallic foams still remains to be the high cost, but as research and development continues for high quality foams, the demand for metallic foams should increase, thus driving the cost down due to higher volumes being demanded.

Another application that has been studied using metal foams as an alternative design choice for a racecar, Sabiá 5, using simulations of self-weight, static, dynamic, and crash tests in order to understand the mechanical behavior and design alternatives as a result of using metal foam components. Aluminum metal foam was chosen as a potential candidate for this study because its aim was to come up with an economic design that would present the necessary weight reduction and structural performance. This is possible due to aluminum foam's properties that encompass high stiffness, low specific weight, high compressive strength, and most of all good energy absorption (Cardoso & Oliveira, 2010). A series of computational tests were performed using aluminum metal foam as a design alternative and it compared to using solid metal of aluminum and steel of the same design,

and a sandwich panel which consists of a thin wall of solid metal enclosing metal foam in the middle. Finite element analyses were conducted for a self-weight simulation and crash tests. For the self-weight test, the optimal model was that of the one that was made of metal foam and aluminum rear bar; it is one of the lightest and most expensive, due to its metal foam composition. However, this may not be a great disadvantage considering the difference it can make in terms of performance and even safety, in the case of an impact. In the crash test, the vehicle undergoes impact against a barrier at a speed of 50 km/h. The sandwich composition model (aluminum and metal foam) presented less deformation and better impact energy absorption if compared with the whole aluminum model in addition to suffering the greatest plastic deformation but lowest deceleration, taking three times longer to reach the same level as the whole aluminum model (Cardoso & Oliveira, 2010). This is a good indicator that metal foams are desirable in these types of applications because it shows that the material strains efficiently and dissipates the energy as desired to the structure, and less so to the passengers. Cardoso and Oliveira mention that the passengers' protection during an impact depends mainly on three factors: an efficient conversion of kinetic energy into deformation, low deceleration levels for the passenger and maintenance of the passenger compartment integrity and conclude that the metal foam supports these factors. To complement this application, they also discuss the potential for metal foams to be applicable to the automotive industry as a whole due to the ability for mass production of metal foams, reducing the overall cost which remains to be a challenge for this material. Within this industry there is potential for metal foams that include sandwich panels, structural reinforcement, impact- absorbing elements, vibration damping,

among others, meeting the market trends: weight reduction for better performance and less fuel consumption, in addition to safety improvements (Cardoso & Oliveira, 2010).

As stated earlier, impact and energy absorption is where metal foams excel at and as a result, there have been a couple of studies performed for cellular structures and metal foams in the application to structures to prevent progressive collapse, where the case study at hand is the World Trade Center collapse of 2001. This case study explores the introduction of energy-absorbing floors within a building that arrests the downward traveling stress wave from a damaged section of a building, thus removing the kinetic energy fast enough to decelerate the falling superstructure without generating high enough loads to cripple otherwise undamaged structure (Newland & Cebon, 2002). Their findings concluded that for a barrier to be plausible and efficient, a material would have to be stretched from floor to ceiling on every floor of the building. Due to its plastic deformation mechanical properties, metal foams and honeycombs were taken into consideration and more precisely the best ones were aluminum foam or possible aluminum honeycomb due to their properties of energy absorption per unit volume and energy absorbed per unit cost. After supposing that the energy absorption material is added to every floor it was found that the weight increase for the total building is that of 6.5% with the aluminum foam being the reference material with a density of 1 Mg/m³ and that floor space losses for 40 MPa crushing stress aluminum foam accounts for about 1%. As for the analysis: the crippled structural columns collapse without absorbing energy, thus leaving the foam to absorb all of the kinetic energy, and the study found that as a rough guide if n stories are destroyed, we may expect $2n$ stories immediately below to be crushed to their full extent (about 40% compression). But, if the undamaged structure can survive an impact load greater than the

level assumed above ($2.3mg$ where m is the falling mass), the deceleration distance (and therefore the collapse length) can be less than calculated here (Newland & Cebon, 2002). Now, of course, there are different constructability challenges and solutions such as logically, more foam would have to be installed in lower stories than the higher stories, combining this system with others such as hydraulic dampers, etc. But the biggest challenge with this is the cost. Newland and Cebon provide great figures for comparisons of cost with different materials but in the end, the cost considerations are still a challenge due to the production of the materials being at low quantities. Today, the cost for these collapse barriers were calculated to be at \$1.3 million per story but if the production were to increase to large volumes, it was assumed that it would be half of that, or \$0.65 million. This is a significant number especially when accounting for inflation for the construction of the two towers, totaling it at \$1.26 million, therefore the installation of an energy absorption system is that of \$6 million per story per tower, 11% of the total cost of the towers. Putting it into perspective today, it would be a very large investment for this kind of system to be put in place for existing buildings so again, it is a challenge to design a system which achieves the required protection at minimum cost so that it is considered economically justifiable (Newland & Cebon, 2002). It is still early for the adoption of metal foams as a universally used material for applications but it is aimed that within the next decade, more research can be conducted in order for the usage to grow and be considered an essential material in engineering for a wide array of applications.

1.2.4 Behavior under Compression

1.2.4.1 Quasi-static Loading

Compression, tension, and shear tests were performed by Smith on a series of different types of steel foams but the compression of HS steel foam is the one that will be of focus. The purpose of these experiments was to evaluate the mechanical properties of the HS steel foam under three different types of compression tests, these properties include densification strain, Poisson's ratio, Young's modulus, and yield stress. Starting off with quasi-static loading is a good method for obtaining properties for a new material and Figure

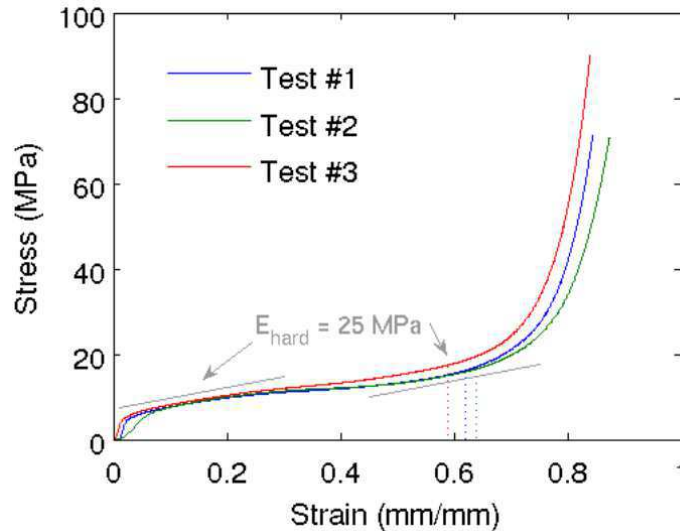


Figure 1.5: Engineering stress-strain curve from densification tests
(Brooks H Smith, 2012)

1.5 shows the response of loading a particular sample of HS steel foam quasi-statically. The samples were measured at relative densities of 14-15% and were measured at 52mm by 55mm in cross-sectional lengths and varying in heights of 80mm and 140mm in order to quantify the effect of seating of the specimens on measured strains. The samples were loaded uniaxially at displacement rates between 0.5mm/min and 1.0mm/min which is equivalent to strain rates between 0.003/min and 0.015/min. The first compression tests

were elastic unloading modulus tests and resulted in several properties; the yield stress was calculated by the traditional 0.002 offset of elastic modulus to be 3.2 ± 0.6 MPa but the tests show that there is substantial variation in the stress-strain response of the material at strains lower than roughly 0.02, but at strains greater than that the variability decreases. Having the 0.002 offset yield stress calculated captures this early variability, but in designing steel foam applications in which moderate to large deformations are to be expected, the 0.002 offset stress exaggerates the practical variability of the material properties. In contrast, another value was calculated per the 0.01 proof yield stress and resulted in 4.0 ± 0.3 MPa and Smith suggests that this is a better choice when defining bi- or tri-linear material properties. Another property that was deduced from the compression test was the elastic modulus (3150 ± 250 MPa) and it was obtained by performing a least square linear regression on the unloading mechanisms. Smith suggests that the highly variable moduli measured prior to $\epsilon_y = 0.02$ are likely due to initial imperfections in the test specimens, such as surfaces which are not precisely parallel, and should not be regarded as characteristics of the material (Brooks H Smith, 2012).

The second compressive tests were densification strain tests and the response is that shown in Figure 1.5 and Figure 1.6 shows the specimen visually being densified progressively. Both of these figures are important in understanding how the material behaves and it is clear that Figure 1.5 resembles the behavior where the material undergoes elastic deformation until yield. Next, the foam undergoes densification and strain hardening where the hollow spheres crush locally to form horizontal bands and this can be seen in Figure 1.6. Finally after the material is completely crushed the foam is no longer a foam and begins to behave as the solid metal. Smith observed during these tests the material formed into an S- or C-curved shape beginning at a longitudinal strain of approximately

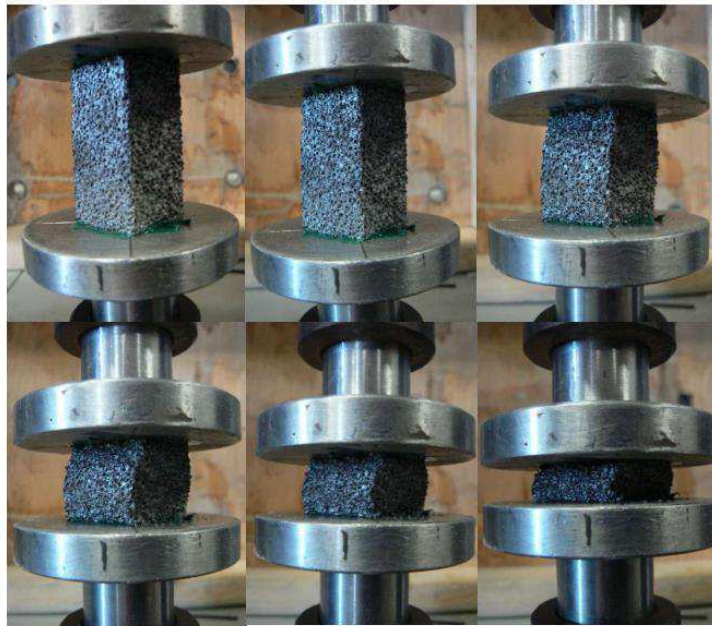


Figure 1.6: A sequence of images of the steel foam during the test at various strains (from left to right then top to bottom: 0.0, 0.10, 0.35, 0.50, 0.65, 0.85). Note that photos use a wide-angle lens; the plates did not rotate during compression (Brooks H Smith, 2012)

30% and suggests that this anomaly is similar to buckling in visual appearance, its commencement at such high strains suggests that it is caused by locally higher strains in the material. At a strain of 0.65 ± 0.05 is when it was observed that densification began,

even though there's no established definition for this in external sources but it was later established from these tests that densification is assumed to begin when the tangent modulus exceeds for the first time the post-yield tangent modulus. The final property that this test obtained was the hardening modulus to be between 20 and 25 MPa (Brooks H Smith, 2012).

The last set of compression tests were done in order to calculate Poisson's ratio. Smith found that from three tests for this material and loading the Poisson's ratio varied by increasing from 0 to a peak value above 0.3 at an applied strain of approximately 0.4 and then decreased until the end of the test that was when the material reached densification. Even though the Poisson's ratio is greater than 0.3 for a part of the test, for most of the duration of it is well below that ratio and this is a significant finding because it corresponds to the material's behavior under multiaxial stress states and even under uniaxial loading is lower than Ashby et al.'s predicted Poisson's ratio values of 0.32-0.34 (Brooks H Smith, 2012).

1.2.4.2 Dynamic/High Strain Rate

There has been a number of studies performed among metal foams with impact loading and high strain rate behavior. One of them is that of composite metal foam (CMF) which is essentially like an inverted HS steel foam when examined visually, it is a solid metal matrix with random voids inside as a result of hollow metallic spheres. It should be noted that this type of foam is much stiffer and stronger than other foams such as conventional HS steel foam, for example its relative density is approximately two times that of HS steel foam and exhibits ultra-high-strength while maintaining large densification strains above 50% that is capable of absorbing energy above 7-10 times higher than any

other metal foam made with similar materials (Rabiei & Vendra, 2009). The study began with two different CMFs made up of steel-steel and aluminum-steel with different combinations of pore sizes and loaded quasistatically at a ram speed of 1.27 mm/min. Then, using the Hopkinson bar experiments, dynamic impact tests were performed at varied strain rates up to 3.5×10^3 1/sec which consisted of releasing a projectile at high speeds through a gas gun to impact the foam and high-speed video cameras were used to process the displacement data, a schematic of this is shown in Figure 1.7. The results showed that loading the sample under high strain affects the stress-strain curve significantly and when

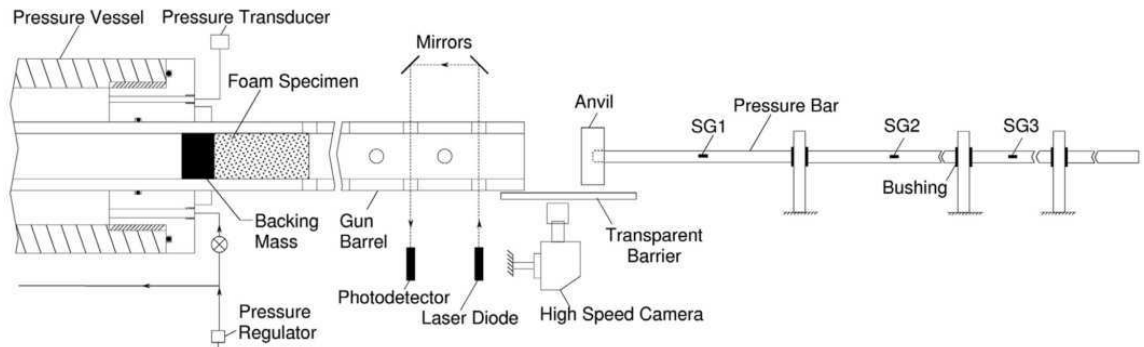


Figure 1.7: Schematic of the experimental set up used to perform impact tests by (Gaitanaros & Kyriakides, 2014a)

compared to quasistatic tests, the yield strength rises to about 80% and the plateau strength increases as well to about 60%. It was concluded by Alvandi-Tabrizi et al. that this implies a remarkable hardening due to strain rate sensitivity and that this sensitivity is more pronounced at nominal strains below 25-30% whereas at higher strains the difference between the dynamic and quasi-static test results becomes smaller, interpreting lower strain rate dependency (Alvandi-Tabrizi, Whisler, Kim, & Rabiei, 2015). This strain rate sensitivity of metal foams has four major parameters that can be contributed to it: rate dependency of the parent metal, micro inertia effect of the cell wall material, plastic shock wave propagation, and pressurization of the entrapped gas (air) inside the cells (Alvandi-

Tabrizi et al., 2015). Energy absorption was calculated in these tests and found that energy absorption is higher for S-S CMF than Al-S CMF. Also, by increasing yield strength and plateau strength, energy absorption increases because it's calculated as the area under the stress-strain curve. This finding coincides with Paul and Ramamurty's conclusion that energy absorption during plastic deformation increases with increasing strain rate and are therefore great candidates for applications in impact protection due to their ability to absorb significantly high energies at high strain rates (Paul & Ramamurty, 2000). It was found that from this test's impact velocity, the velocity of the impactor was not fast enough to generate a plastic shock wave so it was considered neutral. Ideally, a plastic shock wave would follow the elastic wave; where the deformation mode of the foam goes from uniform to localized due to stress difference before and after the shock front. Other findings show the difference in failure modes from comparing quasi-static loading and dynamic loading where cracks visually appear on the outside of the fully densified foam from dynamic tests but are absent in quasi-static tested foams. An explanation for this is theorized to be that there are different rates at which the pressurized air is released from the foam's spheres. Final concluding results are that the dynamic behavior of CMF under compression is insensitive to the sample geometry (Alvandi-Tabrizi et al., 2015).

The other type of foam that has been studied is aluminum open-celled foam. While this particular foam is a different base metal and open-celled than HS steel foam its behavior and properties are relevant and relatable. Similarly to the CMF studies, these experiments also use a gas gun to crush the foam dynamically at impact speeds of 20 to 160 m/s and record the deformation behavior using a high-speed video camera. The primary findings are that crushing of the foam at speeds of 40 m/s or less the behavior of

the foam is very similar to that of quasi-static loading, and at speeds of 60 m/s or greater developed nearly planar shocks that propagated at well-defined velocities. Also, it was found that the material is densified by the shock with the Hugoniot strain increasing with impact speed, approaching asymptotically approximately 90% at the higher velocities used (Gaitanaros & Kyriakides, 2014a). In these experiments, it was also found that energy absorption increased as a function of velocity increasing. The second part of this experiment involved modeling these impact tests using finite element techniques and simulating the dynamic crushing behavior that was obtained in the experimental tests. The particular open-celled aluminum foam used was modeled using the *Surface Evolver* software with the cells having 11 to 17 sides to them and the ligaments connecting them as shear-deformable beams with variable cross sections (Gaitanaros & Kyriakides, 2014b). Using a finite element method enabled the Gaitanaros and Kyriakides to model the foam at speeds up to 200 m/s. The models were able to reproduce the quasi-static crushing behavior and was extended to the dynamic models as a foundation. After much work, the dynamic tests were able to be reproduced as well and checked with calculations. At speeds of 20 m/s and lower the crushing response was very similar to that of quasi-static. At speeds between 20 and 40 m/s, there was a mix of shock and non-shock behavior, and there was a transition behavior between 40 and 50 m/s. At speeds greater than 50 m/s a clear shock behavior was interpreted and the results overall show that a shock will develop when the impact induces a stress that is higher than the initiation stress of the quasi-static case. These results are very similar to the experimental results, thus the final conclusion of this study was that micromechanically accurate models like that one can be used instead of experiments to generate the Hugoniot (Gaitanaros & Kyriakides, 2014b).

1.2.5 Finite Element Modeling

When generated appropriately, finite element models can be an extremely helpful tool in aiding scientists and engineers in performing tests that are otherwise not possible or feasible by experimental means. Since metal foams are highly engineered materials, using finite element methods to modify their material properties and observe their behavior is an efficient and economical technique to understand further how the material behaves. One of the most important properties of this material is that of relative density and even though there have been mathematical models that attempt to explain how the modification of this property affects the overall behavior of the material, experimental tests suggest that the material behavior is more complex than these mathematical models (Brooks H Smith, 2012).

Smith created a series of finite element models to understand how the microscopy of the HS steel foam affected the overall behavior of the materials. He achieved this by using the software ADINA, MATLAB, and different UNIX applications to compute random geometries and solve them by extracting common engineering graphs and values. In addition, a program called Metal Foams Simulator was developed to encompass the combinations of these software. Among these geometries were two algorithms that were created to model foams, one of them was a bulk material of some metal with random voids and the other a hollow sphere model (the one of interest) that consisted of randomly packed hollow spheres connected by small welds. The chosen method for stacking the spheres was that of random close-packing (or RCP) and it is precisely *randomly* that was shown to be the most accurate behavior of the spheres in packing and the “Modified Mechanical Contraction Method” was chosen to be used. The weld geometry presented to be a variable

that was a challenge due to the complexity of the real world manufacturing geometry that it exhibits. The necking from Figure 1.4 was simplified in the model by allowing a maximum overlap between the spheres as opposed to being joined by a neck, this proved to be a more realistic depiction of how the spheres behave experimentally due to the microscopy of the spheres that show a significant indentation of the spheres due to compaction (Brooks H Smith, 2012). It would have been a much more challenging task and used up computational cost to model individual necks for all spheres, thus this is shown in Figure 1.8. After the geometry was defined it was established that the material and model would be an elastic-plastic bilinear model with a Young's modulus of 200 GPa and a plastic modulus of 690 MPa. Elements were chosen to be second-order tetrahedral with maximum

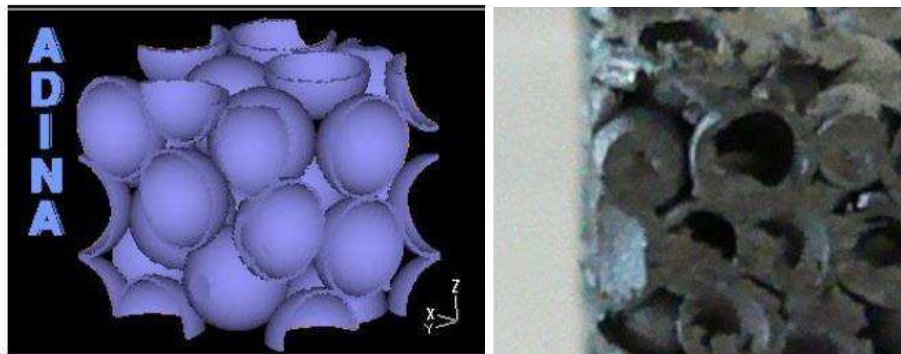


Figure 1.8: Hollow spheres geometry: sample geometry as generated (left); photograph of the experimentally-tested sintered hollow spheres steel foam (right) from (Brooks H Smith, 2012)

sizes approximately 60% of the sphere wall thickness because they accurately represented linear strain variations across three-dimensional geometries, something that is essential because the primary strength mechanism for the hollow spheres is their ability to resist bending (Brooks H Smith, 2012). Boundary conditions and loads for compression were applied to individual nodes, meshing was done, and once the preprocessing was complete, hours later the model was finished running. In the post-processing stage, nodal and element

values were exported to MATLAB to generate stress-strain curves by summing all positive reactions on both +z and -z faces and dividing by the original area to obtain engineering stress. The elastic modulus is calculated as the initial slope of this curve and 0.2% strain offset was applied to find yield stress (Brooks H Smith, 2012). More values were obtained from the model such as elastic and plastic Poisson's ratio, strains, and percentage of elements yielded.

The results of the hollow sphere tests were compared to (Gao, Yu, & Zhao, 2008) published values for validity purposes and then three simulation matrices were performed that tested the effects of geometric randomness upon the elastic modulus, the post-yield behavior with various geometric parameters, and the sensitivity of yield stresses and elastic moduli to various geometric parameters (Brooks H Smith, 2012). The initial validation tests showed yield strengths less than the experimental results (2.3 MPa vs. 3.1 MPa) and it was hypothesized that size effects could account for this 20% difference. The size effects correspond for example to the simulation's lengths of 2.5 void diameters to a side whereas the experimental measurements had 8 to 10 void diameters to a side, thus reducing the stress concentration in the simulation. It also showed that Young's modulus was much higher than expected (2560 MPa vs. 114 MPa) and the hypothesis for this was that the simulation had all weld diameters being a uniform 0.5 mm in size and the experimental measurements ranged from 0.08 mm to 0.5 mm.

The second set of validation was compared to that of Smith's experimental work. In this simulation, the 'overlap' weld was used and most inputs from earlier were used except for the microporosity (within the sphere walls) of 20% that was estimated and used for the base metal yield stress and elastic modulus to be reduced by this amount. The results

showed that the accuracy of the stress-strain curve in the computational model increased as the geometry/size of the sample cubes increased (multiple sizes were used). However, it was also found that the simulations overestimated the strengths and stiffnesses. The Poisson's ratio that was computed was somewhat inaccurate compared to the experimental tests overall. For the post-yield matrix, the results showed that elastic modulus and yield strength are both affected by the strength of the sphere walls, and will increase as the size of the spheres decrease or the wall thickness increases. This is fairly understandable seeing as how it was mentioned earlier the primary strength of the material is that of plate bending and bending resistance in the shell (Brooks H Smith, 2012).

Final conclusions by Smith based on the Metal Foams Simulator are that of validation tests show an accuracy to within 20% of experimental results, increasing in accuracy as simulation size is increased. Shown statistically, randomness may decrease the macroscopic stiffness of the material by up to 70% compared to deterministic simulations, showing the importance of randomness. The plastic hinging effect was demonstrated accurately in a sudden transition between two different Poisson's ratio behaviors. Finally, by analyzing the sensitivity of the foam it demonstrated the potential of simulations to determine the parameters that need to be altered to be able to produce and manufacture a desirable steel foam.

1.3 Experimental Testing

1.3.1 Introduction

Steel is a material that has been used for over a century and it evolved as a new material in response to iron and previously from masonry. Throughout history, building

materials have evolved and improved on through research and development. Metallic foam is a relatively new material in the field of material science whose properties are currently being researched for further understanding of material behavior and potential applications.

As previously stated, out of the three main types of steel foam the one that will be of focus in this thesis is that of hollow spheres. This section of the thesis is primarily focused on the experimental tests and research that was conducted. Keeping in mind that the purpose of this research is to expand the knowledge of hollow sphere steel foam and its mechanical properties, further motivation for this includes the hypothesis that the material is a worthy candidate for structural engineering applications in which energy absorption is of main interest. Hollow sphere steel foam is a compressible material whose mechanical advantages become apparent after it reaches its yield point and undergoes densification, where it starts to essentially recoup the material properties of solid steel and behaving like it. In contrast to solid steel, under a dynamic load, this densification phase allows for large amounts of energy to be dissipated and exhibit large strain hardening regions. It occurs when the individual spheres of the foam collapse during compression into each other simultaneously and cause an increase in energy dissipation and mechanical damping, thus allowing for multiple types of blast or impact applications.

This research of impact testing hollow sphere steel foams was carried out in the spring and the fall of 2015 to measure stress-strain properties of the foam under the impact of a mass. From these tests, multiple characteristics were measured and studied, which include stress-strain relationship and its comparison to quasi-static compressive behavior, strain rate, energy absorption capacity, among others.

1.3.2 Materials and Methods



Figure 1.9: Pre-cut samples of aluminum foam



Figure 1.10: Instron dynatup 8250 impact testing machine and set-up



Figure 1.11: Impactor with mass



Figure 1.12: Samples of HS steel foam pre-impact testing

Various HS steel foam blocks measuring approximately 50mm by 50mm in length and width were acquired from the Fraunhofer Institute for Advanced Materials (IFAM) in Dresden, Germany. This particular steel foam is composed of a mild steel of between 0.3% and 0.5% carbon (Szyniszewski et al., 2014). Even though the manufacturing process randomly distributes the spheres, this foam is considered to be an isotropic material, therefore testing is justified in any load direction and application. After the blocks were



Figure 1.13: 4,500 fps high-speed camera and lighting



Figure 1.14: Samples of HS steel foam post-impact testing acquired, twelve samples were cut and the best nine of those were used in the tests. These nine optimal samples correspond to the visual geometry that they exhibit, such as straight

and parallel faces, in order to best capture the force applied from the impacting mass on the surface area of the top face. Before cutting the samples, measurements were taken with a field ruler of each block and lines were marked along the samples of where cutting was to take place with a black marker, as seen in Figure 1.9 (for aluminum foam), exercising care in detailing the lines parallel to the edges of the foam. Because of the symmetry in the blocks, dividing into halves was the optimal choice and for a given height of approximately 25mm in the base block of foam, four samples could be extracted. In the following Section 1.3.3.1 Measurements and Geometry the measurements of the sample geometry are shown, indicating both prior and post-testing. The samples were cut at Guinness Laboratory in the University of Massachusetts Amherst using a band saw by running the samples along the dimensioned lines as straight and fluidly as possible. The overhead clearance of the band saw was set at less than 1 cm from the sample in order to reduce unwanted vibration from the procedure that could alter the sample cutting process and produce non-consistent and contorted cuts. After the samples were extracted, their mass was recorded using a digital scale to obtain relative density data. Measurements of the samples were performed with a digital caliper in Kaven Hall at Worcester Polytechnic Institute in four directions of the loading direction (height), two in width, and two in length. In total, twelve steel foam samples were cut and dimensioned at approximately 15 cm³ to be tested at three different drop heights using the Instron dynatup 8250 impact testing machine, as seen in Figure 1.10. The foam samples were selectively chosen to be those that exhibited the best visual characteristics for the impact. These characteristics were considered to be those of visually exhibiting the most cube-like appearance to them, meaning that the faces of the sample were straight and parallel.

Three sets of tests consisting of three samples each were performed based on a variation in drop height of the 31.97 lbs mass, seen in orange on Figure 1.11: Impactor with mass. The first set was performed at a maximum height of 928 mm, then the height was reduced to 747mm, and the final set was at a drop height of 520 mm. In the analysis of results, the latter set of results was deemed as undesirable data in the force output. Oscillations were minimally present and not enough to distinguish one test from another. Additionally, in these tests, the moduli of elasticity were calculated to being very different from one another. Therefore, the height was later reproduced at a future date to be at 530 mm, approximating that initial low drop height as best as we could. Since these new results came out acceptable, the set of 520 mm was ruled out and the set of 530 mm replaced it for the low height set of data. In this thesis, the set of 530 mm is what is used. To optimize the results, the faces of the cubes that appeared most parallel were selected to be in the vertical loading direction. Lighting was adjusted accordingly to produce the best video rendering, thus making it better for displacement analysis, resulting in strain data. Initially, in addition to registering the impact force, this machine also registered energy, velocity, and displacement data but it was later found that only the force data was reliable. Using the 4,500 frames-per-second high-speed video camera seen in Figure 1.13, displacements were obtained using a frame-by-frame analysis (in this thesis this analysis is referred to as the “methodological” or “FBF” because a television was used for gathering displacement data going frame-by-frame due to its large display and optimal resolution), and as a result, strain was also obtained through this method. Finally, after the data and videos were obtained from the impact machine and camera, respectively, the new and deformed geometry of the samples was measured at the positions that they were obtained from initially, four height

measurements at each corner of the sample, two width measurements, and two length measurements, as well as photographed, as seen in Figure 1.14: Samples of HS steel foam post-impact testing and in Section 1.3.3.1 Measurements and Geometry. These locations for the measurements of each sample were strategically chosen in order to get an accurate representation for the geometry of the samples.

1.3.3 Results and Analysis

1.3.3.1 Measurements and Geometry

928 mm

Table 1.2: Geometry of the samples for drop height of 928 mm prior to impact

Sample geometry prior to impact [mm]											
Sample	h_1	h_2	h_3	h_4	w_1	w_2	w_3	w_4	Mass [g]	Density [kg/m ³]	Drop height [mm]
1	23.8	24.2	24.0	24.5	27.9	27.8	25.8	25.7	20.5	1184.9	928.0
2	24.3	23.7	23.6	24.0	27.2	26.8	26.0	26.0	19.1	1138.4	
3	24.3	24.4	24.1	24.0	27.6	27.4	25.4	25.5	19.9	1174.9	

Table 1.3: Geometry of the samples for drop height of 928 mm post-impact

Sample geometry post impact [mm]											
Sample	h_1'	h_2'	h_3'	h_4'	w_1'	w_2'	w_3'	w_4'	Mass [g]	Density [kg/m ³]	Drop height [mm]
1	14.4	14.6	14.3	14.4	29.9	29.9	27.3	27.4	20.5	1737.8	928.0
2	13.5	13.7	13.6	13.6	28.7	29.4	27.6	27.8	19.1	1745.3	
3	14.0	13.9	13.9	14.1	29.6	29.4	27.4	27.3	19.9	1764.9	

Table 1.4: Measured strain of set of samples for drop height of 928 mm

Strain, ϵ , in the -z direction					
Sample	h_1'	h_2'	h_3'	h_4'	Average ϵ
1	0.39	0.40	0.40	0.41	0.402

2	0.44	0.42	0.42	0.43	0.431
3	0.42	0.43	0.42	0.41	0.422

747 mm

Table 1.5: Geometry of the samples for drop height of 747 mm prior to impact

Sample geometry prior to impact [mm]											
Sample	h_1	h_2	h_3	h_4	w_1	w_2	w_3	w_4	Mass [g]	Density [kg/m ³]	Drop height [mm]
1	24.6	24.4	24.4	24.2	26.3	26.4	25.8	25.6	19.4	1174.1	
2	23.8	24.0	23.5	24.0	26.9	27.1	26.0	26.2	20.0	1191.2	747.0
3	24.4	24.7	24.7	24.4	27.4	27.6	26.0	25.4	20.3	1170.0	

Table 1.6: Geometry of the samples for drop height of 747 mm post-impact

Sample geometry post impact [mm]											
Sample	h_1'	h_2'	h_3'	h_4'	w_1'	w_2'	w_3'	w_4'	Mass [g]	Density [kg/m ³]	Drop height [mm]
1	16.1	15.9	15.8	16.0	28.5	28.0	27.8	27.5	19.4	1557.1	
2	15.9	16.1	16.0	16.0	28.7	28.3	27.1	27.3	20.0	1612.5	747.0
3	16.7	16.3	16.4	16.5	29.0	29.0	27.5	26.7	20.3	1567.8	

Table 1.7: Measured strain of set of samples for drop height of 747 mm

Strain, ϵ , in the -z direction					
Sample	h_1'	h_2'	h_3'	h_4'	Average ϵ
1	0.35	0.35	0.35	0.34	0.346
2	0.33	0.33	0.32	0.33	0.328
3	0.32	0.34	0.34	0.32	0.329

530 mm

Table 1.8: Geometry of the samples for drop height of 530 mm prior to impact

Sample geometry prior to impact [mm]											
Sample	h_1	h_2	h_3	h_4	w_1	w_2	w_3	w_4	Mass [g]	Density [kg/m ³]	Drop height [mm]
1	28.1	27.8	27.7	27.9	27.1	26.6	26.1	26.3	22.8	1162.7	530.0

2	27.7	27.8	27.8	27.5	26.4	27.1	25.8	26.1	21.8	1133.7
3	29.2	28.6	28.2	28.5	26.2	26.7	24.9	24.5	21.6	1155.0

Table 1.9: Geometry of the samples for drop height of 530 mm post-impact

Sample geometry post impact [mm]											
Sample	h_1'	h_2'	h_3'	h_4'	w_1'	w_2'	w_3'	w_4'	Mass [g]	Density [kg/m ³]	Drop height [mm]
1	21.8	21.8	21.7	21.8	28.7	27.2	27.0	26.8	22.8	1392.7	530.0
2	21.2	21.1	21.2	21.0	27.0	28.5	26.4	26.7	21.8	1400.7	
3	22.1	21.9	21.9	22.0	26.1	26.6	25.1	24.7	21.6	1498.1	

Table 1.10: Measured strain of set of samples for drop height of 530 mm

Strain, ϵ , in the -z direction					
Sample	h_1'	h_2'	h_3'	h_4'	Average ϵ
1	0.22	0.22	0.22	0.22	0.219
2	0.23	0.24	0.24	0.24	0.237
3	0.24	0.23	0.22	0.23	0.232

1.3.3.2 Stress vs. Time

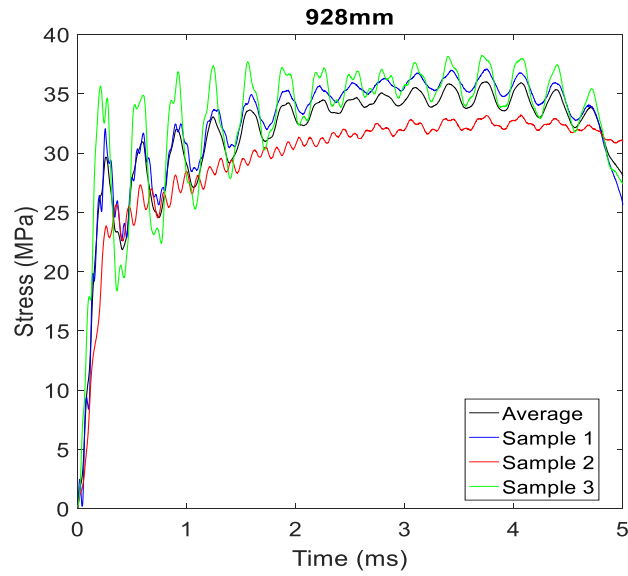


Figure 1.15: Stress vs. time for drop height of 928 mm

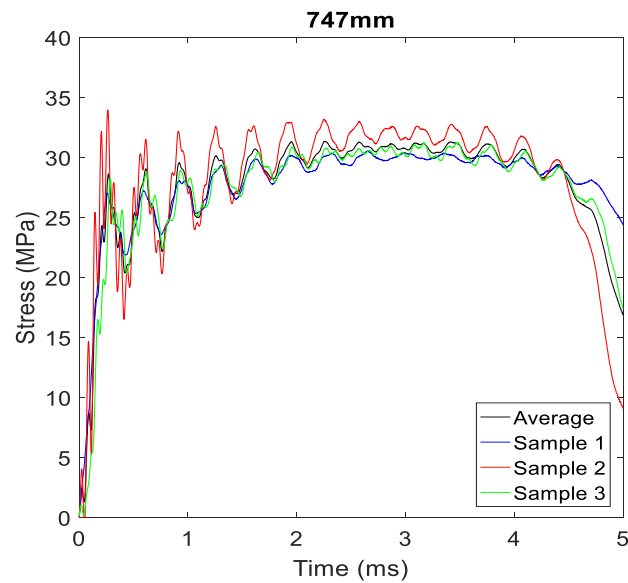


Figure 1.16: Stress vs. time for drop height of 747 mm

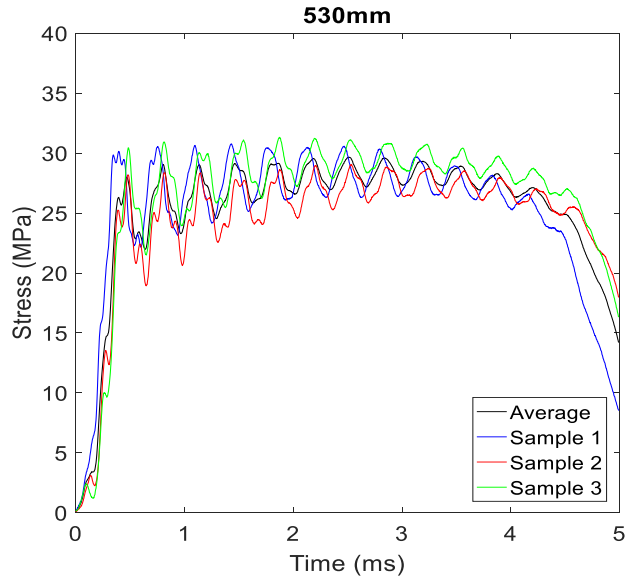


Figure 1.17: Stress vs. time for drop height of 530 mm

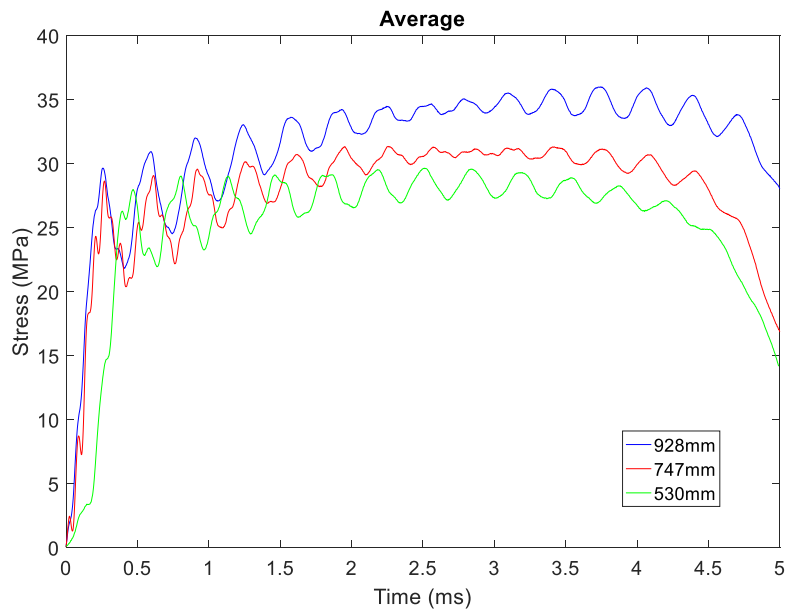


Figure 1.18: Average stress vs. time from all drop heights

Figure 1.15 thru Figure 1.17 show the stress vs. time plots that were generated as a result of the impact tests from each of the three drop heights of 928 mm, 747 mm, and 530 mm. From the output data of force, stresses were calculated as the force applied per cross-sectional area, this area was taken to be the top surface of the sample where the mass impacts the sample. Time was recorded by the machine in increments of 0.002 milliseconds. Each drop height contained three samples to distinguish any variability between them. For each of these three drop heights, an average force of samples within each set of drop heights was calculated and it is shown in Figure 1.18. As hypothesized, a higher drop height yields greater yield stresses and a greater strain hardening region, thus a greater amount of energy being absorbed, this coincides with (Paul & Ramamurty, 2000). The elastic region lasts for less than half of a millisecond under this dynamic impact load and after this point, the plateau stress remains fairly constant during the duration of the impact, and interestingly enough the stress drops down again to zero. This behavior varies greatly to that of quasi-static loading which is examined further in a later section. For each of the three drop heights, the impact duration is something that should be noted because of its very short span of fewer than 5 milliseconds and it is clear from Figure 1.19 that after the impact duration when the force reduces to zero, the oscillations appear to cease to exist. For the next millisecond, where it appears that the oscillations end, the material is fully crushed and the mass rebounds back.

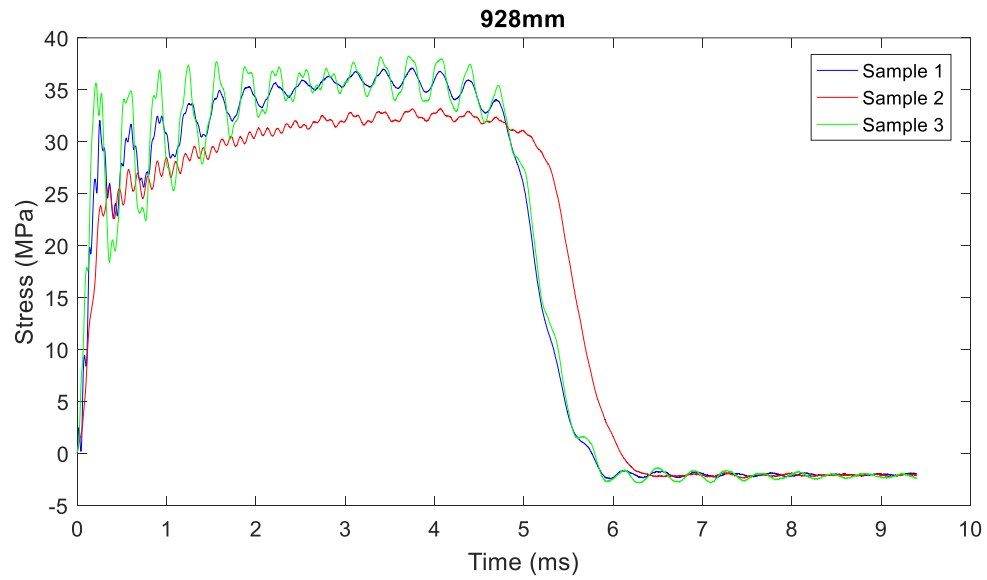


Figure 1.19: Entire duration of data capture of stress vs. time for drop height of 928 mm

In addition, it is clear that there are oscillations throughout the impact. We hypothesize that these oscillations represent frequencies in the equipment rather than in the foams and this is examined in a section later on. By impacting the material, a step change in load sets up a wave. In this experiment, the initial impact causes the load but the load continues to be applied, so it is interesting to note that the period of the oscillations visually remains similar throughout the impact, when it might be expected that the period should increase along the impact. This phenomenon is examined more in depth later on.

1.3.3.3 Stress vs. Strain

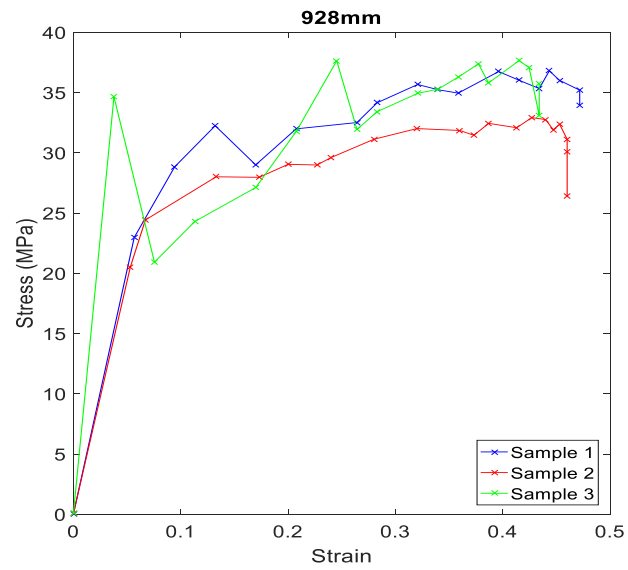


Figure 1.20: Stress vs. strain for drop height of 928 mm

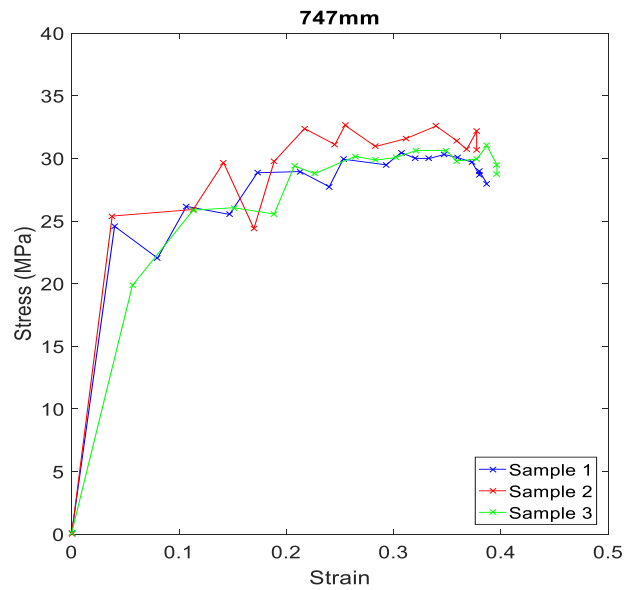


Figure 1.21: Stress vs. strain for drop height of 747 mm

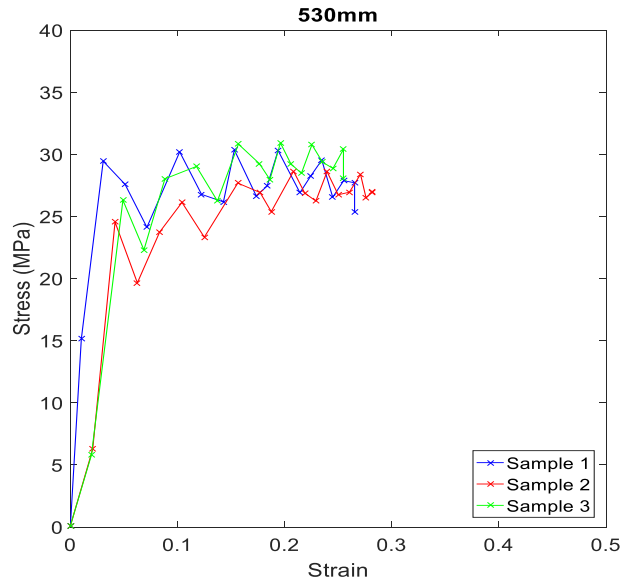


Figure 1.22: Stress vs. strain for drop height of 530 mm

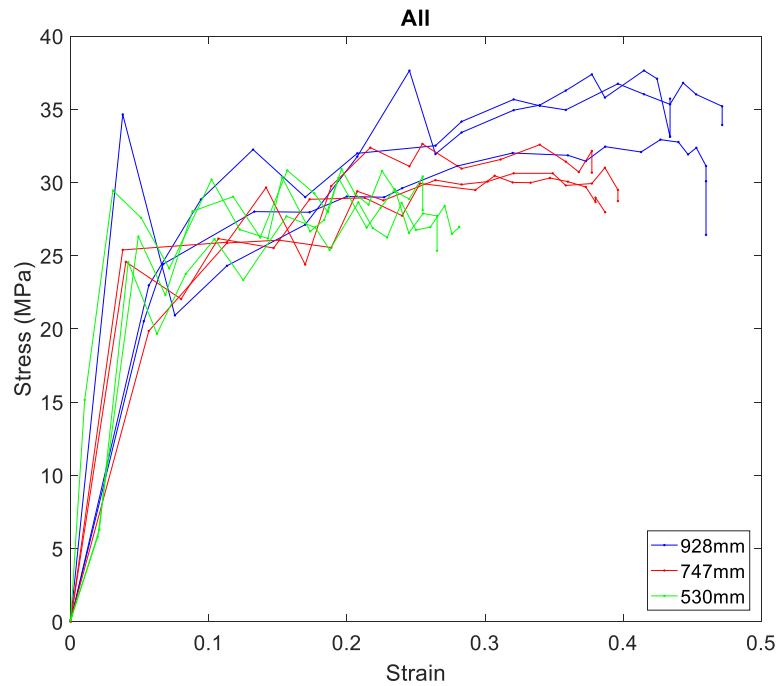


Figure 1.23: Stress vs. strain for all drop heights

In order to understand material properties of any material, stress vs. strain is a critical place to begin with. In Figure 1.20 thru Figure 1.23, stress was calculated from the output of the machine reading impact force and was divided per unit area of the samples. The stress levels are the same from the stress vs. time plots as here and the variation is time to strain. The output data for each sample of force was in the units of lbf and it was converted to N for the purpose of this study. Furthermore, to get it into units of stress, each sample had particular individual cross-sectional dimensions that were measured prior to testing and as a result, the plots display MPa as the calculated unit of stress.

The strain was calculated as the amount of deformation in the vertical direction (due to the load direction) per the initial length of the sample using a displacement analysis method. This method, referred to as “methodological” or “FBF” (frame-by-frame) in this thesis, consists of using the high frame rate videos of the experiments to measure displacements along the dynamic impact. Each experiment was recorded individually by video as well as by output of data. Since they are recorded on separate instruments, the objective is to synchronize them manually in order to accomplish the task at hand of measuring strain. The Instron dynatup 8250 machine began recording data at the moment of impact, any previous video before that is irrelevant, therefore the method began at the frame where there was no deformation of the sample and was set as the reference point (different for every sample for every drop height). To calculate the strain, the video had to be proportioned to a size that could be measured; a large television was used for this. Using a large television, the height of the sample was measured using a field ruler and compared to the actual geometry of the sample. After, displacement measurements were taken frame-by-frame using the field ruler and, as a result, were proportionately calculated in every

frame during the impact of the actual deformation that the sample underwent during the impact duration. Having both the actual initial height of the sample and the incremental displacements for every frame, the strain was calculated as a result.

At this point, there was a large set of data of stress at very small time intervals throughout the duration of the impact and beyond; there was also a much smaller set of data of strain at larger time intervals throughout the duration of the impact. The oscillations shown in Section 1.3.3.2 Stress vs. Time can be attributed for the range of stress data for these graphs, as they are largely variable, with respect to the strain data. The first point in the force output data is the first moment of impact, therefore it corresponded to a strain of 0 and thus the stress and strain could begin to be synchronized. Each frame of the video corresponded to a time interval on the force output data of 0.222 ms or 0.444 ms. The interval between frames is meant to be 0.222 ms but the camera has a recurring error of not registering every frame at that exact time, rather it skips the chronological frame visually, but still registers it as a real “frame” as it is labeled on the videos. Chronologically on the FBF method, this corresponded to a certain duration of impact time with documented time intervals, therefore these times were individually and manually sought out on the force output data and so finally a stress vs. strain plot was obtained for three samples at three different heights. Having multiple samples for multiple drop heights enables us to filter through variability and error to pick out optimal samples and calculate corresponding properties.

1.3.3.4 Comparison to Quasi-static Behavior

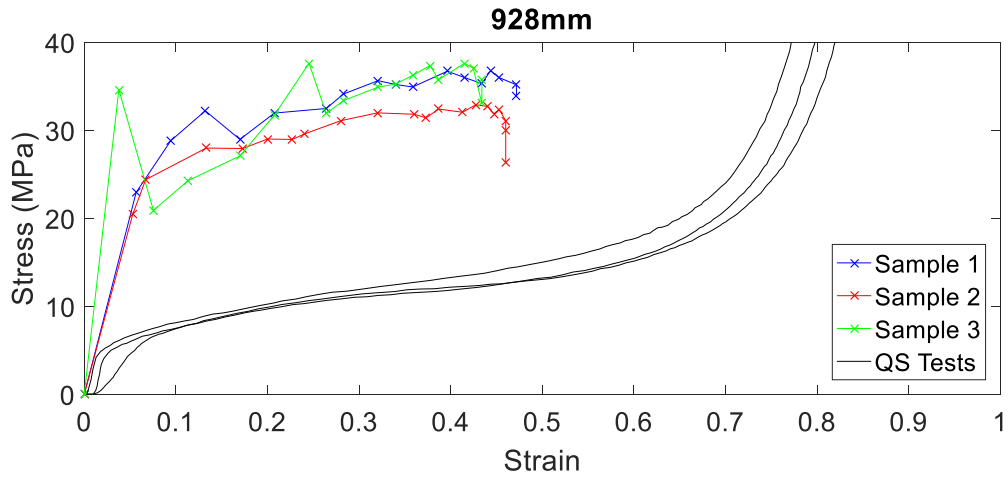


Figure 1.24: Comparison of impact to quasi-static behavior for drop height of 928 mm

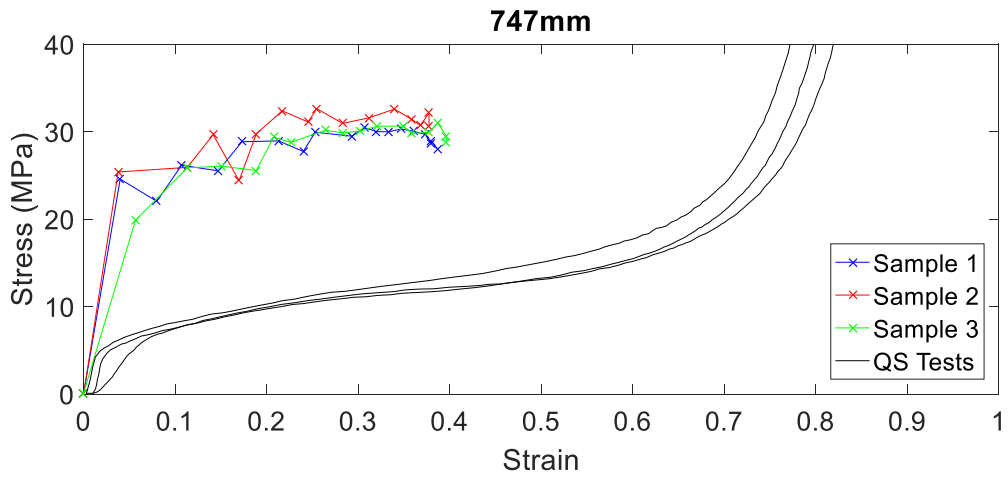


Figure 1.25: Comparison of impact to quasi-static behavior for drop height of 747 mm

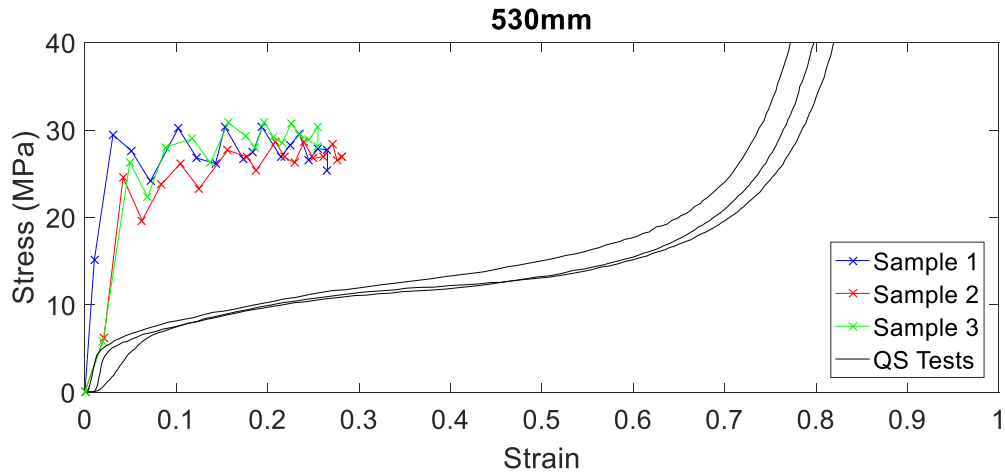


Figure 1.26: Comparison of impact to quasi-static behavior for drop height of 530 mm

Three quasi-static loading tests were conducted by Smith to obtain multiple material properties as seen in Figure 1.5. The samples exhibited relative densities of 14-15%, similar to those measured in this work, and were loaded uniaxially at strain rates of 0.003/min and 0.015/min. To compare this behavior to impact response a software was used to digitize the values from Figure 1.5 and superimpose them onto Figure 1.20 thru Figure 1.22, yielding in Figure 1.24 thru Figure 1.26 where the visual comparison is demonstrated. Visually, it is clear that both of these tests yield different results due to their loading mechanisms. Subjecting the steel foam to an impact load increases the yield stress of the material substantially and becomes more pronounced. When the videos are observed for the dynamic impact it is clear that the mechanism of collapse is non-uniform and collapses by forming “bands” across the sample. Similarly, this is observed as well during quasi-static loading. The strain hardening regions are comparable to one another in terms of the hardening modulus but as for duration, the quasi-static loading develops hardening for a longer period of time. The most significant difference other than the yield stresses is

the ultimate stress point. In the dynamic loading, it appears that the material does not reach an ultimate stress the same way that the quasi-static does, rather it reaches its yield point and hardens at a higher but similar stress value. Whereas in the quasi-static loading, the tests display a behavior of a densification region after approximately a strain value of 0.6. The reason for this can be attributed to the fact that in quasi-static loading conditions the material continues to crush even after it is fully compressed. Also, by having a slow compression, the material is forced to develop strains in a greater amount of time. Another attribute to this is the material properties. It is clear from the figures that for this steel foam, the strain does not reach the densification strain of 0.65, rather it develops strains quicker due to its high yield stress and therefore absorbs a great deal of energy. The other part of this research carried out by Andrew Rock consists of researching aluminum open cell foams under the same dynamic load. Interestingly enough, he found that for aluminum open cell foam the behavior did closely resemble that of quasi-static loading, as seen in Figure 1.27, with a clear hardening and densification region, the main difference was elevated stress levels. It is important to note his experiments because they were periodically checked with and against the steel foam experiments due to the similarities in approach of methods and calculations.

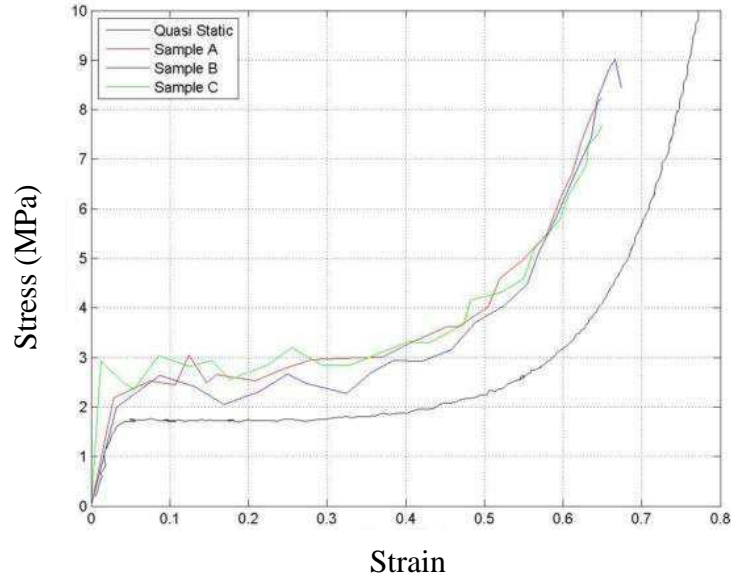


Figure 1.27: Stress vs. strain curve for 20 ppi specimens with quasi-static data superimposed by (Rock, 2016)

In the dynamic impact, the mass rebounds off of the material after it is crushed to its potential based on a number of factors such as the weight of the mass and the height it is being dropped at. This enables the output to have more data for stress-strain and is more exact; in contrast to quasi-static, where strain develops slower and more pronounced. Although the data for the quasi-static is more reliable it would be interesting to compare the strain energy absorbed by this system and compare to the strain energy absorbed by the impact tests. Quasi-static loading is more reliable due to the fact that it is more reproducible as seen from the plots, there is large variability in the stress-strain behavior of dynamic impact. This variability is accounted to the fact that it is dynamic and fast, and of course, the FBF analysis method which is much different than having a strain gauge attached to the samples and deforming at a much slower rate.

1.3.3.5 Strain Rate

Table 1.11: Comparison of methodological (FBF) strain and measured strain for drop height of 928mm

Drop height: 928mm					
Sample	Time of Impact [ms]	Final Strain (FBF)	Final Strain (measured)	Strain Rate (FBF) [1/ms]	Strain Rate (measured) [1/ms]
1	4.444	0.472	0.402	106.2	90.5
2	4.889	0.460	0.431	94.1	88.2
3	4.222	0.434	0.422	102.8	100.0
Average	4.518	0.455	0.418	101.0	92.9
Standard Dev.	0.277	0.016	0.012	5.1	5.1

Table 1.12: Comparison of methodological (FBF) strain and measured strain for drop height of 747mm

Drop height: 747mm					
Sample	Time of Impact [ms]	Final Strain (FBF)	Final Strain (measured)	Strain Rate (FBF) [1/ms]	Strain Rate (measured) [1/ms]
1	4.667	0.387	0.346	82.9	74.1
2	3.778	0.377	0.328	99.8	86.8
3	4.000	0.396	0.329	99.0	82.3
Average	4.148	0.387	0.334	93.9	81.1
Standard Dev.	0.378	0.008	0.008	7.8	5.2

Table 1.13: Comparison of methodological (FBF) strain and measured strain for drop height of 530mm

Drop height: 530mm					
Sample	Time of Impact [ms]	Final Strain (FBF)	Final Strain (measured)	Strain Rate (FBF) [1/ms]	Strain Rate (measured) [1/ms]
1	3.778	0.265	0.219	70.1	58.0
2	4.000	0.281	0.237	70.3	59.3
3	3.556	0.255	0.232	71.7	65.2
Average	3.778	0.267	0.229	70.7	60.8
Standard Dev.	0.181	0.011	0.008	0.7	3.2

Table 1.11 thru Table 1.13 show the strain rates that were calculated using two methods. Understanding how strain rate is related to certain materials is important in order to make appropriate judgments for how the material will be applied. As stated, there are two ways that the strains were calculated as shown, using the frame-by-frame (FBF) analysis method and from measuring the samples before and after impact and using the time from the data, as seen earlier in Table 1.4, Table 1.7, and Table 1.10. Within each set of data for drop heights, the calculated strain rates appear to be more consistent and have less variation because it is less prone to errors, seeing as there are only initial and final measurements of the samples that are taken to obtain the total strain value. Although, this is prone to less errors, it also does not fully capture the strain behavior as desired. In the frame-by-frame analysis method, the strain is calculated from displacements measured at each frame of the video and when taking measurements down from one frame it translates to the next frame, having this method be more susceptible to errors.

In a ballistic blast case reported by (Ramesh, 2008) it is noted that the substantial parts of deformation occur at strain rates as low as 10^2 s^{-1} and that significant parts of the damage that occur as a result of the events reported might be a result of the lower strain rate deformations. The values reported in Table 1.11 thru Table 1.13 are lower than that of 10^2 s^{-1} but that is because those are average strain rate values for a given duration time of impact. This behavior is expected because of the way that the foam behaves under compressive forces with the strain rate being high relative to the impact due to the initiation of the impact, and it slowing down and decreasing as energy gets dissipated.

1.3.3.6 Yield Stress and Elastic Modulus

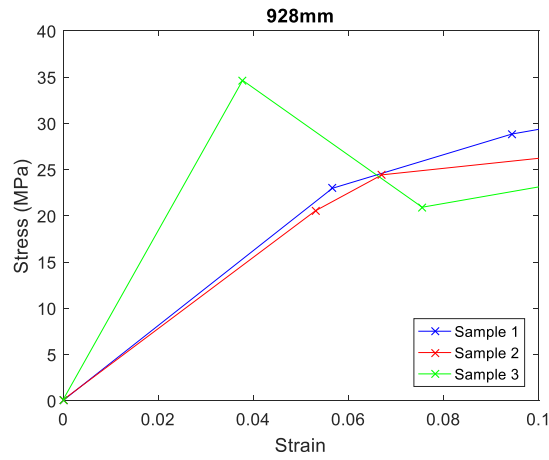


Figure 1.28: Linear, elastic region for drop height of 928 mm showing the yield point

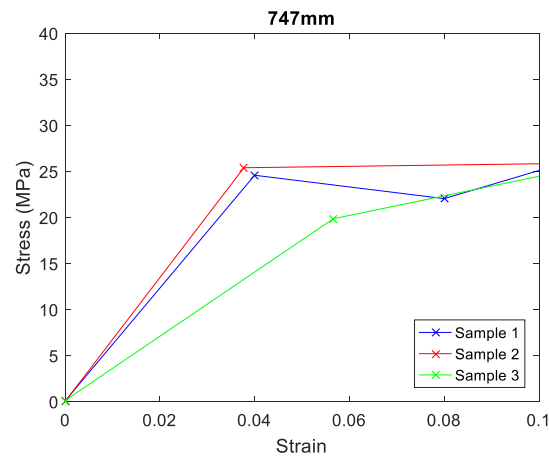


Figure 1.29: Linear, elastic region for drop height of 747 mm showing the yield point

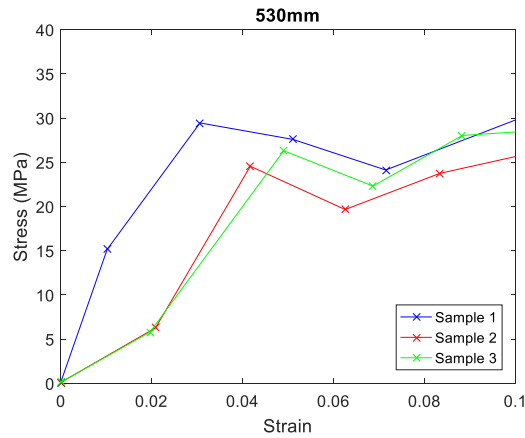


Figure 1.30: Linear, elastic region for drop height of 530 mm showing the yield point

Table 1.14: Elastic modulus for every sample for all drop heights

Drop height [mm]	Sample	Elastic modulus [MPa]	Average [MPa]	Maximum [MPa]	Minimum [MPa]
928	1	405.4	568.9	915.5	385.7
	2	385.7			
	3	915.5			
747	1	612.9	544.9	672.8	348.8
	2	672.8			
	3	348.8			
530	1	958.4	693.2	958.4	534.3
	2	587.0			
	3	534.3			

After the stress vs. strain plots were done it was possible to go into the data and analyze it further. The yield stress and elastic moduli were calculated based on the data and plots from Section 1.3.3.2 Stress vs. Time. The yield stress plots are shown on Figure 1.28 thru Figure 1.30, as a magnified view of the stress-strain plots, with the yield stress being taken to be the first point after initial impact and for the 530 mm drop height the second data point. The yield point was taken to be as such because of the difference in stress with the next data point. In the 530 mm data set, the stress levels become relatively

constant starting at the third data point. This was as such because of the fundamental stress vs. strain plots that this data resembled. At such a short duration for this very fast impact, for these experiments, it was difficult to establish the yield stress because of the lack of data points, which is proportional to the number of frames for the impact on the videos. Using the FBF method, a camera with a higher frame rate would prove to be much more beneficial, the only problem is that it sacrifices video resolution.

As a result, both the yield stresses and the elastic moduli values varied for a given sample drop height. This is attributed to the variability of displacement measurements, which in turn, is the strain measurements. For example, in the all of the drop heights two samples out of three closely resemble one another in terms of elastic modulus and yield stress; and the third has a different value, relatively speaking. Only three samples were used for each drop height and it evident how as more samples that are tested, more and better results are obtained.

1.3.3.7 Energy Absorption Capacity

Table 1.15: Energy absorbed per m^3 for all drop heights

Drop height [mm]	Sample	Strain energy (computed) [MJ/m ³]	Average [MJ/m ³]	Maximum [MJ/m ³]	Minimum [MJ/m ³]
928	1	14.3	13.3	14.3	12.6
	2	12.6			
	3	13.1			
747	1	10.1	10.2	10.4	10.0
	2	10.4			
	3	10.0			
530	1	7.0	6.6	7.0	6.3
	2	6.5			
	3	6.3			

Table 1.16: Total energy absorbed for all drop heights

Drop height [mm]	Sample	Strain energy (computed) [J]	Average [J]	Maximum [J]	Minimum [J]
928	1	256.8	234.0	256.8	215.0
	2	215.0			
	3	230.2			
747	1	169.7	176.2	180.8	169.7
	2	178.3			
	3	180.8			
530	1	139.0	130.2	139.0	123.8
	2	127.9			
	3	123.8			

There has been some research with regards to high strain rate energy absorption upon aluminum foams as illustrated in (Cardoso & Oliveira, 2010) but not as much upon HS steel foams, which makes comparison analyses a challenge. Nevertheless, to calculate the strain energy that was absorbed during the impact, Figure 1.20 thru Figure 1.22 were used as they show the material stress-strain response. The stress-strain response of a material inherently provides the energy absorption of the material as a result of unit analysis. It is known that the majority of the absorption energy comes from when the material is being deformed as it converts kinetic energy into plastic deformation energy. In the stress-strain curves in Figure 1.20 thru Figure 1.22, this is seen where the stress levels remain relatively constant. At a microscopic level, the cell walls and in the case of HS steel foam, the spheres, begin to collapse by crushing individually and then translates to the adjacent spheres, forming longitudinal bands. Nevertheless, the area under the stress-strain curves provide the energy absorption and this can be seen with unit analysis and in Equation (1). The analysis results in units of work energy per volume of material (J/m^3).

$$U^* = \frac{1}{V} \int P dL = \int_0^L \frac{P}{A_0 L_0} dL = \int_0^\varepsilon \sigma d\varepsilon \quad (1)$$

Energy absorption was calculated via MATLAB using the `trapz` function whose function is to integrate a function that is given to the program to plot. It integrates said function by performing a trapezoidal analysis with the given points of the curve, the results are illustrated in Table 1.15: Energy absorbed per m³ for all drop heights and Table 1.16. Having multiple heights further reinforces that the energy absorption calculations and analyses were performed satisfactorily due to the small amount of error within the energy absorbed within each height. For energy absorption per m³, the results yielded that the hollow sphere steel foam absorbed between 5 and 6 times the amount that of aluminum open cell foam.

These HS steel foam tests were conducted consequently with the open-cell aluminum foam tests by (Rock, 2016). In his tests, the same drop heights were used using aluminum foam. For comparison purposes, total energy absorbed (not per unit volume) between both sets were calculated and analyzed; this concluded that a small difference of an average 18% between both sets of test was present and this can be attributed to errors in analyzing the strain data with different methods. This translates directly to the stress-strain plots because the `trapz` function in MATLAB was used to calculate the energy absorbed.

1.3.3.8 Compression Waves

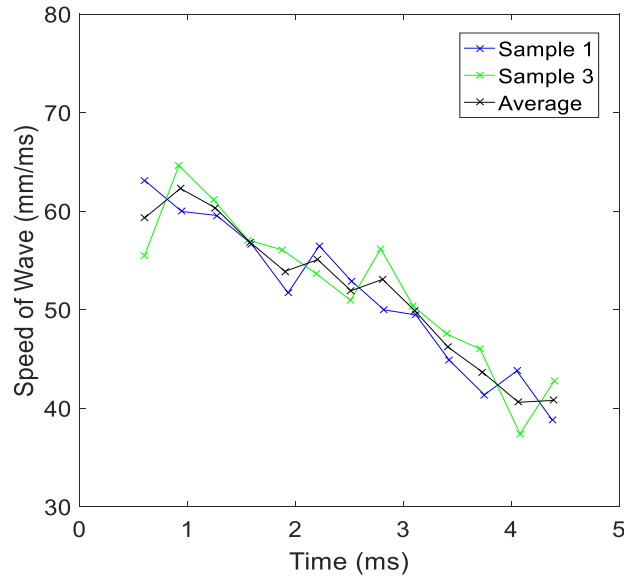


Figure 1.31: Wave speeds within the samples for drop height of 928 mm

Note: The data output in the plot did not clearly represent distinctive crests and troughs enough to calculate for period in sample 2 for this drop height.

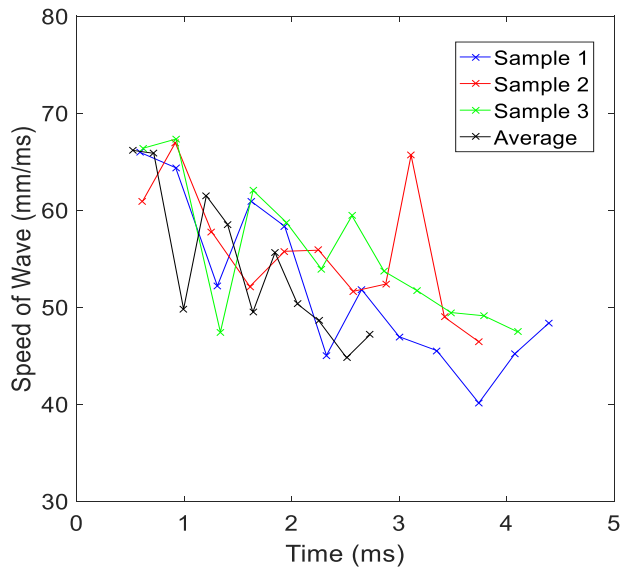


Figure 1.32: Wave speeds within the samples for drop height of 747 mm

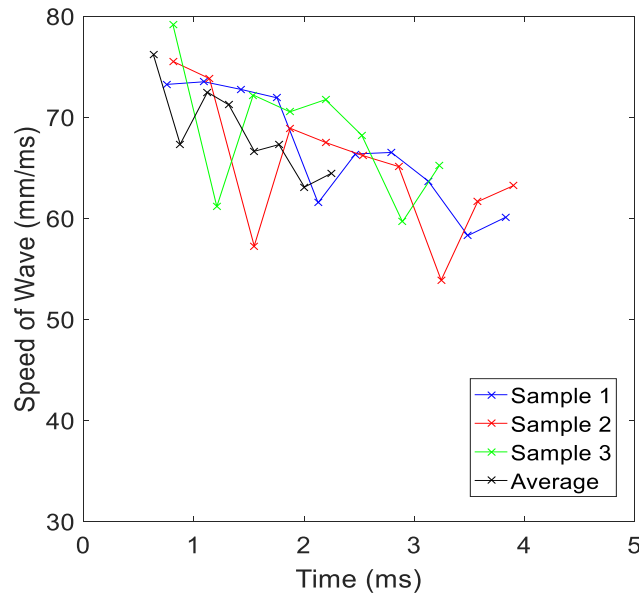


Figure 1.33: Wave speeds within the samples for drop height of 530 mm

The pressure waves of the tests are characterized by the oscillations that occur in the stress vs. time behavior exhibited in Figure 1.15 thru Figure 1.17 and so the purpose of this section is to determine the origin of these oscillations and what they can be attributed to. We know for sure that these waves are a result of the samples being compressed because they occur for the impact duration and cease to exist towards the end at approximately 4.5 ms. Therefore, it was hypothesized that the p-waves could come from the samples themselves or a natural frequency of the testing equipment, like the impact machine itself. For this study, the p-waves values are based on crest to crest periods and are particular to each sample because of the variation in sample geometry and microscopy. In order to calculate wave speed, the sample height must be obtained at every particular time period where there is a crest along the stress data and divide it by the period of the wave for that time instance. The period of the wave is measured in milliseconds and it is the difference

between times at which the crests occur, sequentially. The height of the sample at every occurrence for every sequential oscillation is calculated using the method of double linear interpolation. The reason for this is because the video of the impact for every sample captures the impact every 0.222 or 0.444 ms, and the height of the sample occurs generally in between frames. So in order to calculate the (interpolated) height of the sample, the displacement data from the FBF method is used, which inherently provides the time data for every displacement that is measured. First, the time at which the oscillations occur must be identified from Figure 1.15 thru Figure 1.17. Next, the displacement data that was obtained from the FBF method in Section

1.3.3.3 Stress vs. Strain) must be referenced. Finally, to obtain the height of the sample at the oscillations' crests, the double interpolation method must be used, thereby interpolating between FBF's *time* and *displacement*, matching it up with the crests' *time* that was identified, resulting in an interpolated *height*, assuming linear interpolation. After this set of calculations is completed, the results are the *height* of sample and the *period* of wave, in which dividing one by the other results in the *speed* of wave with units: mm/ms.

It can be concluded from Figure 1.31: Wave speeds within the samples for drop height of 928 mm thru Figure 1.33: Wave speeds within the samples for drop height of 530 mm that, overall, the periods do change throughout the impacts, and in a linear fashion. As the samples strain and crush, their total height decreases, thus reducing the distance that a

p-wave would need to travel from the initial impact at the top surface to the bottom surface where the steel plate lies. Due to this, we initially speculated that the sinusoidal oscillations represent natural frequencies of the machinery equipment meaning that the speed of the p-wave would have to increase throughout the impact due to the samples' reduction in height. However, our results indicate that the periods decrease linearly during strain hardening as seen in Figure 1.31: Wave speeds within the samples for drop height of 928 mm thru Figure 1.33: Wave speeds within the samples for drop height of 530 mm. In addition, wave amplitude should be noted, in that there is a decrease in amplification during strain hardening as well, and can be seen in Figure 1.15 thru Figure 1.17 more specifically during the times of 2.5 - 3.5 ms. At this point of the impact duration is where the stresses are at their maximums, interestingly enough. As a result, it is concluded that the oscillations are therefore not in the samples of steel foams due to the decreasing wave speed and the period of the waves remaining relatively constant.

1.3.4 Conclusions

Previous to the experimental analyses, the hypothesis stood as that HS steel foam is a worthy candidate for structural engineering applications and this is confirmed by the tests, from the energy absorption capacity they have. Compared with aluminum foams that were tested dynamically with the same preparations and executions, steel foams showed that energy absorption per m^3 was approximately 5 to 6 times greater. This is directly related to the region of strain hardening, which the experimental results showed that it extends for the majority of the impact duration. Other conclusions to be drawn from the experimental data is that the samples among higher potential energies yielded larger kinetic

energies, as expected due to the conservation of energy, and this was one of those checks to make sure that data extraction and analysis was being done correctly.

A very important comparison was done with the quasi-static experiments conducted by Smith and the results indicated that impact loading on the material increased the yield stress by approximately 5-6 times, but the strain was reduced by more than half of the quasi-static experiments. Thus, the dynamic experiments were not able to reach the densification strain of approximately 0.6. This is attributed to the difference in duration of crushing where for quasi-static strains can develop more pronounced over longer periods of time and densification is only present in the quasi-static experiments because the material continues to crush after it has been fully crushed. Similarities within the two types of experiments were observed in that the material crushes by forming horizontal bands along the length and width of the sample. This is interpreted by the buckling of local spheres and propagating that into adjacent spheres.

One of the first observations from the output data were the oscillations occurring in the stress-time plots and it was hypothesized that they represented frequencies in the testing equipment as opposed to in the foams themselves. After performing a study on these compression waves, it was concluded that they were not in the steel foam after all due to the decreasing wave speed and constant period of the waves. Therefore, the waves must be present in the testing equipment.

1.3.5 Future Work

Experimental testing of HS steel foam sparked interest for where the next step would be for this innovative material. Between the time of this proposal and the defense, there are multiple directions upon where to be headed in. Finite element analysis has proven

to be valuable for the exploration of a material especially when more of it is not available for further experimental testing or the cost of producing results can be decreased by using FE analysis. One possible application with the results of these tests is to develop a fully functional material model in a finite element program such as ADINA. Next, this material model can be applied to a larger setting which for example, in this case, would be to have HS steel foam act as a material for a structural engineering application. As we know that it is a great material for absorbing energy, one possible application of an FE model would be to model a regular structural element, such as a beam or a column, and to surround the element with HS steel foam developed with the material model. Within this application, there are many analyses that can be used to move forward such as impact or blast simulation on this particular column. Further examination of such a model would look at the response of energy absorption by the HS foam as a function of energy absorption of the column it encloses, buckling capacity, cost analysis, among many others.

1.4 Finite Element Analysis

1.4.1 Introduction

The motivation for introducing finite element analysis is to further study the dynamic crushing of HS steel foam. Smith developed a finite element model and application for the microstructure for it but it was found that in order to simulate the dynamic crushing it would be more cost-effective to model the experiments at a macroscopic scale, and as a result, obtain a material model. In addition to Smith, Gaitanaros and Kyriakides were successful in modeling and analyzing the microstructure of aluminum open-cell foams under dynamic crushing behavior. It is the objective of this section to

develop a macroscopic material model based on the experimental results' mechanical properties. This model can later be adopted into a model whose purpose would be to look at how this material behaves when applied in a purely structural sense. ADINA 9.2.2 is the primary software for finite element analysis that is going to be used.

1.4.2 Modeling

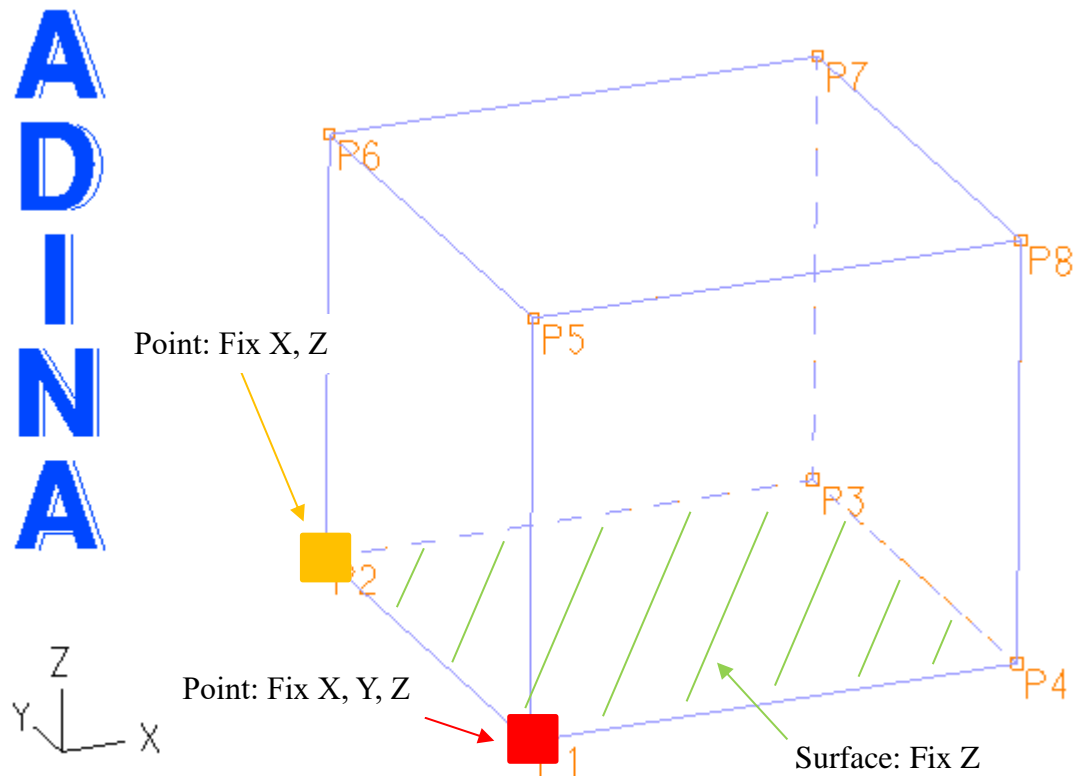


Figure 1.34: Boundary conditions for preliminary model

In order to begin the pre-processing of the FE modeling, many mechanical properties need to be acquired and in this case, they are found in an earlier Section 1.3.3

Results and Analysis. The first objective was to model the crushing experiment from the 928 mm drop height of sample 1. Therefore, geometry was obtained from the measured dimensions for this sample and given special dimensions. In a general sense, the

model was to be interpreted as an imperfect cube, therefore eight points for the HS steel foam sample were input to ADINA, defining the corners of the sample. Once the points were defined, the cube was to be constructed by defining the volume with using vertex types and the shape of a hexahedron. After the six faces formed and defined the volume, a study on boundary conditions was done. Defining the fixity for this system proved to be a challenge due to its multiple iterations of getting desirable and understandable results, especially with deformations. The finalized boundary conditions are displayed in Figure 1.34. This set of boundary conditions provides a stable system for which the loads can be applied to. P1 has all DOFs fixed and P2 has X and Z DOFs fixed, leaving the Y-DOF free so that when the foam is crushed it is able to expand in that direction. Finally, the bottom surface of the foam sample is fixed along the Z direction so as to allowing movement in both X and Y directions and restricting it in the vertical (Z) direction due to the fact that there is a solid surface under that which prevents the foam from crushing in that direction.

The next set of definitions involved the assignment of a material model to the cube for which the material properties were calculated for in Section 1.3.3 Results and Analysis. A tri-linear model was developed to approximate the behavior of Sample 928mm_01. Material definition first began by attempting to recreate Sample 1's stress-strain curve of Figure 1.20 as a bilinear elastic-plastic material with the following material properties:

- Young's modulus, $E = 569 \text{ MPa}$ (This is the average elastic modulus of 928mm drop height experiments)
- Poisson's ratio, $\nu = 0$

- Yield stress = 23.0 MPa (Assumed that second data point for Sample 1's stress-strain curve in Figure 1.20 corresponded to this test's yield stress)
- Mass density, $\rho = 1,163 \text{ kg/m}^3$ (Calculated value for this particular sample's weight and dimensions)
- Strain hardening modulus, $E_H = 29.4 \text{ MPa}$ (Calculated value of the slope between yield stress and ultimate stress)

Once the material was defined, the element group had to be defined and assigned to the cube. As the cube's geometry was defined as a volume, the element group's type was defined as a 3D solid with the corresponding material as the default. Next, to assign this element to the cube, a mesh was created. The volumetric mesh density was set with the method of *number of divisions* and a progression of element edge length as *geometric*. Having the number of subdivisions and length ratio of element edges set as 1 for all directions, U, V, and W meant that this was a coarse mesh, with the cube acting as a single mesh in itself. In order to apply the mesh to the cube, a volumetric mesh was created with 27 nodes per element, the maximum allowed by ADINA, and was an appropriate choice due to the coarse mesh density that was chosen to begin with. Having 27 nodes per element allowed for taking full advantage of the coarse mesh.

To model a specific experimental test, it has to be clear how the loads are going to be implemented and what the output is expected to be. In this case, the output has to be a stress-strain curve and the resulting stresses, therefore, must resemble those that were computed in the experimental test. Typically, forces are defined for loads upon a system but for this instance, the load type that was applied was a displacement upon the entire top surface (Surface 6) of the cube in the $-Z$ direction. Initial and final sample height

measurements were taken for every sample of every drop height, and it is that difference between those two that implies how much the sample had deformed by which got defined as a displacement load for the model. For Sample 928_01, this displacement was measured to be 11.37 mm using the FBF method and proportioning the values to the real geometry. After the displacement loading condition was defined, the time function was created for the load to be referenced to. Time function definition was based on the displacements measured taken by the FBF method, therefore a displacement-time function was created relative to the maximum deflection of 11.37 mm being equal to the magnitude of 1.0, and all of the previous displacement measurements being scaled to that value. Table 1.17 shows the incremental displacements that were measured and the scaled displacements that were input as a time function in ADINA, as seen in Figure 1.35: Scaled displacement-time function for Sample 928_01.

Table 1.17: Time function displacements for Sample 928_01

Time (sec)	Measured Displacement (mm)	Scaled Displacement (mm)
0.000000	0.00	0
0.000444	1.36	0.12
0.000666	2.27	0.2
0.000889	3.18	0.28
0.001111	4.09	0.36
0.001333	5.00	0.44
0.001777	6.37	0.56
0.002000	6.82	0.6
0.002222	7.73	0.68
0.002444	8.18	0.72
0.002666	8.64	0.76
0.003111	9.55	0.84
0.003333	10.00	0.88
0.003555	10.46	0.92

0.003777	10.69	0.94
0.004000	10.91	0.96
0.004444	11.37	1

Once the time function was defined, time steps needed to be added in order to discretize

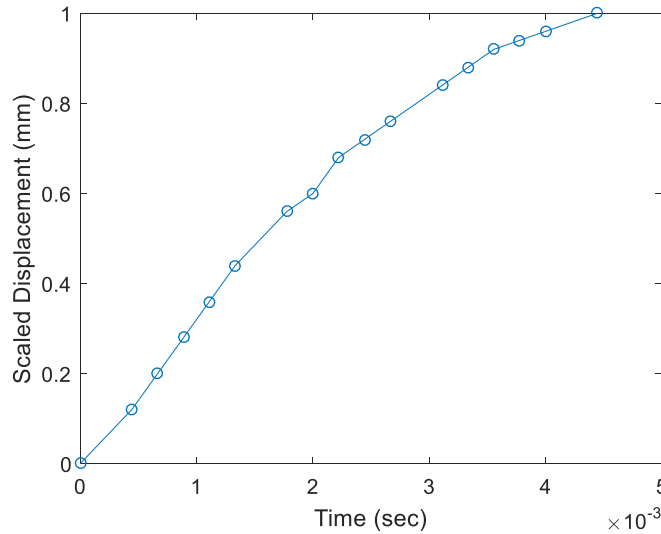


Figure 1.35: Scaled displacement-time function for Sample 928_01

the time function and fully capture the behavior induced by the load. A value smaller than the time duration between points was chosen and to capture the full 0.004444 sec time span and yielding region, two-time steps were defined as follows:

- 100 number of steps with a magnitude of 0.00001
- 100 number of steps with a magnitude of 0.000034

The preliminary model was established and was ready to be run as a dynamics-implicit analysis.

1.4.3 Dynamic Analysis

The purpose of the preliminary dynamics analysis is to set the foundation for a material model with the correct material properties that are in correlation to those that were measured. Applying a plastic-bilinear model in ADINA yielded relatively acceptable

results, with a close approximation to that of the behavior of the stress-strain curve posed

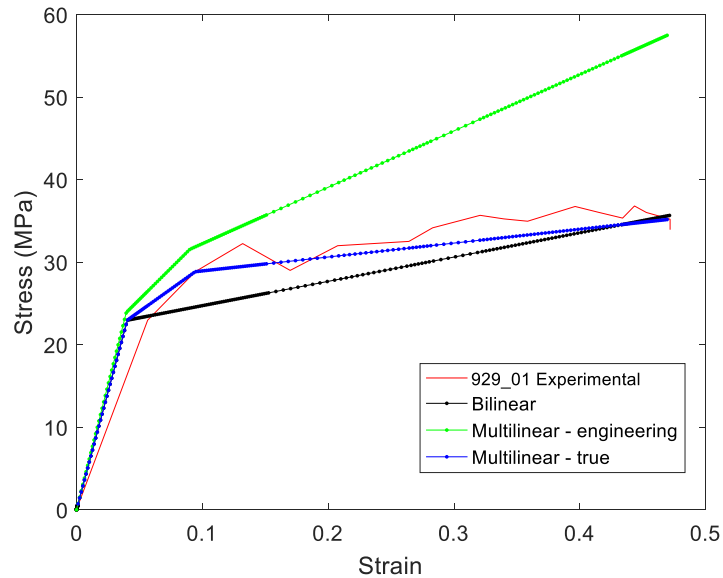


Figure 1.36: Development of stress-strain curve for 928_01

by the experimental results (shown in black in Figure 1.36: Development of stress-strain curve for 928_01). Next, to improve the model's stress-strain response, a multilinear elastic-plastic material was defined with the same characteristics of the bi-linear model's characteristics so as to take the next step towards a tri-linear model. Except, this time, ADINA requires a direct input of the stress-strain curve, so in addition to the previous model's characteristics of: Young's modulus, $E = 569 \text{ MPa}$, Poisson's ratio, $\nu = 0$, Mass density, $\rho = 1,163 \text{ kg/m}^3$, the stresses and the strains were defined as they were calculated for in Section

1.3.3.3 Stress vs. Strain. The three points that were included were the yield point, the next point after yield, and the ultimate stress point. Strain hardening was defined as an isotropic type by default and also by default, the stress-strain curve was interpreted as engineering. After running the same model with the multilinear material properties, a peculiar and questionable stress-strain curve was developed which shows that it increases after the yield point to a stress level that was nearly double than those that were defined (shown in green in Figure 1.36: Development of stress-strain curve for 928_01). Going back and revising the inputs of the materials, one subtle difference made all the difference when inputting the stresses and strains. After numerous trials and iterations, it was found that when inputting a multilinear material in ADINA, the stress-strain properties have to be modified to be read as *true* stresses and strains, as opposed to *engineering*. When the stress-strain curve is inputted for a multilinear material, ADINA has a dialog box for additional options, which was changed to “interpret material input data as true stress-strain data” since default is set to “interpret material input data as engineering stress-strain data” “This difference resulted in the multilinear material shown in blue in Figure 1.36: Development of stress-strain curve for 928_01 which resembles the experimental stress-strain curve better than the bilinear model.

1.4.4 Conclusions

Up to date, the model for Sample928_01 was found to be in a working order after resolving challenges related to boundary conditions, applied loadings, and material properties. It was found that in this case when defining a material with a multilinear elastic-plastic *engineering* stress-strain curve, the default in ADINA for interpreting it needs to be changed to interpret it as *true* stresses and strains. Leaving ADINA to interpret them as

engineering stresses and strains results in unwanted behavior of the model and therefore this corrected model is a good foundation for future modeling.

1.4.5 Future Work

Building upon the existing model will be a task involving new geometry dependent on what it is what the desired outcome should be. One possibility is to implement the material model to a structural application, such as a beam or a column. Here, the idealization for the foam model could get an entirely new geometry to encase the desired structural system with the material properties as defined. Another important property that should be considered in the future is the strain rate sensitivity. ADINA has two modes within defining a multilinear elastic-plastic material. In the Basic mode, the stress-strain curve gets defined as well as Young's modulus, Poisson's ratio, mass density, etc. The second mode that it offers is Strain Rate Effects. As this thesis' work is centered on the response under high strain rates, strain rates do have to be taken into account, observing the response, and comment on the differences of the preliminary model. In the dialog option, the only option available is to make the material "strain rate dependent" where there are multiple inputs that include: Strain Rate Fit Curve, Transition Strain Rate, and Strain Rate Hardening Parameter. These parameters constituted the next approach for using the developed material model into an even more accurate material model.

CHAPTER

2. THE DYNAMIC RESPONSE OF AN AMERICAN ELM TREE

2.1 Introduction

The American Elm Project surged from an interest of Dr. Kane's in which in collaboration with Dr. Arwade and me in which the intent was to structurally analyze an American elm tree located in Central Residential Area within the University of Massachusetts Amherst, as seen in Figure 2.1. The motivation for this project lies in the



Figure 2.1: American elm tree branch of interest located in Central Residential Area, UMass Amherst

background of this particular tree which was used for a tree climbing competition and so is frequently used by tree climbers. Upon an observation of a tree climber using an unconventional method to climb this tree, it led to the investigation of how different parameters and dynamic loads affect the structural response of the tree branch, and as a result, the safety of the tree climbers can be improved. To accomplish this objective, we

must accurately define and calculate the stresses that occur along this tree branch that gets subjected to dynamic loads induced by the climbers.

Two types of dynamic loads are of interest here. The first one is the impulse load, which is an idealization of a climber falling while ascending towards the branch, while secured with a safety rope that is attached to the branch, and thus inducing an impulse on the branch. The second one is the measured, cyclic load of a climber ascending a rope. Using both dynamic load scenarios gives us an idea of how the tree branch will respond structurally and mechanically. Climbers can use our results to understand the likelihood of branch failure when climbing, and choose an alternative method to improve safety.

2.2 Geometry

2.2.1 Experimental Data

The measurements of the primary branch with secondary branches were acquired from Dr. Kane, shown in Appendix A, and it showed measurements taken of the primary branch to be in 12 sections of 1m increments and the last section to be 0.5 m, each with a total diameter, a corresponding vertical angle from the main trunk, and an azimuth angle taken from North. In addition to global coordinates, the external geometry of the tree branch was measured by Dr. Kane, which includes the diameter of each 1m element, its width and depth, and an approximate bark thickness of each. Then, the thickness of the sapwood was assumed to be 35 mm from the literature and as a result, the heartwood diameter was calculated. These measurements are important to the calculation of various parameters including the moment of inertia, the modulus of elasticity, and cross-sectional area geometry for every section. Each section had spherical coordinates that were

converted to Cartesian using both MATLAB and an online tool (<http://keisan.casio.com/exec/system/1359534351>). During field measurements, a total of three secondary branches that were attached to the primary branch were noted. The first secondary branch was the distal remainder of the primary branch, the second branch is located adjacent to the distal branch, producing a bifurcation at the end of the primary branch, and the third secondary branch is located approximately at the midpoint of the primary branch. The presence of these secondary branches is important to the overall dynamic response of the system, but the field measurement of them was not feasible the same way that the primary branch allowed for. The three secondary branches were measured in the field by its start point (where they are attached to the primary branch) and its end point (where in space it protrudes out to), therefore an assumption was made that these two points were connected linearly. In reality, secondary branches were not perfectly straight, and this assumption approximates its presence as best as possible. Furthermore, the three secondary branches were sectioned in 1m increments the same way the primary branch was sectioned, in order to have continuity along the entire system for the finite element modeling. Since the geometry of the secondary branches was not feasible, the geometry of the secondary branches' length was conical and the cross sectional geometry was calculated using proportionality and linear interpolation.

The spherical measurements were performed sequentially, separated into 1m sections along the length of the primary branch. Therefore, through a series of calculations, it was possible to convert the spherical coordinates into Cartesian sequentially, thus generating the branch's geometry in space that was later imported into ADINA for finite element analysis. Another aspect of it that became a challenge was the division by sections

of the three secondary branches because their length was greater than 1m but had to be split into multiple sections that coordinates were not measured by sections, as it was for the primary branch. The measurements that were taken for the three secondary branches were: the full length of the branch of each of the three secondary branches was the only measurement taken for them, and the angle and the azimuth, both relative to the primary branch. To account for only a beginning and end point in space for the secondary branches, it was assumed that they did not change direction of course and therefore, the direction became uniform and it was only a matter of calculating where in space (by coordinates) each of the 1 m section would be if they were to be straight sections. In addition to this, the cross-sectional properties were calculated assuming a conic section for the secondary branches from beginning to end. This is an important assumption to be noted because it does not represent the branch wholly. Rather, the secondary branches are still modeled and idealized as such to give the model that extra mass that it needs to be able to be analyzed for torsional rigidity.

2.2.2 SketchUp Modeling

Once the Cartesian coordinates are obtained for the entire branch (including the primary branch and three secondary branches) they were input into the 3D modeling software, SketchUp for visualization purposes and to have as a reference especially when performing the finite element modeling. The Cartesian coordinates were organized in a table that was later imported into SketchUp using an extension that graphically maps the points in space entered in an x-y-z format. These points are essentially nodes that connect the 1m elements of the primary branch and secondary branches. After all 38 points were

imported into the workspace, which represent the branch's 1m-long sections, they needed to be connected by idealized cylinders to represent the branch composition. No point is alike and they are all in a particular area in space. To connect one point to the next by a cylinder, local axes had to be defined, but first, all of the points were connected by a single continuous line. The method of doing this involved drawing a circle at every one of the 38 points with the exact dimensions that represented the cross-sectional area for that particular section, as calculated. Therefore, once the points were connected by a line, an arbitrary shape was drawn to enable the use of the *Follow Me* tool, which allows for the tree branch to begin to take shape by extruding the 2D shape into a 3D ellipse/cylinder. This arbitrary shape was deleted except for the base of the shape, which is where the beginning of each 1 m section began. After this was done, and since all the points had different axial directions, the *Align Axes* tool was used to accurately draw the measured cross-sectional area for every section. Doing so, and then afterward applying the *Follow Me* tool once again, led the way for the final form of the tree branch. The last part included erasing any geometry that was no longer necessary and finally applying a wood flush to the exterior of the branch. Figure 2.2 shows the finalized model of the tree branch in SketchUp.

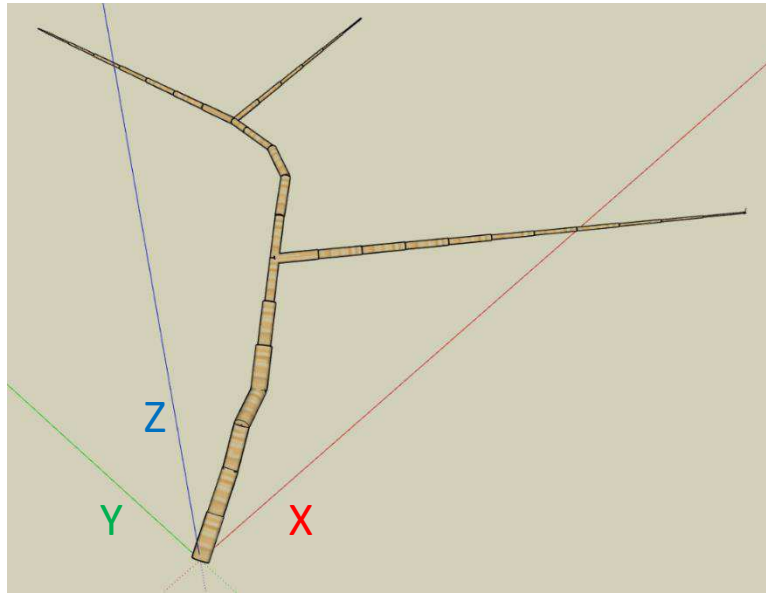


Figure 2.2: SketchUp model of the tree branch showing the scaled geometry for every section

2.3 Finite Element Analysis

2.3.1 Modeling

To be able to analyze this set of problems on a finite element analysis software, multiple mechanical properties need to be obtained and calculated. The necessary wood properties for the American elm were obtained from the *Wood Handbook* (Glass & Zelinka, 2010; Kretschmann, 2010). Density was calculated independently for heartwood and sapwood (bark contribution is negligible, therefore it was ignored) using Equation 4-12 (Glass & Zelinka, 2010) but it was found that the 1% difference in discrepancy was negligible between them, therefore to simplify the problem it was assumed that they both have a calculated density of $1,050 \text{ kg/m}^3$. It was found in Table 5-3a (Kretschmann, 2010) that the “green” modulus of elasticity of the American elm’s heartwood to be 7,700 MPa.

Per (Niklas, 1997), the modulus of elasticity of the sapwood is to be taken as 35% less than the heartwood's, or 5,005 MPa. These properties were the initial values that needed to be obtained to be able to input into ADINA.

The branch's structure consists of the heartwood in the center and the sapwood as a ring that surrounds it, with a thin layer of bark surrounding that. The bark's material properties are negligible for this set of calculations and the bark becomes only relevant for calculating the geometry of the heartwood and sapwood based on the measured total diameter of the branch sections. Since the branch consists of two different subtypes (heartwood and sapwood) with differing moduli of elasticity, an *effective* bending rigidity, EI , was initially calculated due to the individual moduli of elasticity, $(EI)_{\text{heartwood}}$ and $(EI)_{\text{sapwood}}$, that were taken into account. Upon careful consideration by all parties, it was decided that the best approach to approximating modulus of elasticity for this tree was to calculate it by structural means. The term "structural modulus of elasticity" was coined in (Rowe & Speck, 1997) as the modulus of elasticity that is obtained from the measured displacement induced by the weight of the tree climber. To do so, a new set of calculations was prepared in which cross-sectional sections are circular and without bark. This method also implies and assumes that the branch has a single modulus of elasticity that does not vary axially or radially. To get the structural modulus of elasticity, an iterative process was conducted by changing the model's modulus of elasticity until the desired deflection of 7.6 cm (3 in.) was obtained as seen in Section 2.3.4 Calibrating Young's Modulus. That structural modulus was 11,900 MPa. To put it in perspective, the initial modulus of elasticity computed from the "effective" properties calculations was nearly 6,400 MPa, so

an increase of a factor of almost 2; details for these calculations are explained in Section 2.3.4 Calibrating Young's Modulus.

After the geometry of the tree branch was obtained and some of the material properties as well, the finite element modeling was underway. ADINA 9.2.2 was used as the software for the FE modeling and the geometry was imported as Cartesian coordinates 1m in length away (for the most part) from each other, 38 total points were imported to create 38 nodes. Next, the nodes had to be connected to form the 1 m sections of the tree branch. From node to node, straight lines were drawn and began to take the shape of the intended tree branch.

After lines were defined (37 in total) between points, the material of the tree branch had to be defined. Wood is an orthotropic material but plasticity effects were beyond the scope of this projects and therefore the material was defined as isotropic, linear, and elastic because the interest is to focus on the material properties acting along all directions. One material was created with the following properties: Young's modulus of 11,900 MPa (this value is explained later how it was obtained), assumed Poisson's ratio of 0.3, mass density of 1050 kg/m³. After this was established, cross sections needed to be created and assigned to a section. There exist 37 sections that correspond to the lines that connect the 38 nodes. To create each section, multiple values were obtained through geometry and calculations. The total cross-sectional area, A_T , was calculated by adding the area of the sapwood and area of the heartwood for every particular section. The geometry for this varied throughout the length of the primary branch and as stated earlier, assumed to be conic and proportional for the three secondary branches (the primary branch consists of the first 12 sections on the model as shown in Figure 2.4 and is the primary interest). The thickness of the sapwood,

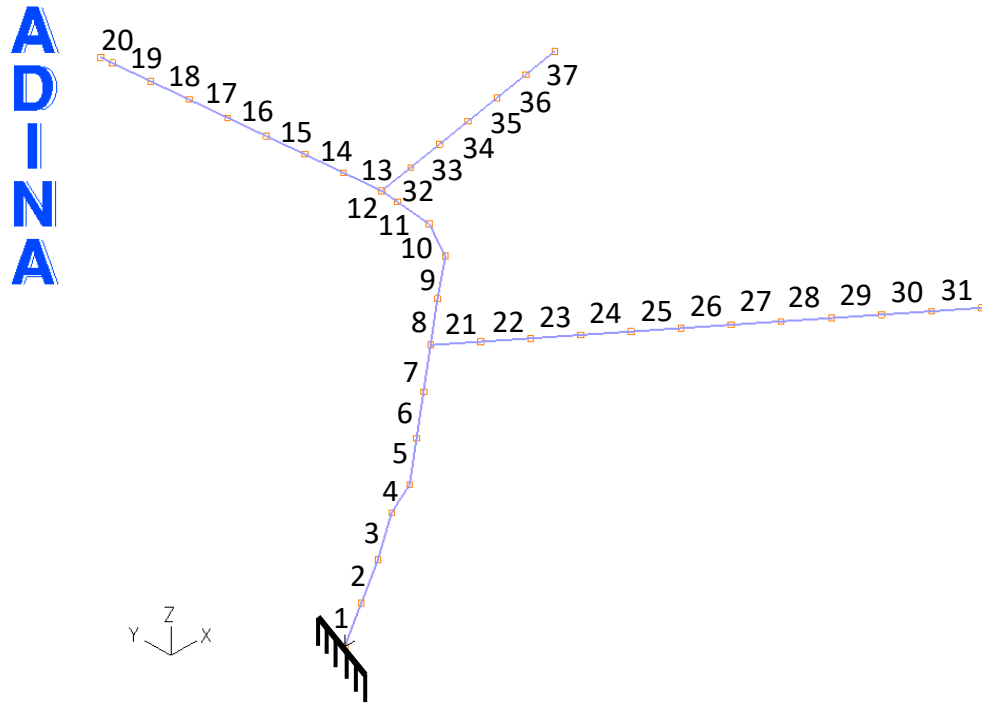


Figure 2.4: FE model of the tree branch with numbered elements

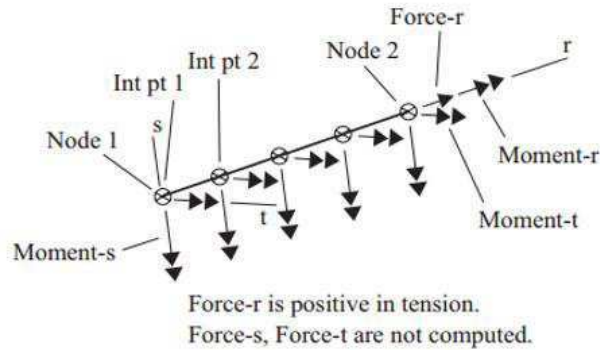


Figure 2.3: Stress resultant output option for the moment-curvature models

t_s , was measured to be 3.5 cm along the length of the primary branch (Niklas, 1997). The thickness of the bark decreases in 3 m increments: 1.25 cm for the first 3 m, 0.6 cm for the next 3 m, 0.4 cm for the next 3 m, and 0.2 cm for the final 2.5 m—unlike the other 11 sections, the 12th section is approximately 0.5 m long. These thicknesses are important because the geometric measurements of the cross-sectional area in the field include the bark. For cross-sectional area calculations, the bark's thickness is neglected, therefore the

cross-sectional area, A_T , is, after all, an idealized area without the bark. To define a general cross section in ADINA, other items that were needed to define the 37 distinct cross sections were area moment of inertia, I_T , and St. Venant's torsional constant, J . For the area moment of inertia, ADINA interprets three different inputs because of the three resultant directions, r , s , and t , as seen in Figure 2.3: Stress resultant output option for the moment-curvature models but since the interest of this work is that of axial and bending stresses, only those in the s - and t -directions are inputted: I_s and I_t . The last parameter that is input for defining the cross sections is St. Venant's torsional constant, J and is computed with Equation (2):

$$J = \frac{\pi}{2} \left(\frac{d_{heartwood}}{2} + t_{sapwood} \right)^4 \quad (2)$$

Once all of the parameters are calculated for every section of the branch, all 37 sections are created in ADINA with their corresponding parameter values.

Drawing the lines to connect every node was an important decision for as to what element group was going to be chosen as. Creating lines for sections and then applying the sections to the lines meant that the type of element for this project was going to be a 3D beam. Having one material defined: isotropic, linear, and elastic and 37 different cross sections then made it possible to define a beam element for every section. The mesh density that was used to begin with was defined as a node-to-node mesh with only one subdivision, and it was later found that this model was not mesh dependent and therefore this type of mesh applied to all of the lines and sections. To create the meshed lines, it was defined for every element group (37 in total) to have 2 nodes per element with a vector orientation in

the skewed vector system and directionality of $X = Y = Z = 1$ and applied to all lines. It was found in a study that the vector orientation did not change the overall results of the magnitude of the stresses therefore that directionality later became unchanged. After all, lines were meshed to represent the defined cross sections the boundary conditions were applied to make a stable structural system. All degrees of freedom were fixed at node 1 as seen in Figure 2.4 to simulate an attachment to the main tree trunk and to make it stable as well. All in all, the tree branch basically acts as a cantilever so various checks along the way with regards to beam deflection. The final part of the FE model is the loads that were applied. A mass-proportional load (self-weight) was applied at all times to the entire model with a magnitude equal to 1 and acting in the $-Z$ direction. When running a self-weight analysis only, either static or dynamic, no more additional loads were applied. Usually though, a self-weight analysis was not always needed and therefore the magnitude of the other load that was applied depended on what type of analysis was going to be run. It was always a point load of a magnitude of 1 and acting in the $-Z$ direction placed on Node 13 which was the node of interest for displacement and that was the node of reference for the climber being attached to that point along the branch. This point load varied in magnitude because of the time function that was occurring for different analyses, and these are explained in the following sections.

2.3.2 Modeling Assumptions

Along the way of any finite element model assumptions were made, and in this case, it is important that they are explicitly described after having the full model being described in the previous section. The first one is the development of the definition for the

modulus of elasticity. As explained earlier, an effective modulus of elasticity was calculated initially based on the composition of the tree's heartwood and sapwood material properties. Effective modulus of elasticity, E (6353 MPa), was calculated by essentially averaging the individual moduli - summing the moduli of elasticity of the heartwood and sapwood and dividing by 2 and it is assumed that this remains constant throughout the entire tree branch and secondary branches. $E_{\text{heartwood}} = 7,700$ MPa (Kretschmann, 2010); $E_{\text{sapwood}} = 5,005$ MPa [$E_{\text{heartwood}}$ taken from Table 5-3a in (Kretschmann, 2010), and E_{sapwood} is assumed to be 35% less than that of $E_{\text{heartwood}}$ (Niklas, 1997)]. This does not perfectly represent the composition of the tree because the geometry of the heartwood varies along the length, while the geometry of the sapwood remains constant along the length of the primary branch. For the purposes of the model of the branch, it was agreed that this was a good approximation and assumption because it sufficiently simplified the model, enabling to define only one material throughout the entire model. All in all, this method was later discarded and the structural modulus of elasticity was calculated as 11,900 MPa, explained later. In addition, this further neglected the initial calculations of an effective axial rigidity (EA), effective moment of inertia (EI), and an effective torsional rigidity (GJ).

Mass density, ρ (1,050 kg/m³), is assumed to be uniform throughout the length of the branch and the secondary branches and was calculated in accordance to Equation 4-12 from (Glass & Zelinka, 2010). Initially, density was calculated independently for heartwood and sapwood (bark contribution is negligible, therefore it was ignored) but it was found that the discrepancy was negligible between them (1% difference), therefore to simplify the problem it was assumed that they both have a calculated density of 1,050 kg/m³.

Perhaps one of the biggest assumptions includes the secondary branches idealized as cones. As they are given a starting diameter from that section's geometry and a final point in space. In addition to conic, they are perfectly straight. This assumption is present in order to factor in the weight of said branches, regardless of the shape. Another assumption with secondary branches: the thickness of the sapwood is also conic, therefore it reduces as it follows the length of the secondary branch proportionately (opposed to the primary branch, where the thickness of sapwood is constant at 3.5 cm). The thickness of heartwood also follows the conic geometry the same way. Another important geometric assumption was that the field measurements that Dr. Kane obtained from the tree branch are without self-weight. In other words, the tree branch is already under its own self-weight when the measurements are being taken and we cannot explicitly measure it without self-weight. Therefore, it was important that one of the first static analyses was to see how much the tree is already deflected by if we are to assume that there is no external load acting on it.

2.3.3 Modal Analysis

One of the preliminary analyses conducted is the modal frequency analysis, which enables us to study the branch's dynamic response and its properties due to a vibrational excitation. As shown in Figure 2.5: First and second modes of the tree branch, the results show that the first two modes of the branch are behaving close to what we expect. The

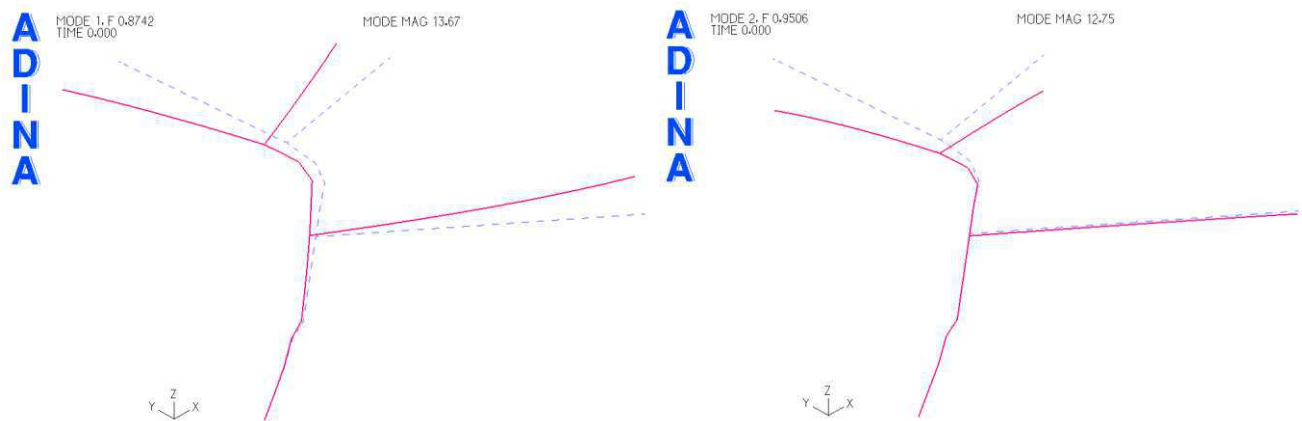


Figure 2.5: First and second modes of the tree branch

modes after the first two modes were undesirable: the majority of the dynamics went to the secondary branches, which were not measured in as much detail. The dotted blue is the undeformed shape and the red in the first mode and displays a frequency of 0.87 Hz and vibrates horizontally, whereas the second mode displays a frequency of 0.95 Hz while vibrating vertically. In theory, this is a good indication that the branch is dynamically behaving in the way we expect it to due to the frequencies that even though are relatively fast values, they are close in value to one another. In the following modes, modes 3 and up, the frequency is at 1.34 Hz and greater but the most prominent motion starts to move out to the secondary branches. The mode frequencies become important when performing damped dynamic analyses which will be detailed later and for defining time steps for the time functions.

2.3.4 Calibrating Young's Modulus

Earlier, it was explained how the research team explored options to obtain a modulus of elasticity, in which the consensus resulted in calculating for a “structural modulus of elasticity”. The objective for the calibration of the modulus was to obtain the modulus value that yielded the measured displacement induced by the weight of a tree climber, without self-weight (explained in Section 2.3.5 Static Analysis why it was neglected for this calibration). On the tree itself, Dr. Kane measured 7.6 cm as the vertical displacement at the point of interest that was induced by solely his weight of 77 kg (and, of course, inherently the real self-weight of the tree branch). An iterative process began by running a set of static analyses, where the variable input was the modulus of elasticity, E, and the desired output was deflection under only self-weight and deflection under self-weight + point load of 756 N (77 kg). Table 2.1 shows the iterative process for which the final values converged.

Table 2.1: Iterative process for calibrating Young's modulus

Structural MOE, E (MPa)	Self-weight + climber deflection (cm)	Self-weight deflection (cm)	Difference, δ (cm)
7,700	15.7	4.0	11.7
13,200	9.2	2.3	6.9
12,000	10.0	2.6	7.4
11,900	10.2	2.6	7.6

The final result was that the self-weight resulted in a deflection of 2.6 cm and the self-weight + point load of 756 N (77 kg) resulted in a deflection of 10.2 cm. By subtracting one from the other, our objective of 7.6 cm is reached of only the climber's weight being induced upon the tree branch. It is with this deflection that the input E was to be used for

the remainder of this work, 11,900 MPa. In this study, beam deflection comes into play because it is clear from the iterative calculations and analyses that it closely resembles the direct proportionality between deflection, δ_{max} , and elastic modulus, E, as a result of the maximum deflection of a cantilever from a point load, as shown in Equation (3):

$$\delta_{max} = \frac{PL^3}{3EI} \quad (3)$$

2.3.5 Static Analysis

The first part of the static analysis that was accomplished was the self-weight static analysis, the objective of which was to give an idea of how much the tree deflected at the point of interest, Node 13, and by how much it should be theoretically propped up by, if needed. Under the tree branch's self-weight, the vertical deflection was 2.6 cm at Node 13. It should be noted that the original branch geometry in space is not necessarily the perfect depiction of what it is in reality. The final, real, geometric measurements obtained by Dr. Kane of the branch are technically the geometric measurements of the branch already in its final state under its self-weight. After modeling the branch in accordance with this geometry, we added its self-weight to the "already deformed" geometry in reality, which we are taking to be in its original state in the ADINA model. A possibility for future work with this would involve that if we find that this correction needs to be done, the approach would be to obtain the X, Y, and Z-coordinates of every node after the self-weight analysis is conducted in order to "subtract" from the original coordinates and locate the branch to its un-deformed, unloaded state as a function of its self-weight. Since the deflection at the point of interest is 2.6 cm, we assumed that it is a small enough value to carry on with the study without needing to modify the original geometry to its "undeformed" state without

any gravity acting on it, and this mass density value is adjustable throughout the entire system. The self-weight load was input into ADINA as a mass proportional load with a magnitude of 1 and acting in the $-Z$ direction. Likewise, the second part of the static analysis involved adding climber's weight of 77 kg, input as a 756 N point load on Node 13 acting in the $-Z$ direction as well. Because of its static analysis nature, a single time function was defined and set as 0 to 1.0 pseudoseconds with a value of 1.0 to 1.0 in magnitude. Both loads referred to that time function and so the time step was simply set at only one step with a magnitude of 1.0 and it was found later that increasing the number of steps did not have an impact on the final result which was the maximum deflection of Node 13. In conclusion, the static analysis served as a tool to calibrate Young's modulus to $E = 11,900$ MPa and to debug the model and make it functional, and Figure 2.6: Static analysis with labeled points.

In accordance with the objective, maximum stresses were calculated along the

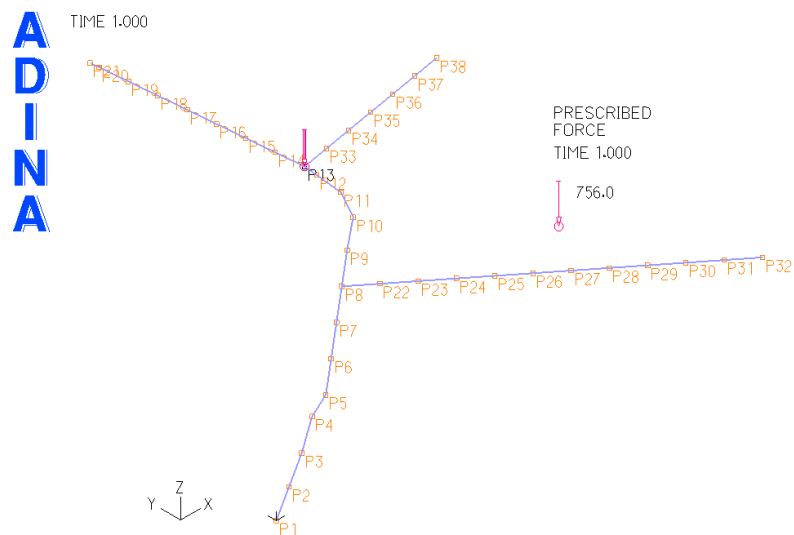


Figure 2.6: Static analysis with labeled points

primary branch modeled as 12 sections as seen in

Table 2.2. A color scale is used to proportionally represent the maximum (in red) and minimum (in green) stresses and where along the primary branch they occur. Stresses were calculated by summing axial and bending stresses at every i^{th} node for every section. Bending and axial stresses were calculated as follows, from Equations (4) and (5):

$$\sigma_{bending} = \frac{My}{I} \quad (4)$$

$$\sigma_{axial} = \frac{P}{A} \quad (5)$$

Table 2.2: Sum of stresses for the self-weight static analysis

Element Group within Primary Branch	Combined Bending and Axial Stresses (MPa)
1	1.03
2	1.11
3	1.00
4	0.71
5	0.45
6	0.67
7	1.32
8	1.00
9	0.61
10	0.56
11	0.83
12	0.51

The results of this analysis show that the maximum stresses occur at the 7th 1m-long section along the primary branch, more specifically on Node 7. The minimum stresses occur in the 5th section.

Table 2.2 serves as a baseline for comparison with subsequent analyses.

2.3.6 Dynamic Analyses

2.3.6.1 Impulse Load

2.3.6.1.1 Introduction and Definitions

In this section, a large set of impulse scenarios on the tree branch are analyzed individually using a MATLAB function. This function calculates the force and displacement for a single degree of freedom system consisting of a free falling mass attached to a spring. This structural system is idealized as the simulation of a tree climber attached to the primary branch at the point of interest, Node 13 (Point 13 on Figure 2.6: Static analysis with labeled points), then falling and being caught by the rope, thus inducing bending and axial stresses along the length of the primary branch through the action of the climber's rope on the tree branch. As stated, the dynamic calculations involved idealizing the climber and the rope as a typical free falling mass-spring system and therefore the force solution is shown in Equation (6):

$$f(t) = kx(t) + mg \quad (6)$$

while $x(t) > 0$

and the displacement solution is shown in Equation (7):

$$x(t) = x(0) \cos \omega_n t + \frac{\dot{x}(0)}{\omega_n} \sin \omega_n t \quad (7)$$

In order to continue to define the problem and identify its set of varying and constant parameters, the function is illustrated as: `function [time, force, disp] = falling_load(m, l_rope, x_fall, strain_10_mbs, mbs, g, t_final, dt)` and the full code that

executes this mass-spring system behavior is included in Appendix B. In this function, the following parameters are constant throughout all the scenarios:

- Rope anchoring technique = single rope anchored to the branch (as opposed to doubly anchored)
- m_{bs} (Minimum rope breaking strength) = 6,500 lbs (28,913 N). This was chosen to be this value as it is a value for which common climbing ropes exhibit.
- g (Gravitational acceleration) = 9.81 m/s^2
- t_{final} (Final time at which the calculation ends) = 2 sec
- dt (Time step for load calculation) = 0.005 sec

The rest of the parameters all vary and it is with these variations that a total of 100 combinations/scenarios were created to identify which parameters, if any, have the greatest effect on the tree branch; and this is possible to observe by calculating the stresses along the branch for each scenario. These parameters are shown in Table 2.3 and using a scenario for every combination yields a total of 100 different impulse load scenarios as shown in Appendix C.

Table 2.3: Input parameters

Parameter	Values in SI units (English units in parentheses)		Description
m	81.65 kg (180 lbs)	99.8 kg (220 lbs)	mass of the climber

l_rop	1.52 m (5 ft)	3.05 m (10 ft)	6.1 m (20 ft)	9.14 m (30 ft)	12.19 m (40 ft)	rope length
x_fall	0.99 m (39 in)	1.32 m (52 in)				fall distance
strain_10_mbs	1%	2%	3%	4%	5%	percentage strain at 10% of rope MBS

2.3.6.1.2 Results and Analysis

Due to the elaborate nature of this analysis, it makes sense to describe and show only one scenario and understand that the remaining 99 analyses follow the same steps and execution. The scenario that is of interest will be the first one, titled “impulse_1”, and has the following characteristics (English units in parentheses):

- Climber mass = 81.65 kg (180 lbs)
- Length of rope = 1.52 m (5 ft)
- Fall distance = 0.99 m (39 in.)
- Percent strain at 10% MBS = 1%

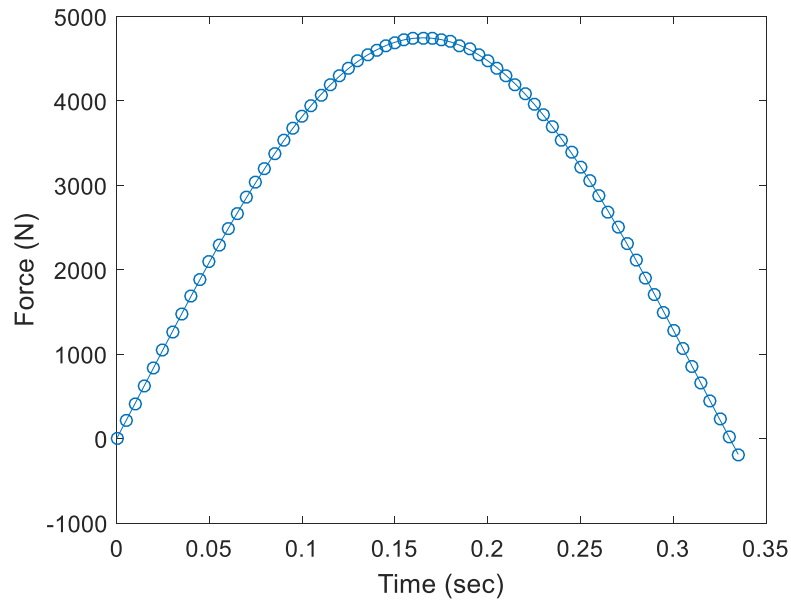


Figure 2.7: Impulse force function for the characteristics as described

Scenario 1 exhibits the force-time imposed on Node 13 as shown in Figure 2.7: Impulse force function for the characteristics as described, which was obtained using the MATLAB code from Appendix B. After force-time curves were obtained for every scenario, they were individually imported into ADINA as an impulse load on Node 13. All of the functions were discretized into the same number of time steps, 1000, at 0.005 magnitude, resulting in a total analysis time of 5 seconds. Figure 2.7: Impulse force function for the characteristics as described shows only the initial impulse of the load of approximately 0.34 seconds. It was decided that because the initial curve was the most important part of the load, it was not necessary to model the rest of the load. This first curve simulates the point of when the climber falls, the rope catches the climber, and here is where the curve begins. Once the rope catches the climber, it elongates and therefore the force induced by the climber gets transferred to the branch via the rope and is a function of its MBS, its

length, the distance of the fall, and the mass of the climber. The load reaches a maximum value of approximately 4,800 N when the rope is fully stretched and therefore transfers the most load to the branch, and then returns back to “zero” when the rope is no longer stretched. Subsequent impulse loads are smaller and it is unnecessary to model them. In addition to the impulse load, the mass proportionality load also was accounted for. In the initial stages of the analyses it was superimposed along with the impulse load but this methodology was later dismissed because it produced an undesired dynamic response from the tree branch. As a result, the mass proportionality load was run independently and its output of forces readings of the branch were extracted from ADINA. Because it was a static analysis and the same throughout all of the scenarios, this only needed to be done once and therefore, the impulse load scenarios were run independent of it. Running a dynamics-implicit analysis resulted in an oscillating tree branch whose displacement-time response oscillated below 0, as expected. To confirm that the impulse loads were being interpreted correctly by ADINA, a study was done in which a delay of 2 seconds was applied to the impulse load function. The analysis was run and the displacement-time response was as expected, in which the function was unchanged for the first 2 seconds, and after 2 seconds the impulse load kicked in and a much larger deflection was visible. Therefore, this confirmed that ADINA was interpreting the loads as desired.

In all of the finite element models, damping was taken into consideration and was estimated to be $\xi = 5\%$ due to the measurement of a similar tree in proximity to this one. Before this was defined, a study was carried out to determine how much significance damping had on the system. The results for Scenario 1 indicated that for $\xi = 5\%$, the maximum deflection on Node 13 resulted in $\delta = 40$ cm, and for $\xi = 1\%$, the maximum

deflection was at 47 cm, thus a 7 cm difference did not have many implications on the rest of the model and for the remainder of the project and scenarios the damping was defined as $\xi = 5\%$.

Table 2.4: Combined of bending and axial stresses and percentage within limit stress for impulse load “Scenario #1” in each element of the primary branch

Element Group within Primary Branch	Combined Bending and Axial Stresses (MPa)	Percentage within Limit Stress (%)
1	10.4	27.6%
2	12.1	32.2%
3	12.0	32.1%
4	8.7	23.1%
5	6.7	17.8%
6	11.0	29.3%
7	23.6	62.8%
8	22.2	59.1%
9	14.0	37.2%
10	14.3	38.0%
11	21.3	56.8%
12	14.1	37.6%

After the pre-processing of the model was completed and the analysis was run, the results are shown in Table 2.4, with the forces being extracted in the post-processing phase and stresses calculated from those forces by using the geometry and properties in Appendix A. Interestingly, with the application of an impulse load on Node 13, the maximum and minimum stress locations are unchanged from where they occurred in the self-weight analysis. Percent within the limit stress of rupture is included in this table to illustrate the relative percentage that each particular element of the primary branch is within the limit stress of rupture, 37.5 MPa [25% reduction from the modulus of rupture value, 50 MPa, for the American elm from the *Wood Handbook* (Glass & Zelinka, 2010; Kretschmann,

2010)]. This is explained more thoroughly in Section 2.4 Conclusions. It increases from the fixed end of the primary branch to the end where the load is applied, as one might expect from a cantilever with a point load at its free end. Because this is a dynamic analysis, extracting the maximum axial and bending moments was not as straightforward as was the static analysis. To obtain the maximum stresses, the force output from ADINA must be extracted and separated by element. For every element, the desired output included the axial force (NODAL FORCE-R) and the moment forces (NODAL MOMENT-S and NODAL MOMENT-T); and for every one of these listed, their values for every time step must be noted as well. The objective was to calculate the magnitude of the sum of stresses based on the set of forces, for every time step, for every element. MATLAB functions and loops were used to convert the output .txt files (from ADINA) into workable cell arrays. Once this was completed, the cell arrays were imported into Excel either manually or with a MATLAB code where in the final Excel sheet formulas were set up for every scenario to calculate for the maximum stresses for every element and to observe the time step they

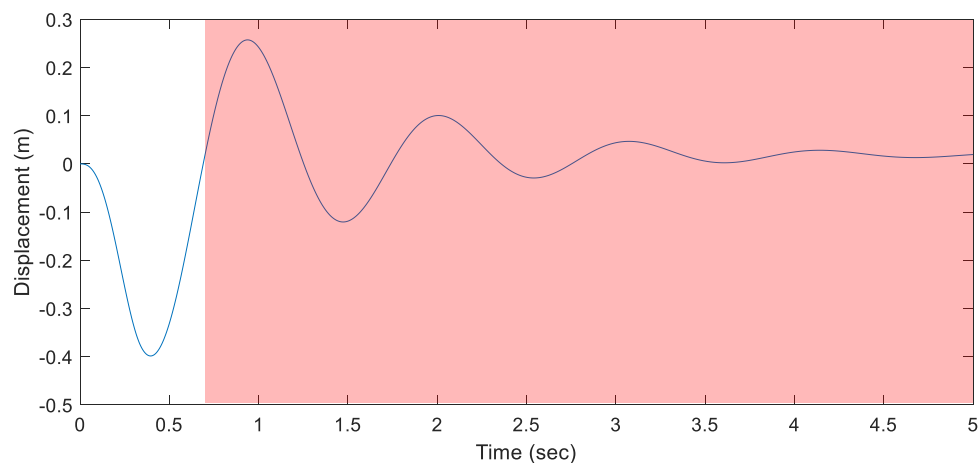


Figure 2.8: Displacement-time response for impulse load: Scenario #1

occurred at. For Scenario 1, the stresses calculated in Table 2.4 occurred approximately at

time step = 0.34 sec, which as seen in Figure 2.8: Displacement-time response for impulse load: Scenario #1, is where the maximum displacement of 40 cm occurs for the impulse load. After the displacement-time curve reaches 0 again on Figure 2.8: Displacement-time response for impulse load: Scenario #1 the rest of the response is non-physical because only the initial impulse was modeled, therefore the displacement cannot be positive, and this is denoted on the plot in a transparent red color.

After confirming that the model for Scenario 1 was behaving correctly, the rest of the analyses for every scenario were conducted and the maximum stresses at every element of the primary branch were calculated, in the same way as Table 2.4. Locations of maximum (Element 7) and minimum (Element 5) stress remained unchanged for all scenarios. This was somewhat expected because the overall location of the impulse load never changed, it was always set at Node 13, what changed was the magnitude of said impulse load due to the alteration of parameters from Table 2.3. Therefore, this allowed for a final comparison of one maximum stress between all 100 scenarios that occurred at the same location among all of them, at Element 7. Appendix C shows exactly that, where it shows the scenarios organized from greatest stress (in red) to least stress (in green) and

the parameters that went into that particular scenario. This shows that “impulse_78” exhibited the most stress for all scenarios with 32.35 MPa with the variable parameters of: 99.8 kg climber mass (greatest), 6.1 m rope length (middle), 1.32 m fall distance (greatest),

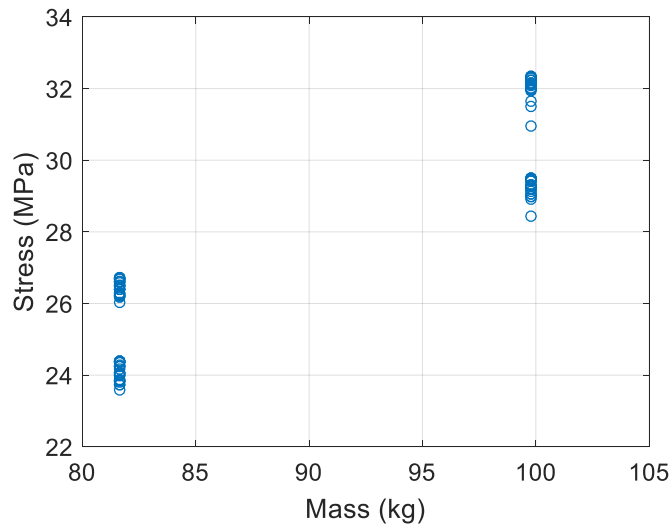


Figure 2.9: Stress vs. mass of all scenarios

and 3% strain at 10% of rope MBS (middle). To compare these results globally, the following graphs are presented to show the effect that every parameter has on the stress on the primary branch, by plotting the maximum stress results of these parameters for every scenario as a function of each parameter individually, shown in Figure 2.9 thru Figure 2.12.

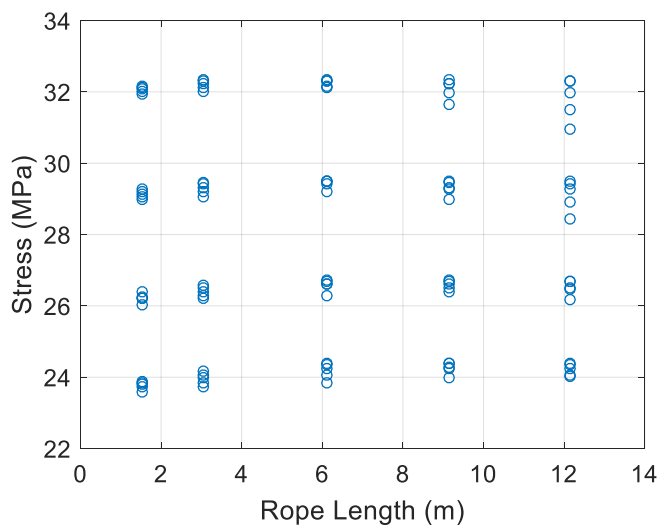
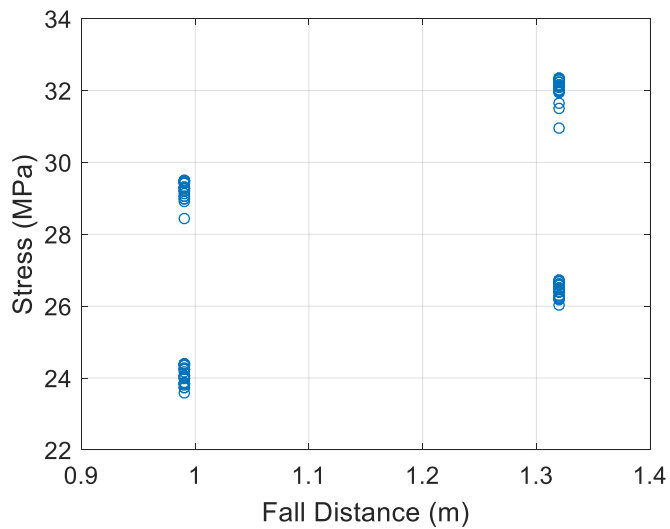


Figure 2.10: Stress vs. rope length of all scenarios



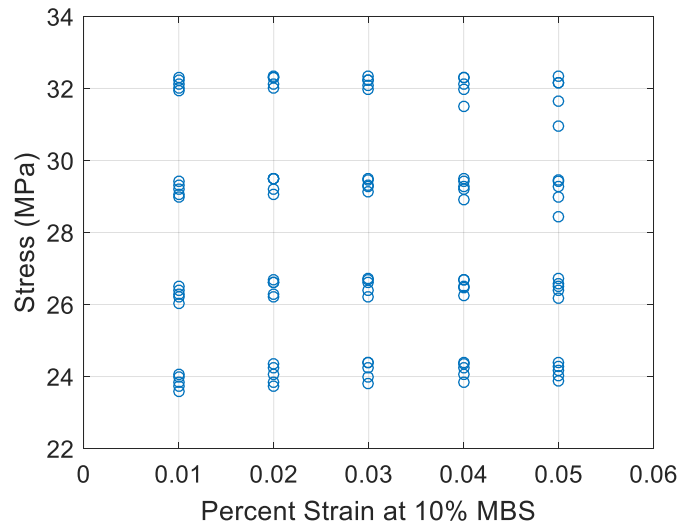


Figure 2.12: Stress vs. percent strain at 10% MBS of all scenarios

2.3.6.2 Climbing Load

2.3.6.2.1 Introduction and Definitions

The second dynamic analysis that was performed was the simulation of eight climbing loads that were measured by Prof. Reiland. Here, the idealization of the model is that of a climber routinely ascending the tree and thus inducing cyclic loads on the tree. Two methods of ascent were considered: DdRT and SRT. DdRT (Doubled Rope Technique) is a climbing technique in which a climbing line is doubled over a branch union, and both legs of the line hang parallel and unobstructed to the ground. SRT (Single Rope Technique) is another climbing technique where a single rope is placed through a suitable branch union, and one leg hangs where it can be used by the climber to access the tree. The second leg of the line may run to the ground over any number of branches and may be secured to the ground by a number of means, or the line may be secured in the canopy at

the branch union (Adams, 2007). It is hypothesized that using the SRT method of climbing given the location of anchorage will induce greater forces upon the tree branch due to only there being a single rope to carry the load, where in the DdRT method the rope doubles the amount of rope for the forces to travel through. In addition, this is evident in Figure 2.14 and Figure 2.13.

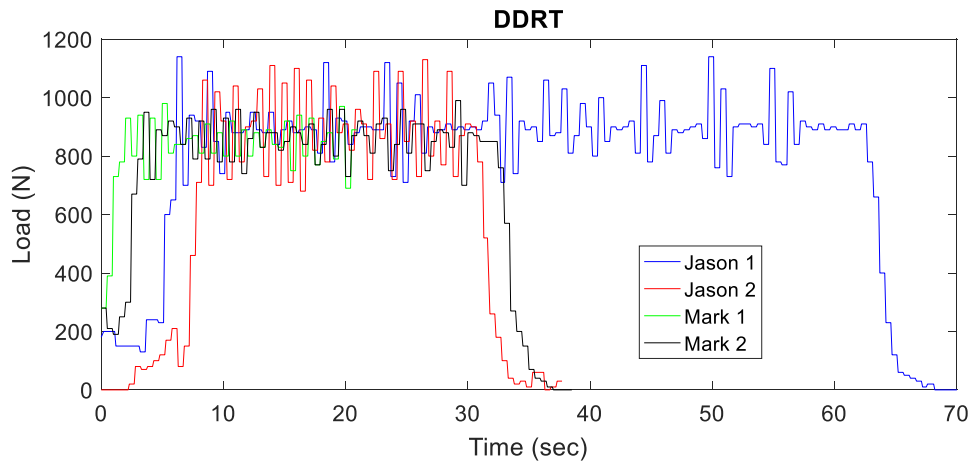


Figure 2.13: DdRT ascending loads

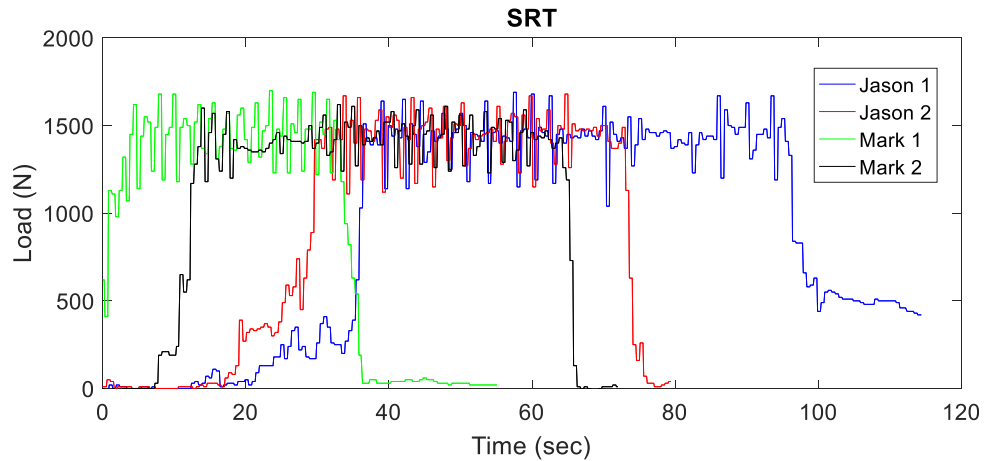


Figure 2.14: SRT ascending loads

The ascending loads were measured and are shown in Figure 2.14 and Figure 2.13. To begin with, the same way that the impulse loads were described and presented, one analysis is presented here as a reference, here the DdRT ascending load of “Jason 1” is

chosen and the first step was to input the time history into ADINA. Because the load is already given from field measurements, the ADINA model consisted of two independent time functions, one for the mass-proportional and one for the ascending load, similarly to the impulse scenarios. The mass-proportional (self-weight) analysis remained unchanged and the ascending load time history was changed for every one of the 8 total scenarios, 4 of which were for DdRT and 4 were for SRT. In the presented example scenario of DdRT-Jason 1 the total time spanned a total of 70 sec and the time step was broken up into 1,400 steps of a magnitude of 0.05 sec. This time step fully captured the behavior of the load due to the load measurements being taken every 0.1 sec, therefore dividing it in half for time steps was adequate and sufficient for the FE model throughout the remainder of the ascending load analyses. Like the impulse load analysis, the variations of this type of scenario resulted in different time functions for each one of the ascending scenarios from both types of climbing techniques, and calculating maximum stresses. For consistency, damping was applied as $\xi = 5\%$.

2.3.6.2.2 Results and Analyses

Table 2.5: Sum of stresses for DdRT load: Jason 1

Element Group within Primary Branch	Combined Bending and Axial Stresses (MPa)	Percentage within Limit Stress (%)
1	4.3	11.4%
2	5.0	13.2%
3	4.9	13.0%
4	3.6	9.6%
5	2.7	7.2%
6	4.4	11.8%
7	9.6	25.5%

8	9.0	23.9%
9	5.6	15.0%
10	6.1	16.2%
11	7.6	20.2%
12	3.6	9.7%

As an example, the maximum stresses for DdRT: Jason 1 are shown in Table 2.5 and were calculated the same way that they were calculated for in Section 2.3.5 Static Analysis, where it is described. Again, the results show that the location of maximum and minimum stresses is the same as the self-weight static analysis, and percent within the limit stress is also shown. This particular behavior could be attributed to that it is a cyclic load as opposed to an impulse load, therefore the increase in stress fluctuates. The displacement-time response is shown in Figure 2.15: Displacement-time response for DdRT: Jason 1 and it is important to note again that the maximum stresses that were calculated for in Table 2.5 correspond to their occurrence at an approximate time step = 6.667 sec, which is where

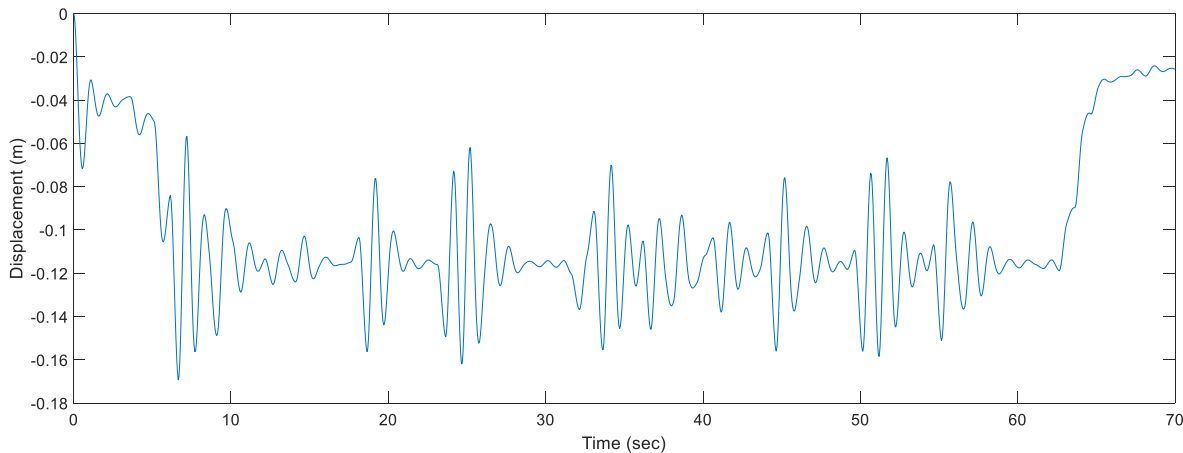


Figure 2.15: Displacement-time response for DdRT: Jason 1
the maximum displacement occurs for this load scenario.

After the model for DdRT: Jason 1 was confirmed that it worked as desired, the rest of the 7 scenarios were applied and their results are seen in Appendix C. It can be

deduced from these tables that as initially estimated, the primary branch undergoes greater forces and thus greater stresses under the SRT method. Some key results of the climbing load scenarios are that the maximum stress it undergoes is under that of the scenario SRT: Jason 2 where it underwent 12.74 MPa and that the location of the maximum stress is at Element 7 for all of them.

2.4 Conclusions

Different types of dynamic loads were applied onto the primary branch of a model of an American elm tree to study its response and ultimately translate that to improving the safety of tree climbers. This study observed this response under two main categories: an impulse load and a climbing load. There was a total of 100 scenarios of impulse loads that were analyzed and the critical scenario resulted in maximum stress of 32.35 MPa (within 86% of the limit stress) on Element 7 of the primary branch, and this location was constant throughout all types of scenarios. One reason for this lies in the idealization of the secondary branches and their location. The largest secondary branch connects at the endpoint of Element 7, thus inducing a large amount of weight onto that part of the primary branch and so this combined with the point load could result in the maximum stress being in that particular location. The graphical parametric analysis yielded in Figure 2.9 thru Figure 2.12 and showed that that the parameters that affected the stress the most were mass and fall distance, as initially hypothesized. This is seen by comparing the stress distribution within each parameter. For the rope length and % strain parameters on Figure 2.10 thru Figure 2.12, the stress visually remains constant for all of the different values assigned for the parameters, whereas in Figure 2.9 thru Figure 2.11, the stress distribution visually

increases as the parameters are changed. Furthermore, this is seen in a tabular format in Appendix C. The other type of load that was applied was the ascending load and 8 total scenarios were analyzed and the critical scenario resulted in a maximum stress of 12.74 MPa also on Element 7 of the primary branch. These values must be taken into a practical context and so we must compare these values to the modulus of rupture (MOR) of the branch of an American elm tree. This MOR value is listed on Table 5-3a as 50 MPa by (Kretschmann, 2010) as a relatively conservative value for which is obtained in laboratory measurements conducted on small, defect-free environments and specimens of wood. In actuality, this value does not accurately represent a good model for comparison to the calculated stresses from this chapter. Therefore, experimental data (Kane, 2014; Kane & Clouston, 2008) concluded that a better approximation to this new MOR value to compare it to should be a reduction in approximately 25% from the (Kretschmann, 2010) 50 MPa value and Table 2.6 shows exactly that.

Table 2.6: Strength properties of the American elm

Common Species Name	Moisture content	Specific gravity	Modulus of Rupture (MPa)	<u>Reduced</u> Modulus of Rupture (MPa)
Elm - American	Green	0.46	50	37.5

As shown, the reduced MOR value is 37.5 MPa and is the allowable limit for the maximum combined bending and axial stress it can withstand before rupturing. While the maximum ascending load comes to about 34% of the limit stress, the maximum impulse load comes within 86% of the limit stress. Therefore, for this particular case it is safe but an increase in either mass or fall distance can surpass the limit stress and the necessary

precautions would need to be taken prior to the ascension event in order to have the climber be out of harm's way and a potential rupture of the tree branch.

2.5 Future Work

Further investigation of this work can involve continuing changing parameters within the impulse load scenario to refine the model and get an even more critical/maximum stress. Another possible investigation could also involve comparing the dynamic behavior of an impulse load with a double-rigged rope system as opposed to the single-rigged from this study. Continuing with this study, the discussion of reduction in strength was a possibility in that in reality the tree could exhibit a loss of load-bearing capacity due to decayed wood or other structural defects like cracks or weakly-attached branches. This could be applied to the location of the maximum stress and detailed modeling would have to be implemented and careful assumptions would need to be made like having a hollowed-out section in order to simulate the real as best as possible. Fundamentally, this specific case would reduce the area moment of inertia and as a result reduce the stiffness of the tree branch, thus having a lower limit stress. Then, the challenge with this lies with how much strength a rotting section could have related to a tree without decay. It is clear that there are many options for continuing this particular work, while at the same time this methodology can be applied to many other types of related research.

APPENDICES

APPENDIX A

A. GENERAL AND FEM GEOMETRY OF TREE BRANCH

Measured Geometry of the Primary and Secondary Branches

BRANCH TYPE	Length (m)	Total Length (m)	Total Diameter (cm)	Element #
PRIMARY BRANCH	1	1	38	1
	1	2	35	2
	1	3	33.9	3
	1	4	33.9	4
	1	5	35.8	5
	1	6	29	6
	1	7	21	7
	1	8	19.9	8
	1	9	21.2	9
	1	10	20	10
	1	11	15.5	11
	0.5	11.5	15.4	12
SECONDARY BRANCH (REMAINDER BRANCH) @ 11.5m	1	1	15.4	13
	1	2	13.3	14
	1	3	11.2	15
	1	4	9.1	16
	1	5	7.0	17
	1	6	4.9	18
	1	7	2.7	19
	0.3	7.3	0.6	20
SECONDARY BRANCH 2 @ 7m	1	1	21.6	21
	1	2	19.6	22
	1	3	17.7	23
	1	4	15.7	24
	1	5	13.7	25
	1	6	11.8	26
	1	7	9.8	27
	1	8	7.9	28
	1	9	5.9	29
	1	10	3.9	30
	1	11	2.0	31
LATERAL BRANCH 3 @ 11.5m	1	1	12	32
	1	2	10.0	33
	1	3	8.0	34
	1	4	6.0	35
	1	5	4.0	36
	1	6	2.0	37

FEM Spatial Geometry of the Primary and Secondary Branches

Element #	Node i			Node j		
	X _i	Y _i	Z _i	X _i	Y _i	Z _i
1	0	0	0	0.7863	0.3177	0.5299
2	0.7863	0.3177	0.5299	1.5726	0.6354	1.0598
3	1.5726	0.6354	1.0598	2.2167	0.8956	1.7791
4	2.2167	0.8956	1.7791	3.1297	1.3021	1.814
5	3.1297	1.3021	1.814	3.7839	1.7602	2.4158
6	3.7839	1.7602	2.4158	4.4381	2.2183	3.0176
7	4.4381	2.2183	3.0176	5.0923	2.6764	3.6194
8	5.0923	2.6764	3.6194	5.7465	3.1345	4.2212
9	5.7465	3.1345	4.2212	6.4889	3.6543	4.6438
10	6.4889	3.6543	4.6438	6.923	4.5443	4.783
11	6.923	4.5443	4.783	7.0275	5.5388	4.783
12	7.0275	5.5388	4.783	7.0798	6.0361	4.783
13	7.0798	6.0361	4.783	6.9926	7.0323	4.783
14	6.9926	7.0323	4.783	6.9054	8.0285	4.783
15	6.9054	8.0285	4.783	6.8182	9.0247	4.783
16	6.8182	9.0247	4.783	6.731	10.0209	4.783
17	6.731	10.0209	4.783	6.6438	11.0171	4.783
18	6.6438	11.0171	4.783	6.5566	12.0133	4.783
19	6.5566	12.0133	4.783	6.4694	13.0095	4.783
20	6.4694	13.0095	4.783	6.4436	13.3083	4.783
21	5.0923	2.6764	3.6194	5.84653	2.0207	3.6543
22	5.84653	2.0207	3.6543	6.60076	1.365	3.6892
23	6.60076	1.365	3.6892	7.35499	0.7093	3.7241
24	7.35499	0.7093	3.7241	8.10922	0.0536	3.759
25	8.10922	0.0536	3.759	8.86345	-0.6021	3.7939
26	8.86345	-0.6021	3.7939	9.61768	-1.2578	3.8288
27	9.61768	-1.2578	3.8288	10.37191	-1.9135	3.8637
28	10.37191	-1.9135	3.8637	11.12614	-2.5692	3.8986
29	11.12614	-2.5692	3.8986	11.88037	-3.2249	3.9335
30	11.88037	-3.2249	3.9335	12.6346	-3.8806	3.9684
31	12.6346	-3.8806	3.9684	13.3891	-4.5359	4.0033
32	7.0798	6.0361	4.783	8.0646	6.2097	4.783
33	8.0646	6.2097	4.783	9.0494	6.3833	4.783
34	9.0494	6.3833	4.783	10.0342	6.5569	4.783
35	10.0342	6.5569	4.783	11.019	6.7305	4.783
36	11.019	6.7305	4.783	12.0038	6.9041	4.783
37	12.0038	6.9041	4.783	12.9886	7.078	4.783

APPENDIX B

B. MATLAB SCRIPT FOR IMPULSE LOAD SCENARIOS

```
function [time, force, disp] =
falling_load(m,l_rope,x_fall,strain_10_mbs,mbs,g,t_final,dt)

%Function calculates the displacement and spring force for a single degree
%of freedom oscillator with the mass freefalling onto the spring. This is
%meant to simulate a tree climber falling and being caught by a rope.
%Solution is based on the Chopra dynamics book
%SRA 10/10/16

% m = mass in kg
% l_rope = rope length in meters
% x_fall = fall distance in meters
% strain_10_mbs = percentage strain at 10% of rope breaking strength
% mbs = rope breaking strength in Newtons
% g = gravity accel in m/s
% t_final = final time at which to end calculation in seconds
% dt = time step for load calculation
%
k_rope = ((strain_10_mbs * l_rope) / (0.1*mbs) )^-1; %rope stiffness based on
10% proof load rating, assumes a single rope rigging system

k_branch = (77*g) / (3*2.54/100);%branch stiffness based on 77kg test and 3
inches of deflection, note, this is hard-coded and converted to meters

k_total = (1/k_rope + 1/k_branch)^-1;%add branch and rope stiffness in series

v_init = sqrt(2*g*x_fall); %compute initial velocity when rope becomes taught

w_n = sqrt(k_total/m); %natural frequency of climber-rope-branch system

x_init = -m*g/(k_total);%static displacement of branch-tree system

t = 0:dt:t_final; %setup a time vector that runs to the end of the simulation
time

x = x_init*cos(w_n*t) + v_init/w_n * sin(w_n*t); %compute the displacement of
the climber
f = k_total*x+m*g;%compute the force in the rope

cut_ind = min(find(x<x(1))); %trim the time vector so that it catches only the
first loading pulse, until the climber rebounds and the line becomes slack
t = t(1:cut_ind);

x = x_init*cos(w_n*t) + v_init/w_n * sin(w_n*t); %recompute displacement and
force using trimmed time vector
f = k_total*x+m*g;

%rename variables for nice output
time = t;
disp = x;
force = f;
```

```
%transpose the matrices  
time = time';  
disp = disp';  
force = force';  
end
```

APPENDIX C

C. MAXIMUM CALCULATED STRESSES FOR ALL SCENARIO TYPES

Impulse Load Scenarios – Greatest to Least

Scenario	Climber Mass (kg)	Rope Length (m)	Fall Distance (m)	Percent Strain at 10% of Rope MBS	Max. Load (N)	Max. Stress @ Element 7 (MPa)	% Within Limit Stress (37.5 MPa)
78	99.8	6.1	1.32	0.03	5065.4	32.3	86.3%
87	99.8	9.14	1.32	0.02	5066.2	32.3	86.3%
70	99.8	3.05	1.32	0.05	5195.8	32.3	86.2%
97	99.8	12.14	1.32	0.02	4840.7	32.3	86.1%
79	99.8	6.1	1.32	0.04	4840.1	32.3	86.1%
69	99.8	3.05	1.32	0.04	5340.7	32.3	86.1%
77	99.8	6.1	1.32	0.02	5340.7	32.3	86.1%
96	99.8	12.14	1.32	0.01	5341.2	32.3	86.1%
88	99.8	9.14	1.32	0.03	4742.5	32.2	86.0%
68	99.8	3.05	1.32	0.03	5502.4	32.2	85.9%
86	99.8	9.14	1.32	0.01	5503.0	32.2	85.9%
60	99.8	1.52	1.32	0.05	5592.3	32.2	85.8%
80	99.8	6.1	1.32	0.05	4650.9	32.2	85.8%
67	99.8	3.05	1.32	0.02	5684.9	32.1	85.7%
76	99.8	6.1	1.32	0.01	5684.9	32.1	85.7%
59	99.8	1.52	1.32	0.04	5686.2	32.1	85.7%
58	99.8	1.52	1.32	0.03	5786.4	32.1	85.5%
66	99.8	3.05	1.32	0.01	5893.1	32.0	85.4%
57	99.8	1.52	1.32	0.02	5893.8	32.0	85.4%
89	99.8	9.14	1.32	0.04	4490.2	32.0	85.3%
98	99.8	12.14	1.32	0.03	4489.9	32.0	85.3%
56	99.8	1.52	1.32	0.01	6009.3	31.9	85.2%
90	99.8	9.14	1.32	0.05	4286.6	31.6	84.3%
99	99.8	12.14	1.32	0.04	4226.6	31.5	84.0%
100	99.8	12.14	1.32	0.05	4020.6	30.9	82.5%
82	99.8	9.14	0.99	0.02	4552.5	29.5	78.7%
72	99.8	6.1	0.99	0.02	4787.7	29.5	78.7%
73	99.8	6.1	0.99	0.03	4551.8	29.5	78.7%
92	99.8	12.14	0.99	0.02	4359.0	29.5	78.7%
74	99.8	6.1	0.99	0.04	4358.4	29.5	78.7%
65	99.8	3.05	0.99	0.05	4663.2	29.5	78.6%
83	99.8	9.14	0.99	0.03	4274.7	29.5	78.6%
75	99.8	6.1	0.99	0.05	4196.5	29.4	78.4%

64	99.8	3.05	0.99	0.04	4787.7	29.4	78.4%
91	99.8	12.14	0.99	0.01	4788.1	29.4	78.4%
63	99.8	3.05	0.99	0.03	4926.9	29.3	78.2%
81	99.8	9.14	0.99	0.01	4927.4	29.3	78.2%
84	99.8	9.14	0.99	0.04	4058.9	29.3	78.1%
93	99.8	12.14	0.99	0.03	4058.7	29.3	78.1%
55	99.8	1.52	0.99	0.05	5004.3	29.3	78.0%
62	99.8	3.05	0.99	0.02	5084.0	29.2	77.9%
71	99.8	6.1	0.99	0.01	5084.0	29.2	77.9%
54	99.8	1.52	0.99	0.04	5085.1	29.2	77.9%
53	99.8	1.52	0.99	0.03	5171.5	29.1	77.7%
61	99.8	3.05	0.99	0.01	5263.4	29.1	77.5%
52	99.8	1.52	0.99	0.02	5264.0	29.1	77.5%
85	99.8	9.14	0.99	0.05	3884.8	29.0	77.3%
51	99.8	1.52	0.99	0.01	5363.4	29.0	77.3%
94	99.8	12.14	0.99	0.04	3834.0	28.9	77.1%
95	99.8	12.14	0.99	0.05	3658.0	28.4	75.8%
30	81.65	6.1	1.32	0.05	4100.7	26.7	71.2%
38	81.65	9.14	1.32	0.03	4184.0	26.7	71.2%
29	81.65	6.1	1.32	0.04	4272.7	26.7	71.2%
47	81.65	12.14	1.32	0.02	4273.3	26.7	71.2%
39	81.65	9.14	1.32	0.04	3954.3	26.7	71.1%
48	81.65	12.14	1.32	0.03	3954.0	26.7	71.1%
27	81.65	6.1	1.32	0.02	4727.3	26.6	71.0%
28	81.65	6.1	1.32	0.03	4477.5	26.6	71.0%
37	81.65	9.14	1.32	0.02	4478.3	26.6	71.0%
20	81.65	3.05	1.32	0.05	4596.6	26.6	70.9%
40	81.65	9.14	1.32	0.05	3768.6	26.5	70.7%
19	81.65	3.05	1.32	0.04	4727.3	26.5	70.7%
46	81.65	12.14	1.32	0.01	4727.8	26.5	70.7%
49	81.65	12.14	1.32	0.04	3714.3	26.5	70.6%
18	81.65	3.05	1.32	0.03	4874.8	26.4	70.4%
36	81.65	9.14	1.32	0.01	4875.3	26.4	70.4%
10	81.65	1.52	1.32	0.05	4956.8	26.4	70.3%
17	81.65	3.05	1.32	0.02	5040.9	26.3	70.0%
26	81.65	6.1	1.32	0.01	5040.9	26.3	70.0%
9	81.65	1.52	1.32	0.04	5042.1	26.3	70.0%
8	81.65	1.52	1.32	0.03	5132.9	26.2	70.0%
16	81.65	3.05	1.32	0.01	5229.2	26.2	69.9%
7	81.65	1.52	1.32	0.02	5229.9	26.2	69.9%
50	81.65	12.14	1.32	0.05	3525.9	26.2	69.8%
6	81.65	1.52	1.32	0.01	5334.6	26.0	69.4%

25	81.65	6.1	0.99	0.05	3686.6	24.4	65.1%
34	81.65	9.14	0.99	0.04	3561.0	24.4	65.0%
43	81.65	12.14	0.99	0.03	3560.8	24.4	65.0%
33	81.65	9.14	0.99	0.03	3757.9	24.4	65.0%
24	81.65	6.1	0.99	0.04	3834.3	24.4	64.9%
42	81.65	12.14	0.99	0.02	3834.9	24.4	64.9%
35	81.65	9.14	0.99	0.05	3402.1	24.3	64.8%
23	81.65	6.1	0.99	0.03	4010.5	24.2	64.7%
32	81.65	9.14	0.99	0.02	4011.2	24.2	64.7%
44	81.65	12.14	0.99	0.04	3355.6	24.2	64.6%
15	81.65	3.05	0.99	0.05	4112.0	24.2	64.4%
14	81.65	3.05	0.99	0.04	4225.4	24.1	64.2%
22	81.65	6.1	0.99	0.02	4225.4	24.1	64.2%
41	81.65	12.14	0.99	0.01	4225.8	24.1	64.2%
45	81.65	12.14	0.99	0.05	3194.7	24.0	64.0%
13	81.65	3.05	0.99	0.03	4351.2	24.0	64.0%
31	81.65	9.14	0.99	0.01	4351.6	24.0	64.0%
5	81.65	1.52	0.99	0.05	4421.4	23.9	63.7%
12	81.65	3.05	0.99	0.02	4494.4	23.8	63.6%
21	81.65	6.1	0.99	0.01	4494.4	23.8	63.6%
4	81.65	1.52	0.99	0.04	4495.3	23.8	63.6%
3	81.65	1.52	0.99	0.03	4574.1	23.8	63.4%
11	81.65	3.05	0.99	0.01	4657.8	23.7	63.3%
2	81.65	1.52	0.99	0.02	4658.3	23.7	63.3%
1	81.65	1.52	0.99	0.01	4748.7	23.6	62.8%

Climbing SRT Scenarios

Scenario	Max. Stress @ Element 7 (MPa)	% Within Limit Stress (37.5 MPa)
srt_climbing_j1	12.72	33.9%
srt_climbing_j2	12.74	34.0%
srt_climbing_m1	12.12	32.3%
srt_climbing_m2	11.80	31.5%

Climbing DdRT Scenarios

Scenario	Max. Stress @ Element 7 (MPa)	% Within Limit Stress (37.5 MPa)
ddrt_climbing_j1	9.6	25.5%
ddrt_climbing_j2	9.9	26.5%
ddrt_climbing_m1	8.4	22.5%
ddrt_climbing_m2	7.9	21.0%

BIBLIOGRAPHY

- Adams, M. (2007). Safe and efficient tree ascent: doubled rope techniques (DdRT). *Arborist News*, 16(3), 50–54. Retrieved from http://www.treebuzz.com/pdf/CC_Jun07.pdf
- Alvandi-Tabrizi, Y., Whisler, D. A., Kim, H., & Rabiei, A. (2015). High strain rate behavior of composite metal foams. *Materials Science and Engineering: A*, 631, 248–257. <http://doi.org/10.1016/j.msea.2015.02.027>
- Ashby, M. F., Evans, A. G., Fleck, N. A., Gibson, L. J., Hutchinson, J. W., & Wadley, H. N. G. (2000). *Metal Foams: A Design Guide* (Vol. 54). Butterworth-Heinemann.
- Banhart, J., & Seeliger, H. W. (1996). Aluminium Foam Sandwich Panels: Metallurgy, Manufacture and Applications. *Helmholtz-Berlin.De*, sdfdsf, 4–7. Retrieved from http://www.helmholtz-berlin.de/media/media/spezial/people/banhart/html/B-Conferences/b113_banhart2008.pdf
- Cardoso, E., & Oliveira, B. F. (2010). Study of the use of metallic foam in a vehicle for an energy-economy racing circuit. *Materialwissenschaft Und Werkstofftechnik*, 41(5), 257–264. <http://doi.org/10.1002/mawe.201000594>
- Friedl, O., Motz, C., Peterlik, H., Puchegger, S., Reger, N., & Pippan, R. (2008). Experimental investigation of mechanical properties of metallic hollow sphere structures. *Metallurgical and Materials Transactions B: Process Metallurgy and Materials Processing Science*, 39(1), 135–146. <http://doi.org/10.1007/s11663-007-9098-2>
- Gaitanaros, S., & Kyriakides, S. (2014a). Dynamic crushing of aluminum foams: Part I - Experiments. *International Journal of Solids and Structures*, 51(9), 1646–1661. <http://doi.org/10.1016/j.ijsolstr.2013.11.020>
- Gaitanaros, S., & Kyriakides, S. (2014b). Dynamic crushing of aluminum foams: Part II - Analysis. *International Journal of Solids and Structures*, 51(9), 1646–1661. <http://doi.org/10.1016/j.ijsolstr.2013.11.020>
- Gao, Z. Y., Yu, T. X., & Zhao, H. (2008). Mechanical Behavior of Metallic Hollow Sphere Materials: Experimental Study. *Journal of Aerospace Engineering*, 21(4), 206–216. [http://doi.org/10.1061/\(ASCE\)0893-1321\(2008\)21:4\(206\)](http://doi.org/10.1061/(ASCE)0893-1321(2008)21:4(206))
- Glass, S. V., & Zelinka, S. L. (2010). Moisture relations and physical properties of wood. In *Wood handbook: Wood as an engineering material* (p. 4.1-4.19). Madison, Wisconsin: General Technical Report (GTR-190). Forest Products Laboratory. [http://doi.org/General Technical Report FPL-GTR-190](http://doi.org/General%20Technical%20Report%20FPL-GTR-190)
- Kane, B. (2014). Determining parameters related to the likelihood of failure of red oak (*Quercus rubra* L.) from winching tests. *Trees - Structure and Function*, 28(6),

1667–1677. <http://doi.org/10.1007/s00468-014-1076-0>

Kane, B., & Clouston, P. (2008). Tree pulling tests of large shade trees in the genus *Acer*. *Arboriculture and Urban Forestry*, 34(2), 101–109.

Kennedy, A. (2012). Porous metals and metal foams made from powders. In K. Kondoh (Ed.), *Powder Metallurgy* (p. 124). InTech.

Kretschmann, D. E. (2010). Mechanical Properties of Wood. *Wood Handbook - Wood as an Engineering Material*, 5.1-5.46. Retrieved from http://www.fpl.fs.fed.us/documnts/fplgtr/fplgtr190/chapter_05.pdf?

Nakajima, H., Hyun, S. K., Tane, M., & Nakahata, T. (2006). Fabrication and Properties of Porous Materials with Directional Elongated Pores. *Materials Science Forum*, 512, 295–300. <http://doi.org/10.4028/www.scientific.net/MSF.512.295>

Newland, D. E., & Cebon, D. (2002). Could the World Trade Center have been modified to prevent its collapse? *ASCE Engineering Mechanics*, (November), 1360–1361.

Niklas, K. J. (1997). Mechanical properties of Black Locust (*Robinia pseudoacacia* L.) wood. Size- and age-dependent variations in sap- and heartwood. *Annals of Botany*, 79(3), 265–272. <http://doi.org/10.1006/anbo.1996.0340>

Park, C., & Nutt, S. . (2000). PM synthesis and properties of steel foams. *Materials Science and Engineering: A*, 288(1), 111–118. [http://doi.org/10.1016/S0921-5093\(00\)00761-9](http://doi.org/10.1016/S0921-5093(00)00761-9)

Paul, A., & Ramamurty, U. (2000). Strain rate sensitivity of a closed-cell aluminum foam. *Materials Science and Engineering: A*, 281(1–2), 1–7. [http://doi.org/10.1016/S0921-5093\(99\)00750-9](http://doi.org/10.1016/S0921-5093(99)00750-9)

Rabiei, A., & Vendra, L. J. (2009). A comparison of composite metal foam's properties and other comparable metal foams. *Materials Letters*, 63(5), 533–536. <http://doi.org/10.1016/j.matlet.2008.11.002>

Ramesh, K. T. (2008). High Strain Rate and Impact Experiments. *Handbook of Experimental Solid Mechanics*, 874.

Rock, A. (2016). *The High Strain Rate Response of Aluminum Open-Cell Foam*.

Rowe, N. P., & Speck, T. (1997). Biomechanical variation of non-selfsupporting plant growth habits: a comparison of herbaceous and large-bodied woody plants. In *L'Arbre, Biologie et Developpement* (C. Edelin, pp. 1–11).

Ryan, G., Pandit, A., & Apatsidis, D. P. (2006). Fabrication methods of porous metals for use in orthopaedic applications. *Biomaterials*, 27(13), 2651–2670. <http://doi.org/10.1016/j.biomaterials.2005.12.002>

- Sanders, W. S. (2002). Mechanical Behavior of Closed-Cell and Hollow-Sphere Metallic Foams.
- Shapovalov, V. (1998). No Title. In D. S. Schwartz et al. (Ed.), *Porous and Cellular Materials for Structural Applications* (521st ed., p. 281). Warrendale, PA: MRS.
- Smith, B. H. (2012). *Material Characterization and Computational Simulation of Steel Foam for Use in Structural Applications*. University of Massachusetts Amherst.
- Smith, B. H., Szyniszewski, S., Hajjar, J. F., Schafer, B. W., & Arwade, S. R. (2012). Steel foam for structures: A review of applications, manufacturing and material properties. *Journal of Constructional Steel Research*, 71, 1–10.
<http://doi.org/10.1016/j.jcsr.2011.10.028>
- Szyniszewski, S. T., Smith, B. H., Hajjar, J. F., Schafer, B. W., & Arwade, S. R. (2014). The mechanical properties and modeling of a sintered hollow sphere steel foam. *Materials and Design*, 54, 1083–1094. <http://doi.org/10.1016/j.matdes.2013.08.045>